The mathematical modeling of the single and ensemble dynamics of magnetic filaments

Rūdolfs Livanovičs

Department of Physics
University of Latvia

This dissertation is submitted for the degree of
Doctor of Physics

Scientific advisor:
Dr. habil. phys. Andrejs Cēbers

Riga 2015

ESF
EIROPAS SOCIĀLAIS FONDS

EIROPAS SAVIENĪBA

LATVIJAS UNIVERSITĀTE
ANNO 1919

IEGULDĪJUMS TAVĀ NĀKOTNĒ

This work has been supported by the European Social Fund within the project «Support for Doctoral Studies at University of Latvia».

Acknowledgements

I am most grateful to my scientific advisor Dr. habil. phys. Andrejs Cēbers for introducing me to the research of soft micromagnetic materials and guiding me over many years. Without his experienced guidance and helpful advice this work would not exist.

I would also like to thank my family for their support as well as my colleagues at the Faculty of Physics and Mathematics.

The financial support of the ESF and the University of Latvia is gratefully acknowledged.

Abstract

The use of biomimetic systems for the creation of microengines and fluid mixers is an active area of research in the field of soft matter. It is feasible to use magnetic filaments, which are easily controlled by varying the parameters of an external magnetic field, for the aforementioned purposes. In this work we have formulated a mathematical model of magnetic filaments that incorporates both the effects of twist and hydrodynamic interactions to varying degrees of approximation and implemented it in the form of two software libraries. We have used this model to explore the dynamics of both single filaments and ensembles of filaments within a wide range of control parameters and to derive new results concerning the behavior of both ferromagnetic and superparamagnetic filaments in time dependent magnetic fields.

Table of contents

List of figures

List of tables

Chapter 1

Introduction

Recent advances in material science and the continuing progress towards creating useful technological devices at the micrometer and nanometer scale have led to considerable scientific interest in potential sources of finely controlled motion that could be used as microengines, microfluidic mixers, etc. Microscopic magnetically actuated filaments provide one such candidate system and the purpose of this work is to establish a comprehensive mathematical model to numerically explore the behaviour of various types of magnetic filaments in a wide parameter space.

In this introductory chapter we begin by briefly describing the general background and biological inspiration for research in microscopic filaments in general as well as the motivation for this work in particular (sections 1.1 and 1.2). We also present a general outline of this thesis in section 1.3.

1.1 General background and motivation

One of the most prevalent trends in modern technologies is the ever decreasing characteristic size of the components used in the manufacturing of technological devices. This trend began more than fifty years ago with the invention of microscopic transistors, which ultimately led to the development of modern electronics and information technology. More recently, researchers have learned to produce not just microelectrical but micromechanical devices as well. The combination of the miniaturization of both electrical and mechanical components is referred to as micro electro mechanical systems (MEMS). Engineers have learned to mass produce many types of such devices using various techniques such as different kinds of microlithography, surface micromachining and others [57]. These developments have led to a great number of successful applications including microsensors, microscopic gyroscopes, displays, inkjet printers and many others.

All active microdevices require a supply of energy. These may be broadly divided in two groups: internal and external sources. The most prominent example of the former is the use of chemical energy, while external sources include the use of external electric and magnetic fields to supply the energy that actuates the motion of the device. The choice of using external sources of energy where feasible confers certain major advantages on microdevices - there is no need to transport or replenish a supply of expendible fuel and it is relatively easy to control the magnitude, geometry and time dependence of external magnetic or electric fields, potentially providing a means of precise control of the microdevice. We therefore focus on magnetically actuated microfilaments, composed of either ferromagnetic or superparamagnetic beads, which may be either artificially linked or self-assemble into linear chains under the influence of an external magnetic field. Nevertheless, the introduction of an external field does complicate the physics of the problem to a degree, so it is no surprise that, historically, the first scientific investigations in microscopic filamentary structures in Newtonian fluids considered devices actuated by internal energy rather than external fields.

Since the characteristic sizes of the systems we're considering are measured in microns, the Reynolds numbers associated with the fluid flows are almost negligibly small and we operate entirely within the viscosity dominated regime of Stokesian hydrodynamics. Insofar as controlled propulsion is desired, the Stokesian regime imposes a major constraint on the kind of dynamics we can use in the form of the scallop theorem (first published in 1977 by Purcell in his seminal paper *Life at Low Reynolds Number* [66]). The theorem states that in order to achieve net propulsion any prospective swimmer must undergo non-reciprocal deformations (that is to say, deformations that are not geometrically invariant with respect to time reversal). The name of the theorem derives from the observation that the scallop - the only mollusc in the class of bivalves able to swim on its own - only swims as a result of inertial effects and could not do so in the overdamped realm of Stokesian hydrodynamics. While scallops are fortunate enough to live at a scale where inertia can aid in propulsion, there are many examples in nature where that is not the case. For instance, nearly every cell in the human body utilizes a non-motile *primary cilium* [35] that until recently was thought to be a vestigial organelle of no importance. Much to the contrary, it was in fact shown to play a crucial role in cell function, regulation of cell growth and so many human diseases that genetic ciliopathies [2] are now a prolific object of medical research. In the case of flexible filaments, the necessary symmetry breaking is accomplished by hydrodynamic self-interactions - the process by which the filament, having experienced a force due to interaction with the external magnetic field, transfers momentum to the surrounding fluid, which in turn exerts a reaction force back on different segments of the filament. The mathematical description of hydrodynamic interactions is therefore a crucial part of modelling such devices and plays a commensurately central role in this dissertation.

1.2 Recent studies on microscopic magnetic filaments

While the rich structures formed in magnetorheological suspensions in the presence of external magnetic fields have long been recognized as an interesting field of study (see, for instance, Bossis [10] for a comprehensive review), specific interest in the fundamental dynamics and applications of chains of magnetic particles is of more recent origin. In 2003, Cēbers [12] demonstrated the existence of two basic metastable modes of deformation for elastic superparamagnetic filaments in a constant external magnetic field. While the existence of the S-like long lived states had been predicted before (by Cēbers [11] and Melle [58]), it was the newly found U-like hairpin shapes (also found experimentally by Goubault *et al* [39]) that would ultimately prove conducive to self-propulsion. This was shown by the seminal experiment of Dreyfus [24] in 2005, where a red blood cell was attached to a superparamagnetic filament, which was then able to transport the cell in a controlled direction using the energy provided by an external magnetic field. This experiment attracted a great deal of attention from researchers as the first practical demonstration of the considerable potential utility of magnetically actuated microswimmers for medical applications. The experiment of Dreyfus was soon numerically described by the model of Gauger and Stark [36]. While in the experiment the symmetry breaking necessary to satisfy the scallop theorem was provided by the attachment of the red blood cell, it was soon shown that it was also possible to induce propulsive behavior by material defects in the filament itself [67] or the buckling instability induced by the action of the external magnetic field. Several experimental and theoretical studies of superparamagnetic filaments followed, as reviewed by Cēbers in 2005 [13].

In an initially separate avenue of scientific research, it was also noted that magnetotactic bacteria contained chains of ferromagnetic particles [28]. Biologically inspired ferromagnetic filaments were also found [25] to exhibit similar behavior to superparamagnetic filaments in terms of their tendency to assume either U-like or S-like metastable shapes depending on the ratio of magnetic and elastic forces as well as the frequency of the external magnetic field. It was therefore shown [5] that a ferromagnetic microswimmer was just as feasible as a superparamagnetic one. Nevertheless, for the historical reasons outlined in this chapter, ferromagnetic swimmers remain somewhat less studied compared to their superparamagnetic counterparts, a deficiency which this dissertation partly attempts to address.

1.3 Main objectives of this dissertation

The primary aim of this work is to construct a comprehensive numerical model capable of handling a wide variety of ferromagnetic and superparamagnetic filament configurations in arbitrary external magnetic fields for both single filaments and filament ensembles, taking into account the effects of twist and hydrodynamic interactions. This is accomplished in Chapters 2 and 3 (as well as Appendices A and B).

The construction of this model enables us to formulate additional objectives relating to particular filament configurations that are of physical interest. In particular, we thoroughly explore the dynamics of ferromagnetic filaments with free ends in both two and three dimensions with a view towards applications in micropropulsion. We also consider artificial ferromagnetic cilia with potential applications in the mixing of microfluids, superparamagnetic microswimmers and ensembles of magnetic filaments, to examine the hydrodynamic coupling in different filament configurations.

Some of the research conducted during the preparation of this dissertation has already become a part of the scientific record. In particular, we have recently published results concerning the instability of the loops formed by ferromagnetic filaments in a constant magnetic field [26], a review of the dynamics of ferromagnetic microswimmers in the resistive force theory approximation [27], a discussion of the basic dynamics of ferromagnetic cilia without hydrodynamic interactions [14] and a study on creating self-propelling microdevices by attaching an elastic tail to a permanent magnetic dipole [55]. These results are not explicitly restated in this work except where necessary to provide context for the many additional results given here, particularly as it concerns the difference between the more accurate treatment of hydrodynamic interactions we present here and previous results.

1.4 Dissertation outline

A comprehensive description of the theoretical model of a magnetic filament is presented in Chapter 2. We begin by outlining a brief overview of the theoretical approaches used to describe different elastic filaments in Section 2.1 along with a short description of the methods used to model fluid flows in Stokesian fluids to varying degrees of accuracy. Section 2.2 describes the basic kinematic framework used to characterize the filament geometrically. In Section 2.3 we present the various energy densities that enable us to derive the force densities that affect the filament in the static case. We then proceed to discuss Stokesian hydrodynamics and derive both the basic equation of motion for the filament and several types of approximations for the mobility tensor that ultimately serves to characterize the hydrodynamic interactions the filament is subject to.

In Chapter 3 we introduce a discrete version of the expressions derived in Chapter 2 and describe the numerical model developed to solve the equations of motion for the filament, its generalization to an arbitrary number of filaments and the software implementation of the numerical model. We also explore the computational properties of the model, establish its accuracy and computational requirements for different values of the underlying numerical parameters.

Chapter 4 details a selection of the results obtained through the use of the numerical model, devoting particular attention to the impact of the hydrodynamic interactions at various levels of approximation. Finally, we present the main conclusions of this dissertation in Chapter 5.

Chapter 2

Theoretical model

2.1 General considerations

Before formulating the theoretical model of a flexible magnetic filament in a Stokesian fluid, we first review briefly the approaches used in the scientific literature. The first modern attempts to theoretically describe the full nonlinear dynamics of elastic filaments in viscous fluids (without the additional complexity of magnetism) are due to Wolgemuth, Powers and Goldstein [76], who formulated the basic bending and twist energy densities, derived the twist diffusion equation and analyzed the linearized dynamics analytically and established the existence of two possible states induced by the twist-bend coupling in a filament undergoing twist injection at one of its ends. This provides a useful test for any implementation of the filament equations of motion that includes the effects of twist, since it is possible to derive to appropriate critical values of the relevant parameters analytically and compare them to numerical results.

Cēbers [12] formulated a theoretical model of the full nonlinear dynamics of a two dimensional superparamagnetic filament (without hydrodynamic interactions at first) introducing the tangent angle formalism, where the equations of motion were formulated for the angle ϕ (where the tangent vector was given by $\mathbf{t} = (\cos\phi, \sin\phi)$) and solved in conjunction with an equation for the Lagrange multiplier used to ensure the inextensibility of the filament. While this approach proved quite useful for two dimensional calculations, it turned out that further generalizations to three dimensional filament configurations and the inclusion of the effects of twist produced a theoretical framework of considerable complexity [7] which required the use of a complex quantity called the complex curvature and was not particularly amenable to efficient numerical simulations. An alternative model in terms of the filament position vector along the filament's center line was therefore developed [26], generalized extensions of which form the basis of the approach used in this work.

It was recognized as early as 2006 [36] that improvements to the standard resistive force theory approximation for hydrodynamic interactions were highly desirable. Nevertheless, no applications of more sophisticated hydrodynamic models to the dynamics of ferromagnetic filaments currently exist in the published scientific literature and are therefore a major focus of this work. More generally, several promising approaches to the calculation of hydrodynamic interactions in Stokes flows do exist. Some examples include the Rotne-Prager-Yamakawa tensor [68] and the method of induced forces, which makes use of multipole expansions of the flow field [18][32], both of which are utilized in this work.

There also exist more general approaches which focus on the calculation of the entire flow field rather than just the mobility or friction tensors acting on collections of spheres or more general objects immersed in Stokes flow. The most widespread of these is the immersed boundary method [59], originally proposed by Peskin [64] to facilitate numerical modelling of the human heart, but later adapted for use in a wide variety of situations where fluid-structure interactions played a crucial role. While these methods are quite expensive computationally due to the necessity of solving the full Stokes (or Navier-Stokes in cases where Reynolds numbers were not negligibly small) equations, the appeal of immersed boundary and immersed interface [53] lay in their ability to utilize wildly different Eulerian (for the fluid flow) and Lagrangian (for the immersed body dynamics) numerical grids to maximize computational efficiency. Most recently, Tian *et al* [71] have published a novel reformulation of the immersed boundary method which utilized a lattice Boltzmann [16] method to ensure efficient and easily parallelizable solution of the hydrodynamics while retaining the advantages of the flexible coupling to the Lagrangian immersed body dynamics introduced by Peskin. This latter approach is under consideration for future extensions to this work to realize efficient modelling of filament ensembles in the case of large numbers of filaments, where current approaches face severe computational constraints (as described in Chapter 3.3).

2.2 Filament kinematics

It is assumed throughout this work that the filament is thin, with a radius considerably smaller than the total length of the filament. It is therefore reasonable to describe the filament as a one dimensional curve (taken to be the filament's center line) and make use of the standard framework of differential geometry [22].

Given filament coordinates as functions of a material coordinate ξ (which labels points on the center line of the filament) in the form $x(\xi), y(\xi)$ and $z(\xi)$ in $\mathbb{R}^3$ space, we may readily identify the arclength of the filament by noting that the distance between two points on the center line of the filament is given by $\left(\frac{\partial \mathbf{r}}{\partial \xi}\right)^2 d\xi^2 = d\mathbf{r}^2 = ds^2$. The unit tangent vector of the filament is then given by

$$\mathbf{t} = \frac{\frac{\partial \mathbf{r}}{\partial \xi}}{\left|\frac{\partial \mathbf{r}}{\partial \xi}\right|} = \frac{\partial \mathbf{r}}{\partial s}. \tag{2.1}$$

The position vector field in Cartesian coordinates may be now be expressed as as function of the arclength parameter s

$$\mathbf{r}(s) = x(s)\mathbf{i} + y(s)\mathbf{j} + z(s)\mathbf{k}, \tag{2.2}$$

where the vectors $\mathbf{i}, \mathbf{j}, \mathbf{k}$ give the standard Cartesian basis.

The normal and binormal vectors can now be defined as follows

$$\mathbf{n}(s) = \frac{d\mathbf{t}}{ds}, \tag{2.3}$$

$$\mathbf{b}(s) = \mathbf{t} \times \mathbf{n}. \tag{2.4}$$

The tangent, normal and binormal vectors together compose the Frenet frame. Thus, we now have a moving frame, defined at each point on the filament center line. This frame is purely intrinsic in that it describes the filament purely in terms of local quantities.

The filament curvature $\kappa(s)$ and torsion $\tau(s)$ are scalar functions defined in terms of the Frenet basis vectors by the Frenet equations

$$\frac{d\mathbf{t}(s)}{ds} = \kappa(s)\mathbf{n}(s), \frac{d\mathbf{n}(s)}{ds} = -\kappa(s)\mathbf{t}(s) + \tau(s)\mathbf{b}, \frac{d\mathbf{b}(s)}{ds} = -\tau(s)\mathbf{n}(s). \tag{2.5}$$

Geometrically, the curvature measures the bending of the filament in the $\mathbf{t} - \mathbf{n}$ plane, while the torsion quantifies any deviation from that plane. The Frenet frame is a moving frame, attached to the center line of the filament. Since the filament is not necessarily straight, the frame rotates as it traverses the center line.

The basic kinematic description outlined so far is, in fact, sufficient to proceed to deriving the dynamic equations describing a curved filament under the action of an external force (such as that induced in a magnetic material by an external magnetic field). However, in order to describe the effects of twist as well as for the sake of completeness, we should also introduce the material Darboux frame, which will prove quite useful in the subsequent chapters.

The Darboux frame consists of a set of three orthonormal director vectors $\mathbf{e}_1(s), \mathbf{e}_2(s), \mathbf{e}_3(s)$. As a matter of convention, we will assign $\mathbf{e}_1(s)$ and $\mathbf{e}_2(s)$ to the principal directions of the cross section of the filament at any s. The third vector is then given by $\mathbf{e}_3(s) = \mathbf{e}_1(s) \times \mathbf{e}_2(s)$. Since the cross section is always orthogonal to the center line of the filament it follows that $\mathbf{e}_3(s) = \mathbf{t}(s)$. Throughout this work $\mathbf{e}_3(s)$ and $\mathbf{t}(s)$ will be used interchangably, generally preferring $\mathbf{t}(s)$ wherever explicit reference to the Darboux (as opposed to the Frenet) frame is not strictly necessary for clarity.

The angular velocity vector of the material frame $(\mathbf{e}_1(s), \mathbf{e}_2(s), \mathbf{e}_3(s))$ is called the Darboux vector $\mathbf{\Omega}$ [62]. Its properties may be obtained by considering the (rotational) changes the material basis vectors undergo as the natural parameter s is varied, leading to

$$\frac{\partial \mathbf{e}_i}{\partial \mathbf{s}} = \mathbf{\Omega} \times \mathbf{e}_i \tag{2.6}$$

for each $i = 1, 2, 3$. To express the Darboux vector directly we may simply take the cross product of both sides of (2.6) and an arbitrary Darboux basis vector to obtain

$$\mathbf{\Omega} = \mathbf{e}_i \times \frac{\partial \mathbf{e}_i}{\partial s} + \mathbf{e}_i \left(\mathbf{e}_i \cdot \mathbf{\Omega}\right). \tag{2.7}$$

The components of the Darboux vector are given by cyclic permutation of the indices according to the properties of the vector cross product

$$\Omega_1 = \frac{\partial \mathbf{e}_2}{\partial s} \cdot \mathbf{e}_3, \tag{2.8}$$

$$\Omega_2 = \frac{\partial \mathbf{e}_3}{\partial s} \cdot \mathbf{e}_1 \tag{2.9}$$

and

$$\Omega_3 = \frac{\partial \mathbf{e}_1}{\partial s} \cdot \mathbf{e}_2. \tag{2.10}$$

We can now identify the curvature and torsion with the components of the Darboux vector from the Frenet equations and the component expressions (2.8) - (2.10) if we recall that the tangent vector of the Frenet frame will always coincide with the material basis vector $\mathbf{e}_3$:

$$\Omega_1^2 + \Omega_2^2 = \kappa^2, \Omega_3 = \tau + \frac{\partial \psi}{\partial s}, \tag{2.11}$$

where ψ denotes the angle between the Frenet normal vector $\mathbf{n}$ and the material frame vector $\mathbf{e}_2$ so that $\cos(\psi) = \mathbf{e}_2 \cdot \mathbf{n}$. This is the crucial difference between the Frenet and the Darboux frame.

The kinematic framework established here will be used in the next section to construct the necessary expressions for the forces acting on the filament and to eventually arrive at the equations of motion for the filament.

2.3 Filament dynamics

To derive the expressions for the forces and moments acting on an arbitrary element of the filament cross section it is useful to first define the total energy associated with the physical processes the filament is subjected to. The total energy is the sum of the energies associated with the phenomena of (a) bending, (b) twist, (c) the internal tension associated with enforcing the inextensibility of the filament as well as (d) the magnetic forces induced by the interaction between the external magnetic field and the magnetic materials in the structure of the filament:

$$E = E_{bending} + E_{twist} + E_{stretching} + E_{magnetic}. \tag{2.12}$$

The bending energy [52] is given by

$$E_{bending} = \frac{1}{2}A\int_0^L \left(\frac{\partial^2 \mathbf{r}}{\partial s^2}\right)^2 ds = \frac{1}{2}A\int_0^L \kappa^2 ds = \frac{1}{2}A\int_0^L \left(\Omega_1^2 + \Omega_2^2\right) ds, \tag{2.13}$$

where A denotes the bending stiffness, assumed constant throughout the filament ($A = \frac{\pi}{4}a^4Y$ for a circular filament with radius a and Young modulus Y [49]), L is the length of the filament and ds denotes the differential line element of the filament in its natural parametrization. The kinematic quantities $\mathbf{r}$, κ and the components of the vector $\mathbf{\Omega}$ have already been identified in the previous section.

The twist energy [52] is

$$E_{twist} = \frac{1}{2}C\int_0^L \Omega_3^2 ds, \tag{2.14}$$

where C is the torsional stiffness, assumed constant throughout the filament.

The condition of inextensibility may be expressed as

$$\frac{\partial \mathbf{r}}{\partial s} \cdot \frac{\partial \mathbf{r}}{\partial s} = 1, \tag{2.15}$$

which may be enforced using a Lagrange multiplier function. Therefore, the associated energy may be formally defined as

$$E_{tension} = \frac{1}{2}\int_0^L \Lambda(s)\left(\frac{\partial \mathbf{r}}{\partial s}\right)^2 ds, \tag{2.16}$$

where $\Lambda(s)$ is a local Lagrange multiplier function. Physically, this may be interpreted without loss of generality as an internal tensile force within the filament, as will become more apparent after the appropriate force densities have been derived.

The magnetic energy for a ferromagnetic filament [51] is

$$E_{magnetic} = MH \int_0^L (\mathbf{h} \cdot \mathbf{t}) ds = MH \int_0^L \left(\mathbf{h} \cdot \frac{\partial \mathbf{r}}{\partial s} \right) ds, \tag{2.17}$$

where M is the magnitude of the spontaneous magnetization per unit length of the filament (the magnetization vector per unit length is given by $-M\mathbf{t}$), H is the strength of the external magnetic field and the unit vector $\mathbf{h}$ is the direction vector of the aforementioned field.

The magnetic energy for a superparamagnetic filament (see Appendix A for a derivation) is given by

$$E_{magnetic} = M_0 \int_0^L (\mathbf{h} \cdot \mathbf{t})^2 ds = M_0 \int_0^L \left(\mathbf{h} \cdot \frac{\partial \mathbf{r}}{\partial s} \right)^2 ds, \tag{2.18}$$

where $M_0 = \frac{a^2(\mu-1)^2 H^2}{8(\mu+1)}$ and μ denotes the magnetic permeability of the filament with a as its radius.

In order to describe the dynamics of a magnetic filament, we must first determine the forces that control its motion. Let us consider an arbitrary infinitesimal internal segment of the filament located between two arbitrarily close cross sections (at a distance ds) within the filament. We then have a force $-\mathbf{F}$ on one end of the segment and $\mathbf{F} + d\mathbf{F}$ on the other. A mechanical equilibrium (a state in which linear and angular momenta are conserved and the net force and moment both equal zero) may then be imposed by applying an external force $\mathbf{K}ds$, which must balance the total internal force $d\mathbf{F}$. Therefore, since all the forces must sum to zero at equilibrium, it follows that

$$\mathbf{K} = -\frac{d\mathbf{F}}{ds}. \tag{2.19}$$

Moments acting on the segment may be treated in an identical fashion. To first order (the moment produced by the external force $\mathbf{K}$ is of higher order) this yields

$$\frac{d\mathbf{M}}{ds} = \mathbf{F} \times \mathbf{t}, \tag{2.20}$$

where $\mathbf{M}$ denotes the external moment required to achieve mechanical equilibrium.

According to the principle of virtual work, if an infinitesimal displacement of the filament is considered, the sum of the total energy (2.12) and the external forces $\mathbf{K}$ acting on the filament must be at a minimum in equilibrium. This means that any variation in the functional of the internal energy of the filament must be balanced by an appropriate change in the external forces if equilibrium is to be maintained. Using the calculus of variations [37], generalizing the infinitesimal segment invoked previously to the entire filament and taking into account the ends of the filament, we can express the first variation of the filament energy functional (2.12) in the following general form, one that is very similar to the traditional approach employed in the tangent angle formalism [12]:

$$\delta E = -\int_0^L (\mathbf{f}\cdot\delta\mathbf{r} + m\delta\chi_3)\,ds + \left(\mathbf{F}_{ext}\cdot\delta\mathbf{r} + \mathbf{M}_{ext}\cdot\boldsymbol{\varepsilon}\right)\Big|_0^L, \tag{2.21}$$

where $\mathbf{f}$ denotes the total internal force density

$$\mathbf{f} = \mathbf{f}_{bending} + \mathbf{f}_{twist} + \mathbf{f}_{tension} + \mathbf{f}_{magnetic}, \tag{2.22}$$

while m is the internal moment density required to hold the filament in an equilibrium configuration against twist, $\mathbf{F}_{ext}$ and $\mathbf{M}_{ext}$ denote the external forces and moments acting on the appropriate ends of the filament, $\delta\mathbf{r}$ is the variation of the position vector of the filament, whereas the angle variation $\delta\chi_3$ describes the rotational variation of the basis vector $\mathbf{e}_3$ in the Darboux frame. Evidently, to obtain the force densities we require to formulate an equation of motion for the filament we will first have to calculate a number of auxiliary quantities, including the variation of the position vector. Before we proceed, it should be noted that there are several approaches to calculating the energy variation in the published literature. One of the most concise and geometrically illustrative approaches for the particular case of inextensible filaments was recently given by Powers [65] and it will be employed throughout this chapter.

In order to compute the necessary variations it is useful to first consider the variation of the arclength of the filament (to first order):

$$\delta ds = \sqrt{\left(\frac{\partial\mathbf{r}}{\partial s} + \frac{\partial}{\partial s}(\delta\mathbf{r})\right)^2} - ds = \frac{\partial\mathbf{r}}{\partial s}\cdot\frac{\partial}{\partial s}(\delta\mathbf{r}). \tag{2.23}$$

Given the constraint of inextensibility we only consider variations that do not stretch the filament so that $\delta ds = 0$ and therefore

$$\frac{\partial\mathbf{r}}{\partial s}\cdot\frac{\partial}{\partial s}(\delta\mathbf{r}) = 0. \tag{2.24}$$

Thus, the order in which we calculate the derivative of the variation of the position vector and the variation of the derivative of the position vector becomes irrelevant and the notation can be simplified accordingly

$$\frac{\partial}{\partial s}(\delta \mathbf{r}) = \delta \frac{\partial \mathbf{r}}{\partial s} = \delta \mathbf{r}'. \tag{2.25}$$

Let us now consider infinitesimal variations of the body-fitted Darboux frame. Since we only consider those variations that are constrained to preserve the inextensible nature of the filament, it follows that variations may only change the Darboux basis vectors by an infinitesimal rotation angle χ_i so that

$$\delta \mathbf{e}_i = \boldsymbol{\varepsilon} \times \mathbf{e}_i, \tag{2.26}$$

where $\boldsymbol{\varepsilon} = \delta\chi_1 \mathbf{e}_1 + \delta\chi_2 \mathbf{e}_2 + \delta\chi_3 \mathbf{e}_3$.

Having obtained the variations of the basis vectors we are now equipped to derive the variation of the angular velocity (or Darboux) vector $\boldsymbol{\Omega}$ of the material frame we defined as part of the description of the kinematic framework in Section 2.1. Recall that $\boldsymbol{\Omega}$ is defined by

$$\frac{\partial \mathbf{e}_i}{\partial s} = \boldsymbol{\Omega} \times \mathbf{e}_i, \quad i = 1, 2, 3. \tag{2.27}$$

Its variation will prove useful in deriving the twist force density. We may begin by taking the variation of both sides of equation (2.27)

$$\delta \frac{\partial \mathbf{e}_i}{\partial s} = \delta(\boldsymbol{\Omega} \times \mathbf{e}_i). \tag{2.28}$$

Note that $\delta \frac{\partial \mathbf{e}_i}{\partial s} = \frac{\partial}{\partial s}(\boldsymbol{\varepsilon} \times \mathbf{e}_i)$ due to equations (2.26) and (2.25). Utilizing the standard rules of differentiation and the definition of the Darboux vector we get

$$\delta\boldsymbol{\Omega} \times \mathbf{e}_i = \frac{\partial \boldsymbol{\varepsilon}}{\partial s} \times \mathbf{e}_i + \boldsymbol{\varepsilon} \times (\boldsymbol{\Omega} \times \mathbf{e}_i) - \boldsymbol{\Omega} \times (\boldsymbol{\varepsilon} \times \mathbf{e}_i), \tag{2.29}$$

which is easily simplified using the rules of vector calculus and the fact that for an arbitrary vector $\mathbf{v}$, if $\mathbf{v} \times \mathbf{e}_i = \mathbf{0}$ for all values of the index i, it follows that $\mathbf{v} = \mathbf{0}$. The final form of the variation of the Darboux vector is thus given by

$$\delta\boldsymbol{\Omega} = \frac{\partial \boldsymbol{\varepsilon}}{\partial s} + \boldsymbol{\varepsilon} \times \boldsymbol{\Omega}. \tag{2.30}$$

We have now derived the necessary variations for the geometric quantities describing the filament in the Darboux frame. Before proceeding with the calculation of the force densities, however, let us consider the geometric significance of the results we have just obtained.

The variation of the Darboux vector given in (2.30) is by itself sufficient to establish the existence of a coupling between curvature and twist. In particular, if we impose a non-zero deformation of the filament's center line in the form $\boldsymbol{\varepsilon} = \delta\chi_1\mathbf{e}_1 + \delta\chi_2\mathbf{e}_2$ and write out the components of equation (2.30) explicitly:

$$\delta\Omega_1 = \delta\frac{d\chi_1}{ds} + \Omega_2\delta\chi_3 - \Omega_3\delta\chi_2, \tag{2.31}$$

$$\delta\Omega_2 = \delta\frac{d\chi_2}{ds} + \Omega_3\delta\chi_1 - \Omega_1\delta\chi_3, \tag{2.32}$$

$$\delta\Omega_3 = \delta\frac{d\chi_3}{ds} + \Omega_1\delta\chi_2 - \Omega_2\delta\chi_1, \tag{2.33}$$

we see from equation (2.33) that, given non-zero curvature $\kappa = \sqrt{\Omega_1^2 + \Omega_2^2} \neq 0$ any deformation of the center line will result in a change in twist. This implies that even given zero initial twist and no external moments acting on the ends of the filament, a filament may still twist as a result of other deformations and this should always be considered when exploring the properties a new filament configuration - it is not always trivial to decide whether the effects of twist may be neglected and often a numerical investigation is required. It is, however, true, as we will see in later chapters, that this effect is often quite negligible in many situations of practical interest.

Furthermore, the converse is not strictly true. If we impose an explicit change of twist in the form $\boldsymbol{\varepsilon} = \delta\chi_3\mathbf{e}_3$, the principal curvatures Ω_1 and Ω_2 do change (see equations (2.31) and (2.32)), but the curvature $\kappa = \sqrt{\Omega_1^2 + \Omega_2^2}$ remains invariant.

We can now return to the filament energy variation given in equation (2.21) and consider the individual terms. The force density term can be immediately rewritten as follows using the product rule for the derivative

$$\mathbf{f} \cdot \delta\mathbf{r} = \frac{\partial \mathbf{F}}{\partial s} \cdot \delta\mathbf{r} = \frac{\partial}{\partial s}(\mathbf{F} \cdot \delta\mathbf{r}) - \mathbf{F} \cdot \delta\mathbf{e}_3. \tag{2.34}$$

Using the definition of the constrained variation given in eq. (2.26) we can rewrite the last term to obtain

$$\mathbf{f} \cdot \delta\mathbf{r} = \frac{\partial}{\partial s}(\mathbf{F} \cdot \delta\mathbf{r}) - \mathbf{F} \cdot \boldsymbol{\varepsilon} \times \mathbf{e}_3 = \frac{\partial}{\partial s}(\mathbf{F} \cdot \delta\mathbf{r}) - \boldsymbol{\varepsilon} \cdot \mathbf{e}_3 \times \mathbf{F}, \tag{2.35}$$

where the last expression was obtained using the properties of the scalar triple product.

A similar approach can be adopted to deal with the moments. We begin by noting that the variations of the components of the Darboux vector given in equations (2.31)-(2.33) let us once again utilize the properties of the scalar triple product and write for the moment components

$$M_i \delta \Omega_i = M_i \delta \frac{\partial \chi_i}{\partial s} + \mathbf{M} \cdot \boldsymbol{\Omega} \times \boldsymbol{\varepsilon}. \tag{2.36}$$

Making use of the derivative product rule again we obtain

$$M_i \delta \Omega_i = \frac{\partial}{\partial s} \left(M_i \delta \chi_i \right) - \frac{\partial \mathbf{M}}{\partial s} \cdot \boldsymbol{\varepsilon}. \tag{2.37}$$

Furthermore, from equations (2.30) - (2.33) it follows that

$$\mathbf{M} \cdot \frac{\partial \boldsymbol{\varepsilon}}{\partial s} = M_1 \delta \Omega_1 + M_2 \delta \Omega_2 + M_3 \delta \Omega_3. \tag{2.38}$$

From the energy densities specified in equations (2.13) and (2.14) we also know the moments for bending and twist: $M_1 = A\Omega_1$, $M_2 = A\Omega_2$ and $M_3 = C\Omega_3$. Using equation (2.38) we may now express the energy variation in the following way

$$\delta E = -\int_0^L \boldsymbol{\varepsilon} \cdot \frac{\partial \mathbf{M}}{\partial s} ds - \int_0^L \boldsymbol{\varepsilon} \cdot \mathbf{M}_m ds + \left(\mathbf{F}_{ext} \cdot \delta \mathbf{r} + \mathbf{M}_{ext} \cdot \boldsymbol{\varepsilon} \right) \big|_0^L , \tag{2.39}$$

where $\mathbf{M}_m$ is the moment associated with the interaction with the external magnetic field, written in a generalized way to avoid writing two separate expressions to accommodate both ferromagnetic and superparamagnetic filaments. Since equation (2.39) must hold for an arbitrary infinitesimal basis vector rotation $\boldsymbol{\varepsilon}$ and considering equations (2.21), (2.35) and (2.37) the following moment balance equation must be true:

$$\frac{\partial \mathbf{M}}{\partial s} + \mathbf{e}_3 \times \mathbf{F} + \mathbf{M}_m + \mathbf{M}_v = \mathbf{0}, \tag{2.40}$$

where $\mathbf{M}_v$ is technically arbitrary at this point, but may be readily identified with the viscous torque per unit length from physical considerations. One may note that in the absence of the magnetic and viscous torques, equation (2.40) reduces to the classical equilibrium moment balance equation for a bent and twisted rod [52].

Excluding the tangential part of equation (2.40) and disregarding the magnetic and viscous terms we immediately obtain

$$\mathbf{F} = -A \left(\frac{\partial^3 \mathbf{r}}{\partial s^3} - \frac{\partial \mathbf{r}}{\partial s} \left(\frac{\partial \mathbf{r}}{\partial s} \cdot \frac{\partial^3 \mathbf{r}}{\partial s^3} \right) \right) + C\Omega_3 \frac{\partial \mathbf{r}}{\partial s} \times \frac{\partial^2 \mathbf{r}}{\partial s^2}. \tag{2.41}$$

The first term in equation (2.41) is the bending force minus its tangential part. The tangential part can then be absorbed into the tension force density which we shall obtain shortly, since it by definition includes all of the internal tension in the filament that ultimately serves to ensure that the inextensibility constraint is satisfied. The second term is the twisting force, which can be simply differentiated with respect to the arclength parameter of the filament to obtain the twist force density

$$\mathbf{f}_{twist} = C\frac{\partial}{\partial s}\left(\Omega_3(s)\frac{\partial \mathbf{r}}{\partial s}\times\frac{\partial^2 \mathbf{r}}{\partial s^2}\right). \tag{2.42}$$

The bending force density is simply the derivative of the first term in eq. (2.41):

$$\mathbf{f}_{bending} = A\frac{\partial^4 \mathbf{r}}{\partial s^4}. \tag{2.43}$$

We have now obtained the moment balance equation for the filament and used it to determine the bending and twist force densities. However, we still need to find the tension and magnetic force densities as well as the boundary conditions. While the moment balance approach could be further extended to accomplish this, it is much more straightforward to obtain these directly from the energy densities specified in the beginning of this chapter.

To illustrate the simplicity of this approach, let us force derive the bending force density directly from the energy density given in equation (2.13). The variation for the bending energy of the filament may be formally expressed as

$$\delta E_{bending} = A\int_0^L \mathbf{r}''\cdot\delta\mathbf{r}''ds, \tag{2.44}$$

where the primes denote differentiation with respect to the natural parameter. Integrating equation (2.44) by parts yields

$$\delta E_{bending} = -A\int_0^L \mathbf{r}'''\delta\mathbf{r}'ds + \left(\mathbf{r}''\delta\mathbf{r}'\right)\big|_0^L, \tag{2.45}$$

which may be integrated by parts again to give

$$\delta E_{bending} = A\int_0^L \mathbf{r}''''\delta\mathbf{r}ds + \left(\mathbf{r}''\delta\mathbf{r}' - \mathbf{r}'''\delta\mathbf{r}\right)\big|_0^L. \tag{2.46}$$

The bending force per unit length can now be calculated directly as the functional derivative of the energy term

$$\mathbf{f}_{bending} = \frac{\partial \mathbf{F}_{bending}}{\partial s} = -\frac{\delta E_{bending}}{\delta \mathbf{r}} = -A\frac{\partial^4 \mathbf{r}}{\partial s^4}, \tag{2.47}$$

where $\mathbf{F}_{bending}$ denotes the bending force (rather than the force density) and the boundary terms of equation (2.46) will be used later on to establish the boundary conditions for the filament.

The derivation of the tension and the magnetic force densities is analogous to the bending force and may be found in Appendix B. The resulting tension force density required to ensure the inextensibility of the filament is

$$\mathbf{f}_{tension} = \frac{\partial}{\partial s}\left(\Lambda \frac{\partial \mathbf{r}}{\partial s}\right). \tag{2.48}$$

The magnetic force density for the ferromagnetic filament is given by

$$\mathbf{f}_{magnetic} = \mathbf{0}, \tag{2.49}$$

while the superparamagnetic case yields

$$\mathbf{f}_{magnetic} = -2M_0 \left(\mathbf{h} \cdot \frac{\partial^2 \mathbf{r}}{\partial s^2}\right) \mathbf{h}. \tag{2.50}$$

Note that equation (2.49) does not imply that a ferromagnetic filament is unaffected by the external magnetic field, since we have not yet considered boundary conditions. It is, however, interesting to note that within the limits of the approximations we have employed the magnetic force density affecting a ferromagnetic filament acts only on the ends of the filament.

The use of this direct approach does, however, have its limitations. We might, for instance, try to derive the twist force density we obtained from the moment balance approach using the relevant energy density directly. To do so, let us formally write the variation of the twist energy as follows

$$\delta E_{twist} = C \int_0^L \Omega_3 \delta \Omega_3 ds = C \int_0^L \Omega_3 \left(\delta \frac{d\chi_3}{ds} + \Omega_1 \delta \chi_2 - \Omega_2 \delta \chi_1\right) ds. \tag{2.51}$$

Noting that, due to the condition of inextensibility (2.15), $\delta\chi_1 = -\mathbf{e}_2 \cdot \delta \partial_s \mathbf{r}$ and $\delta\chi_2 = \mathbf{e}_1 \cdot \delta \partial_s \mathbf{r}$ (which are the only two possible degrees of freedom for the variation δr, as we are only considering an infinitesimal rotation), one may rewrite the integral (2.51) as follows

$$\delta E_{twist} = C \int_0^L \left(\Omega_3 \frac{\partial \mathbf{e}_1}{\partial s} \cdot \delta \frac{\partial \mathbf{r}}{\partial s} + \Omega_3 \mathbf{e}_1 \cdot \delta \frac{\partial^2 \mathbf{r}}{\partial s} - \Omega_3 \Omega_1 \mathbf{e}_2 \delta \frac{\partial \mathbf{r}}{\partial s} - \Omega_3 \Omega_2 \delta \mathbf{e}_2 \cdot \mathbf{e}_3\right). \tag{2.52}$$

One could now proceed to laboriously calculate each of the four terms in (2.52) and obtain the necessary force density, but it is quite evident that the moment balance approach employed previously was much better suited for the particular task of finding the twist force density. Nevertheless, the direct approach is clearly very convenient for quickly obtaining expressions for the other force densities and easily yields boundary terms that will be useful later.

Although we have now derived all of the force densities acting on a bent and twisted magnetic filament in an external magnetic field, there are still two crucial free parameters that remain to be determined - the internal tension $\Lambda(s)$ and the twist $\Omega_3(s)$. For the former, the traditional approach used in works that utilize the tangent angle formalism (see [12] for the classical treatment) is to use a variational approach to derive an equation for $\Lambda(s)$ to be solved in conjunction with the equations of motion of the filament. We will now illustrate why this approach is not particularly useful in the formalism employed here.

We may start by noting that the condition of inextensibility given in equation (2.15) may be rewritten as

$$\mathbf{t}(s) \cdot \frac{\partial \mathbf{v}(s)}{\partial s} = 0, \tag{2.53}$$

which may then be reformulated in an integral form to incorporate the tension term from equation (2.48)

$$0 = -\int_0^L \Lambda \mathbf{t} \cdot \frac{\partial \mathbf{v}}{\partial s} ds = \int_0^L \mathbf{v} \cdot \frac{\partial (\Lambda \mathbf{t})}{\partial s} ds - (\mathbf{v} \cdot \Lambda \mathbf{t})|_L + (\mathbf{v} \cdot \Lambda \mathbf{t})|_0 . \tag{2.54}$$

Since, up to first approximation and disregarding hydrodynamic interactions (see Section 2.4 for the full treatment), the velocity can be expressed as $\mathbf{v} = \zeta^{-1} \sum \mathbf{f}$, we can substitute in the bending force density from (2.47) and write

$$T = \int_0^L \left(-A \frac{\partial^4 \mathbf{r}}{\partial s^4} \cdot \frac{\partial (\Lambda \mathbf{t})}{\partial s} + \mathbf{f}_{magnetic} \cdot \frac{\partial (\Lambda \mathbf{t})}{\partial s} + \left(\frac{\partial (\Lambda \mathbf{t})}{\partial s} \right)^2 \right) ds, \tag{2.55}$$

where we have left the magnetic term unspecified for generality (the magnetic properties of the filament are irrelevant to this derivation) and the twist term has been omitted for brevity. The standard way to derive an equation for the function $\Lambda(s)$ is to find the associated Euler-Lagrange equation [20]. In order to do so, we need to compute the functional derivatives $\partial T / \partial \Lambda$ and $\partial T / \partial \Lambda'$, where T refers to the functional (2.55). This is fairly straightforward to do, yielding

$$\frac{\partial T}{\partial \Lambda} = \mathbf{r}^{(4)} \mathbf{t}' - 2\Lambda' \mathbf{t} \mathbf{t}' - 2\Lambda \mathbf{t}' \mathbf{t}' + \mathbf{f}_{magnetic} \mathbf{t}', \tag{2.56}$$

$$\frac{\partial T}{\partial \Lambda'} = \mathbf{r}^{(4)} \mathbf{t} - 2\Lambda \mathbf{t} \mathbf{t}' - 2\Lambda' \mathbf{t} \mathbf{t} + \mathbf{f}_{magnetic} \mathbf{t}, \tag{2.57}$$

where the primes as well as the superscript (4) denote the appropriate order derivatives with respect to the arclength s. The derivative $\frac{\partial}{\partial s}\frac{\partial T}{\partial \Lambda'}$ reads

$$\mathbf{r}^{(5)}\mathbf{t}+\mathbf{r}^{(4)}\mathbf{t}'-2\left(\Lambda'\mathbf{t}\mathbf{t}'+\Lambda\mathbf{t}'\mathbf{t}'+\Lambda\mathbf{t}'\mathbf{t}''\right)-2\left(\Lambda''\mathbf{t}\mathbf{t}+2\Lambda'\mathbf{t}\mathbf{t}'\right)+\left(\mathbf{f}_{magnetic}\mathbf{t}\right)'. \tag{2.58}$$

Putting (2.56), (2.57) and (2.58) together and algebraically simplifying the results we obtain the Euler-Lagrange equation for the tension Λ

$$-\frac{\partial^5\mathbf{r}}{\partial s}+2\frac{\partial^2\Lambda}{\partial s^2}\mathbf{t}+4\frac{\partial\Lambda}{\partial s}\frac{\partial\mathbf{t}}{\partial s}+2\Lambda\mathbf{t}\frac{\partial\mathbf{t}}{\partial s}\frac{\partial^2\mathbf{t}}{\partial s^2}-\frac{\partial\mathbf{f}_{magnetic}}{\partial s}=\mathbf{0}. \tag{2.59}$$

It is evident that in contrast to the tangent angle formalism [12], where the tension equation was considerably simpler than the equation of motion, the differential equation we have obtained here is a fairly complicated way to go about ensuring the inextensibility of the filament. Fortunately, there is a better way, incorporated as part of the numerical model and described along with it in Chapter 3 of this work.

To conclude this description of filament dynamics, it only remains to develop an equation for the twist density $\Omega_3(s)$. In order to do so, let us return to considering a constrained variation that only rotates an arbitrary segment of the filament, but does not stretch it, as defined in (2.26). The local angular velocity vector with respect to an infinitesimal time δt may be written as $\boldsymbol{\omega}=\frac{\boldsymbol{\varepsilon}}{\delta t}$. The constrained variation of the basis vectors (2.26) can now be expressed using the local angular velocity as

$$\frac{\delta\mathbf{e}_i}{\delta t}=\boldsymbol{\omega}\times\mathbf{e}_i. \tag{2.60}$$

In the limit where δt tends to zero, (2.60) reduces to

$$\frac{\partial\mathbf{e}_i}{\partial t}=\boldsymbol{\omega}\times\mathbf{e}_i. \tag{2.61}$$

The same argument holds for the time derivative of the Darboux vector in the limit $\delta t\to 0$. Taking into account the constrained variation of the Darboux vector (2.30) we may express the temporal change of the Darboux vector in terms of the local angular velocity as follows

$$\frac{\partial\boldsymbol{\Omega}}{\partial t}=\frac{\partial\boldsymbol{\omega}}{\partial s}+\boldsymbol{\omega}\times\boldsymbol{\Omega}. \tag{2.62}$$

Since we are aiming to derive an equation for the twist density Ω_3, the third component of equation (2.62) is particularly significant

$$\frac{\partial \Omega_3}{\partial t} = \frac{\partial \omega_3}{\partial s} + \Omega_1 \omega_2 - \Omega_2 \omega_1 . \tag{2.63}$$

Considering the definition of the Darboux vector (2.6), equation (2.63) can be rewritten purely in terms of the filament's shape and the angular velocity component ω_3

$$\frac{\partial \Omega_3}{\partial t} = \frac{\partial \omega_3}{\partial s} + \frac{\partial \boldsymbol{r}}{\partial s} \times \frac{\partial^2 \boldsymbol{r}}{\partial s^2} \cdot \frac{\partial}{\partial s} \frac{\partial \boldsymbol{r}}{\partial t} . \tag{2.64}$$

Equation (2.64) is sometimes called the condition of compatibility in the literature [6]. It is essentially a conservation law for the twist density which states that the filament can only twist for two reasons - either the angular velocity is non-uniform throughout the filament (the first term of equation (2.64)) or as the result of certain changes in the geometry of the filament involving a non-uniform linear velocity. The geometric interpretation of the second term of equation (2.64) is not intuitively straightforward and may benefit from the introduction of an additional mathematical concept called the writhe, because it turns out that the second term in the condition of compatibility essentially describes all the possible filament deformations which change the writhe of the filament.

In differential geometry and knot theory, the writhe is a quantity that essentially describes the amount of coiling in any closed, simple curve. The underlying theoretical material is quite rich and we recommend the extensive review article of Kamien [45] for a thorough treatment. For our purposes here, it is sufficient to note the integral definition of writhe for the case of an isolated space curve

$$Wr = \frac{1}{2\pi} \int_0^L \frac{\mathbf{e}_z (\mathbf{t} \times d\mathbf{t}/ds)}{1 + \cos(\theta)} ds, \tag{2.65}$$

where $\theta(s)$ is the angle between the tangent vector $\mathbf{t}(s)$ and the z axis in Cartesian coordinates. In numerical calculations involving situations in which the filament periodically forms loops the writhe is often useful as a quantitative metric of the evolution of the filament's shape [26].

Finally, we can rewrite the condition of compatibility in the form of a diffusion equation for the twist density that can be solved in conjunction with the filament's equation of motion that will be formulated in a subsequent chapter

$$\zeta_r \frac{\partial \Omega_3}{\partial t} = C \frac{\partial^2 \Omega_3}{\partial s^2} + \zeta_r \frac{\partial \boldsymbol{r}}{\partial s} \times \frac{\partial^2 \boldsymbol{r}}{\partial s^2} \cdot \frac{\partial}{\partial s} \frac{\partial \boldsymbol{r}}{\partial t}, \tag{2.66}$$

where $\zeta_r = 8\pi\eta a^3$ is the rotational friction coefficient.

We have now established the basic force densities acting on arbitrary inner points in the filament as well as the twist diffusion equation and can now proceed to formulating the equations of motion and the appropriate boundary conditions.

2.4 Equations of motion and hydrodynamic interactions

Now that we have developed a mathematical framework to describe the forces that change the shape of a flexible magnetic filament, it is possible to formulate the equations of motion that govern the overall dynamics of the system. The filament is immersed in an incompressible Newtonian fluid which is quiescent until perturbed by the deformation of the filament, which is in turn actuated by the external magnetic field. Naturally, when the filament deforms, the surrounding fluid exerts a force back on the filament, which in turn affects the filament's shape. Therefore, even in the case of a single filament, any movement of any element of the filament will induce an indirect effect, mediated by the fluid, on all other parts of the filament. This is what we refer to by the term *hydrodynamic interactions*. Furthermore, from a theoretical point of view, it makes no difference if our system consists of a single filament or an entire ensemble when it comes to describing hydrodynamic interactions, except insofar as we can make simplifying assumptions in limiting cases when different filaments are far from each other.

In the most general form, one may distinguish between three kinds of forces, which must sum to zero

$$\mathbf{F}_{viscous} + \mathbf{F}_{inertial} + \mathbf{F}_{filament} = \mathbf{0}, \tag{2.67}$$

where $\mathbf{F}_{filament}$ denotes the sum of all the internal forces acting on the filament. In general, to obtain the viscous and inertial forces it is necessary to analyze the motion of the fluid surrounding the filament.

To begin with, if we denote the fluid velocity vector field by $\boldsymbol{u}$ and the fluid density scalar field by ρ, the conservation of mass dictates the following continuity equation [48][50]

$$\frac{\partial \rho}{\partial t} + \boldsymbol{\nabla} \cdot (\rho \boldsymbol{u}) = 0, \tag{2.68}$$

where $\boldsymbol{\nabla}$ denotes the vector differential operator $\boldsymbol{\nabla} = \partial/\partial x\mathbf{i} + \partial/\partial y\mathbf{j} + \partial/\partial z\mathbf{k}$ and ρ is the fluid density. Since we have already stated our inclination to remain firmly in the realm of incompressible fluids, assuming $\rho = const$ in (2.68) immediately yields the condition of incompressibility

$$\nabla \cdot \mathbf{u} = 0, \tag{2.69}$$

which will remain in force throughout this work. However, we also need an equation of motion for the fluid. For an arbitrary fluid (unit) volume element, Newton's second law reads

$$\rho \frac{d\boldsymbol{u}}{dt} = \mathbf{f}_{hydrodynamic} + \mathbf{f}_{external} \tag{2.70}$$

and the hydrodynamic force may be expressed formally from the definition of the stress tensor

$$\mathbf{F}_{hydrodynamic} = \oiint\limits_{\partial V} (\boldsymbol{\sigma} \cdot \mathbf{n})\, d\partial V, \tag{2.71}$$

where $\boldsymbol{\sigma}$ denotes the second order stress tensor and $\mathbf{n}$ is the outer normal of the volume element. Using Gauss' theorem we can transform (2.71) into a volume integral

$$\mathbf{F}_{hydrodynamic} = \iiint\limits_{V} (\nabla \cdot \boldsymbol{\sigma})\, dV, \tag{2.72}$$

which enables us to reformulate (2.70) in the following form

$$\rho \frac{d\boldsymbol{u}}{dt} = \nabla \cdot \boldsymbol{\sigma} + \mathbf{f}_{external}, \tag{2.73}$$

where the derivative d/dt represents the total (also known as the substantive or convective) derivative $\partial/\partial t + \mathbf{u} \cdot \nabla$. The reasons for this and the general distinction between Lagrangian and Eulerian coordinates are well described in virtually all standard works on fluid dynamics (such as [48], [50] and many others) and will not be further detailed here.

As was already mentioned, the isotropic and Newtonian nature of the fluid will assumed for the entirety of this work. The hydrodynamic stress tensor therefore consists only of the hydrostatic pressure term and linear viscous stresses according to the stress-strain equation

$$\boldsymbol{\sigma} = -p\mathbf{I} + \eta \left(\nabla\mathbf{u} + (\nabla\mathbf{u})^T \right), \tag{2.74}$$

where $\mathbf{I}$ denotes the identity tensor, η is the (dynamic) fluid viscosity and $\nabla\mathbf{u}$ is the tensor gradient. The tensor gradient $\nabla\mathbf{u}$ can be expressed in component form as $(\nabla\mathbf{u})_{ij} = \partial u_j/\partial x_i$, with x_i denoting the i-th spatial coordinate.

Inserting the stress-strain equation (2.74) in (2.73) and noting the incompressible nature of the fluid we obtain the Navier-Stokes equation

$$\rho\left(\frac{\partial}{\partial t}+\mathbf{u}\cdot\boldsymbol{\nabla}\right)\mathbf{u}=\eta\boldsymbol{\nabla}^2\mathbf{u}-\boldsymbol{\nabla}p+\mathbf{f}_{external}. \tag{2.75}$$

Combined with the condition of incompressibility (2.69) the Navier-Stokes equation is sufficient to fully describe the motion of the fluid under the external (from the perspective of the fluid) force provided by the filament. It is, however, worth considering whether we actually need all of the complexity inherent in the Navier-Stokes equation to describe the behaviour of our system.

If we assume, as will be done throughout this work, no-slip boundary conditions between the surface of the filament and the surrounding fluid and denote the filament velocity by $\mathbf{v}=\frac{\partial\mathbf{r}}{\partial t}$ we can approximate the viscous and inertial forces to clarify equation (2.67)

$$\eta L\mathbf{v}+\rho L^2\mathbf{v}^2=\mathbf{F}_{filament}, \tag{2.76}$$

where L is the filament length. Given that typical sizes of the filaments discussed in this work are on the order of a few to a few hundred micrometers and filament velocities cannot be expected to exceed a fraction of the filament length per second, the viscous force is larger than the inertial force by a factor of a million at the very least, often even more. It is therefore reasonable to discard inertial effects as negligible.

It is common to denote the ratio of inertial and viscous forces using the Reynolds number

$$Re=\frac{\rho vL}{\eta}, \tag{2.77}$$

which in our case is expected to be roughly on the order of $Re\leq 10^{-6}$. In the limit of small Reynolds numbers the Navier-Stokes equation (2.75) reduces to the stationary Stokes equation [48], obtained by eliminating all the inertial terms

$$\eta\boldsymbol{\nabla}^2\mathbf{u}+\mathbf{f}_{external}=\boldsymbol{\nabla}p, \tag{2.78}$$

which, coupled with the condition of incompressibility (2.69) completely describes the motion of an overdamped, viscous (often called Stokesian) fluid under the influence of an external force. The term *Stokes equations* (note the plural) will be used throughout the remainder of this work to refer to the combination of the Stokes equation and the condition of incompressibility. The required boundary conditions are given simply by stating that the fluid velocity must match the velocity of the filament at the surface of the filament (no-slip boundary conditions). Note that the pressure variable is necessary to satisfy the condition of incompressibility (2.69). This kind of flow is often called creeping flow due to the fact that at macroscopic sizes such flows are typically very slow. Henceforth, all discussion of hydrodynamics in this work will assume Stokesian flow.

Two important observations about the Stokes equation are immediately apparent. First, it does not contain a derivative with respect to time: in the Stokesian regime all flows are stationary, thus momentum transfer is essentially instantaneous. Secondly, the Stokes equation is a linear equation. This is crucially important because the superposition of arbitrary many solutions of a linear differential equation constitutes a solution. One may therefore construct solutions to the Stokes equation in complicated circumstances as superpositions of simpler, known solutions. This fact underlies virtually all existing practical methods for describing Stokes flow in the presence of external forces, as direct analytical solutions are possible in only the most trivial cases.

In the simplest possible case, one may take a single point-like particle immersed in the fluid subject to a force $\mathbf{F}$, located at position $\mathbf{r}_0$. The fluid as a whole is therefore subject to the force density $\mathbf{f}(\mathbf{r}) = \mathbf{F} \cdot \delta(\mathbf{r} - \mathbf{r}_0)$, where δ denotes the Dirac delta function [38]. Considering the linearity of the Stokes equation, the fluid velocity field can be immediately written as

$$\mathbf{u}(\mathbf{r}) = \mathbf{G}(\mathbf{r} - \mathbf{r}_0) \cdot \mathbf{F}. \tag{2.79}$$

This velocity field is known as the stokeslet in the literature [54], while the mobility tensor is called the Oseen tensor. It is denoted with the capital G because, given the point-like perturbation of the otherwise quiescent fluid, it is by definition the Green function of the Stokes equation [4].

The crucial linearity of the Stokes equations lets us easily generalize this to a flow field corresponding to an arbitrary distribution of point-like forces

$$\mathbf{u}(\mathbf{r}) = \int \mathbf{G}(\mathbf{r} - \mathbf{r}') \cdot \mathbf{f}(\mathbf{r}') d\mathbf{r}'. \tag{2.80}$$

However, we have not yet specified the Oseen tensor. The classical approach [47] involves taking the Fourier transform of the Stokes equation and the incompressibility condition and utilizing the symmetries of the system to calculate the necessary integrals in Fourier space. In a similar approach, Zapryanov [79] used the fundamental solutions of the Laplace and biharmonic equations in Fourier space to circumvent the need for explicit integration. However, a more physically illustrative approach has been recently given by Dhont in his seminal textbook on the dynamics of colloid systems [21]. We will give an extremely brief overview of this derivation since the Oseen tensor is quite central to the topic of hydrodynamic interactions in Stokesian fluids, the interested reader may refer to the aforementioned textbook for a more complete treatment.

We begin by noting that an expression analogous to (2.80) exists for the pressure as well

$$p(\mathbf{r}) = \int \mathbf{g}(\mathbf{r}-\mathbf{r}') \cdot \mathbf{f}(\mathbf{r}') d\mathbf{r}', \tag{2.81}$$

where $\mathbf{g}(\mathbf{r}-\mathbf{r}')$ is usually called the pressure vector. It plays an analogous role to the Oseen tensor in (2.80), however since pressure is a scalar field, the quantity is a vector rather than a tensor. Noting that in this generalized case the force is distributed somewhere in the fluid and we therefore have $\mathbf{F} = \int \mathbf{f}(\mathbf{r}') \cdot \delta(\mathbf{r}-\mathbf{r}') d\mathbf{r}'$, we can insert (2.80) and (2.81) in the Stokes equations to obtain

$$\int \left(\boldsymbol{\nabla} \mathbf{g}(\mathbf{r}-\mathbf{r}') - \eta \boldsymbol{\nabla}^2 \cdot \mathbf{G}(\mathbf{r}-\mathbf{r}') - \mathbf{I} \cdot \delta(\mathbf{r}-\mathbf{r}') \right) \cdot \mathbf{f}(\mathbf{r}') d\mathbf{r}' = \mathbf{0} \tag{2.82}$$

from the Stokes equation itself (**I** denotes the identity tensor), whereas the condition of incompressibility yields

$$\int \left(\boldsymbol{\nabla} \cdot \mathbf{G}(\mathbf{r}-\mathbf{r}') \right) \cdot \mathbf{f}(\mathbf{r}') d\mathbf{r}' = 0. \tag{2.83}$$

Since (2.82) and (2.83) must hold for arbitrary force densities $\mathbf{f}(\mathbf{r}')$, the parts of those two expressions enclosed in the brackets must be equal to zero, thereby giving us explicit equations for the Green functions of the Stokes equations

$$\boldsymbol{\nabla} \mathbf{g}(\mathbf{r}-\mathbf{r}') = \eta \boldsymbol{\nabla}^2 \cdot \mathbf{G}(\mathbf{r}-\mathbf{r}') + \mathbf{I} \cdot \delta(\mathbf{r}-\mathbf{r}') \tag{2.84}$$

and

$$\boldsymbol{\nabla} \cdot \mathbf{G}(\mathbf{r}-\mathbf{r}') = 0. \tag{2.85}$$

Do note that the vector gradient $\boldsymbol{\nabla}\mathbf{g}(\mathbf{r}-\mathbf{r}')$ in (2.84) is in fact a tensor of rank two sometimes denoted $\boldsymbol{\nabla} \otimes \mathbf{g}(\mathbf{r}-\mathbf{r}')$ in the literature to clarify that point, since it may be seen as the dyadic product of the nabla operator and a vector. We may now apply the $\boldsymbol{\nabla}$ operator once more to take the divergence of (2.84) and find that the pressure vector must satisfy the following Poisson equation

$$\boldsymbol{\nabla}^2 \mathbf{g} = \boldsymbol{\nabla} \mathbf{I} \delta(\mathbf{r}), \tag{2.86}$$

which can be immediately solved using the fundamental solutions to the Laplace equation that are well described in standard mathematical literature [30] to yield

$$\mathbf{g} = \frac{\mathbf{r}}{4\pi r^3}. \tag{2.87}$$

The pressure vector can now be substituted directly into (2.84) to obtain

$$\nabla^2 \left(\frac{\mathbf{I}}{4\pi r} - \eta \mathbf{G}(\mathbf{r}) \right) = -\frac{1}{4\pi} \left(\frac{\mathbf{I}}{r^3} - \frac{3\mathbf{r} \otimes \mathbf{r}}{r^5} \right), \tag{2.88}$$

which after some algebraic manipulation to satisfy the boundary condition that the fluid is quiescent at infinity ($\mathbf{G}(\mathbf{r}) \to 0$ as $\mathbf{r} \to \infty$) yields the Oseen tensor

$$\mathbf{G}(\mathbf{r}) = \frac{1}{8\pi\eta} \left(\frac{\mathbf{I}}{r} + \frac{\mathbf{r} \otimes \mathbf{r}}{r^3} \right). \tag{2.89}$$

The Oseen tensor decays with increasing distance as $1/r$, showing the rather long range character of hydrodynamic interactions. This is one of the main reasons why relatively accurate modelling of hydrodynamic interactions is crucial to understanding the behaviour of complex systems in Stokes flows.

As we've already mentioned, because of the linearity of the Stokes equations, it is in principle possible to construct any Stokes flow from an appropriate contribution of stokeslets. Nevertheless, for the sake of completeness we should mention that it is sometimes considered illustrative to utilize derivatives of the stokeslet to describe the nature of relatively simple Stokes flows [23] in the form of a Taylor expansion of a stokeslet around the center of a geometric body. This is sometimes referred to as the multipole expansion of Stokes flow [47] in analogy to classical electromagnetism. In such an expansion, the presence of a single force is described by a monopole solution (which is simply the stokeslet), two forces give rise to a dipole, four cause a quadrupole, etc. For instance, one may write the Stokes dipole [74] as

$$\mathbf{u}_{dipole} = \frac{1}{8\pi\eta} \left(-\frac{\mathbf{F} \cdot \mathbf{d}}{r^3} + \frac{3(\mathbf{F} \cdot \mathbf{r})(\mathbf{d} \cdot \mathbf{r})}{r^5} \right) \cdot \mathbf{r} + \frac{1}{8\pi\eta} \left(\frac{(\mathbf{d} \times \mathbf{F}) \times \mathbf{r}}{r^3} \right), \tag{2.90}$$

where $\mathbf{d}$ denotes the vector between the two forces. The first term in (2.90) is often referred to as the stresslet [54], whereas the second term is called the rotlet. The rotlet is notable for being the lowest order multipole expansion term that exerts any net torque on the fluid.

It is also worth remarking that the Oseen tensor has an obvious singularity at $r = 0$. This causes certain issues in numerical methods based on integrating distributions of stokeslets such as the boundary integral approach [72] and imposes constraints on the computational efficiency of such methods. This is largely addressed by the method of regularized stokeslets [19], where the delta function used to obtain (2.79) is replaced by a smoothed out regularized function leading to exact regularized replacements for all of the multipole expansion terms without any singularities.

More generally, considering the linearity of the Stokes equation, we may express the linear and angular velocities of an arbitrary segment of the filament as follows

$$\mathbf{v}_i = \sum_j \left(\boldsymbol{\mu}_{ij}^{(tt)} \cdot \mathbf{F}_j + \boldsymbol{\mu}_{ij}^{(tr)} \cdot \mathbf{T}_j \right), \tag{2.91}$$

$$\boldsymbol{\omega}_i = \sum_j \left(\boldsymbol{\mu}_{ij}^{(rt)} \cdot \mathbf{F}_j + \boldsymbol{\mu}_{ij}^{(rr)} \cdot \mathbf{T}_j \right), \tag{2.92}$$

where $\mathbf{F}_j$ and $\mathbf{T}_j$ denote the force and torque acting on the particular segment of the filament; $\boldsymbol{\mu}_{ij}^{(tt)}$, $\boldsymbol{\mu}_{ij}^{(tr)}$, $\boldsymbol{\mu}_{ij}^{(rt)}$, $\boldsymbol{\mu}_{ij}^{(rr)}$ are four 3 x 3 mobility tensors and the sums run over the entire filament. These tensors are all symmetrical, as a consequence of the Lorentz reciprocal theorem (for a complete treatment see [41]).

Seeing as how in practice the mobility tensors can only be computed on the basis of known analytical solutions to the Stokes equation (2.78), we have in effect established a natural discretization of the filament in the form of N identical spheres. These and subsequent expressions regarding the properties of these mobility tensors are therefore not specific to filaments, but rather pertain to arbitrary configurations of spheres or anything that can be approximated as such. However, given that internal segments in our filament only rotate as an effect of twist (see Section 2.3), we need only consider the linear velocities, reducing the number of necessary mobility tensors to one: $\boldsymbol{\mu}_{ij}^{tt}$, which will be denoted $\boldsymbol{\mu}_{ij}$ from now on. This yields the general equation of motion that will be used throughout this work

$$\mathbf{v} = \boldsymbol{\mu} \cdot \mathbf{f}. \tag{2.93}$$

Furthermore, the mobility tensor is also positive definite. This may be seen from a purely physical consideration: the energy dissipated in the fluid per unit of time is $\sum_i (\mathbf{F}_i \cdot \mathbf{v}_i) = \mathbf{f} \cdot \mathbf{v} = \mathbf{f} \cdot \boldsymbol{\mu} \cdot \mathbf{f}$ and must be positive, therefore the mobility tensor is positive definite. This property is very useful for the efficient numerical calculation of mobility tensors for arbitrary filament configurations (or, more generally, arbitrary collections of spheres in 3D space).

We have in effect already calculated the mobility tensor $\boldsymbol{\mu}$ for a particularly simple case: a situation where we have two point-like particles, one of which is acted upon by an external force and the other being free from external influence. In this case $\boldsymbol{\mu}_{ij} = \mathbf{G}(\mathbf{r}_{ij})$ with $\mathbf{r}_{ij} = \mathbf{r}_2 - \mathbf{r}_1$ and $\boldsymbol{\mu}_{ii} = \frac{\mathbf{I}}{6\pi\eta a}$, which is simply the inverse of the well known hydrodynamic drag coefficient for a single sphere in Stokes flow. This is a complete description for the case of two point-like particles, since point-like particles cannot rotate and therefore higher order multipole terms are irrelevant. The only caveat is that the particles cannot be closer than $1.5a$, as the Oseen tensor loses the positive definiteness that we already showed to be necessary for retaining physical behaviour. This can be remedied by using regularized modifications of the Oseen tensor [19] or other corrections that take into account the finite (non-zero) size of the particles.

Unfortunately, this approach cannot be directly generalized to the vastly more complicated case of a discretized filament of arbitrary shape (effectively, an arbitrary configuration of finite size spheres) in analytic form. It is possible to make considerable headway by considering asymptotic expansions for slightly more complicated geometries involving fairly thin bodies such as prolate spheroids and cylinders and matching coefficients with far-field expansions of Stokes flow. This lead to the slender body theory of Keller and Rubinow [46] which involves solving boundary integral equations for the force exerted by the body on the fluid. This approach was later improved and extended by Shelley [69], partly addressing certain numerical challenges involving the evaluation of integrals with nearly singular kernels at certain points. The method of regularized stokeslets of Cortez [19] can also be interpreted as an alternative reformulation of slender body theory addressing many of the same concerns cited by Shelley [69] using different means to achieve similar ends. Ultimately, all versions of slender body theory share the problem of limited scalability to large problems, due to the need to numerically solve computationally intensive boundary integral equations for each filament configuration. Since we do not directly employ slender body theory in this work, we will only discuss the limiting case of an asymptotically thin filament which leads to a fully local approximation of hydrodynamic interactions known as resistive force theory.

Resistive force theory was first derived in the seminal paper of Gray and Hancock [40] in 1955. They analyzed the propulsive behaviour of sea-urchin spermatozoa and used the empirical observation of a travelling wave across the tail of the spermatozoon to derive an effective anisotropy between the friction coefficients felt by the organism in different directions on motion. Two decades later, in his 1975 John von Neumann lecture on flagellar hydrodynamics Lighthill [54] derived more precise expressions for the values of normal and tangential friction coefficients after identifying resistive force theory as a particular limiting case of the slender body approach. In particular, Lighthill showed that for an asymptotically thin filament the friction coefficients for the normal and tangential directions can be expressed as

$$\zeta_n = \frac{4\pi\eta}{\log(2q/a) + 1/2}, \tag{2.94}$$

$$\zeta_t = \frac{2\pi\eta}{\log(2q/a)}, \tag{2.95}$$

where $q = 0.09\lambda$, λ is the wavelength of the helical distribution of stokeslets measured along the center line of the filament and a is the radius of the filament. Obviously, as the λ values are difficult to determine when examining arbitrary configurations of filaments without prior experimental guidance, the exact values of the friction coefficients are difficult to estimate with any accuracy. Nevertheless, the asymptotic behaviour is clear: as the filament radius a tends to zero, the friction anisotropy ratio ζ_n/ζ_t tends to 2. The convergence of the asymptotic behaviour is only logarithmic, however, meaning that for any finite values of the filament radius a the anisotropy ratio will likely be considerably smaller. Nevertheless, this resistive force theory approach provides an extremely convenient if imprecise approximation to hydrodynamic interactions due to being entirely local and very cheap computationally. It has therefore enjoyed very widespread use in the scientific research of flexible filaments in Stokesian fluids and will also be used extensively throughout this work, although we will compare the results to more sophisticated approaches whenever it is feasible to do so.

While the derivation of Lighthill [54] is quite laborious and will not be detailed here, the asymptotic behaviour can be seen in a fairly straightforward fashion. Let us consider a distribution of stokeslets along the center line of a thin filament oriented along the x axis in Cartesian coordinates. Since the filament is thin and no slip boundary conditions are in effect, we may reasonably expect the fluid velocity close to any arbitrary line element to be close to that induced by a stokeslet of appropriate strength. The filament is given by the position vector $\mathbf{r}(s) = (r_x(s), r_y(s), r_z(s)) = (r_1(s), r_2(s), r_3(s))$ with the filament radius given by $a^2(s) = r_2^2(s) + r_3^2(s)$. We will also make an exception to the kinematic framework outlined in Section 2.2 and set the arclength to the range $(-L, L)$, so the filament length is $2L$ in this case, following the approach outlined by Batchelor [3]. This is done because having symmetric integration limits greatly simplifies the algebraic manipulations required to derive the result we are looking for and is unequivocally the better choice for this problem. Considering equation (2.80) we can express the fluid velocity using the Oseen tensor

$$u_i(\mathbf{r}) = \frac{1}{8\pi\eta}\int_{-L}^{+L}\left(\frac{f_i(r_1')}{\left((r_1-r_1')^2+a^2\right)^{1/2}} + \frac{(r_i-r_i')(r_j-r_j')f_j(r_1')}{\left((r_1-r_1')^2+a^2\right)^{3/2}}\right)dr_1', \tag{2.96}$$

where the indices i and j take the values 1, 2, 3. Assuming an initially quiescent fluid, (2.96) represents an integral equation for the force densities associated with the stokeslets and therefore also for the friction coefficients of the filament. While this cannot be solved analytically, we can nevertheless analyze the asymptotic behaviour of the solution as the ratio $\frac{a}{L}$ tends to zero for an asymptotically thin filament. It is evident from (2.96) that the asymptotic solution is determined by four integrals

$$I_1 = \int_{-L}^{+L} \frac{dr_1'}{\left((r_1 - r_1')^2 + a^2\right)^{1/2}}, \tag{2.97}$$

$$I_{2,3,4} = \int_{-L}^{+L} \frac{(r_1 - r_1')^n}{\left((r_1 - r_1')^2 + a^2\right)^{3/2}} dr_1', \tag{2.98}$$

where $n = 0, 1, 2$. The integrals themselves are trivial to calculate, but the asymptotic behaviour is worth looking at in more detail. For the first integral we get

$$I_1 = \log \frac{r_1 + L + \left(a^2 + (L + r_1)^2\right)^{1/2}}{r_1 - L + \left(a^2 + (L - r_1)^2\right)^{1/2}}. \tag{2.99}$$

Dividing both the numerator and denominator by L and utilizing the fact that for an arbitrary α and a real, analytic function x the expression $\alpha + (\alpha^2 + x^2)^{1/2}$ can be expanded in the Taylor series (up to second order) $(\alpha + |\alpha|) + \frac{x^2}{2|\alpha|} + O(x^4)$ we can expand (2.99) into a power series of the ratio a/L up to second order

$$I_1 = \log \frac{2\frac{L+r_1}{L} + \left(\frac{r_1}{L}\right)^2 \frac{1}{2\frac{L+r_1}{L}}}{\left(\frac{r_1}{L}\right)^2 \frac{1}{2\frac{L-r_1}{L}}}, \tag{2.100}$$

where we have also utilized the fact that $\left|\frac{r_1+L}{L}\right| = \frac{r_1+L}{L}$ and $\left|\frac{r_1-L}{L}\right| = \frac{L-r_1}{L}$. After algebraic simplification we get

$$I_1 = \log \left(\frac{-4(r_1^2 - L^2)}{a^2} - \frac{r_1 - L}{r_1 + L} \right), \tag{2.101}$$

where the second term can be neglected in the limit of asymptotically small ratios a/L. Dividing both the numerator and denominator by a generalized average filament radius a_0 to account for the fact the a need not be constant everywhere and further simplifying, we get Batchelor's result [3]

$$I_1 = 2\log \frac{2L}{a_0} + 2\log \frac{\left(1 - \frac{r_1^2}{L^2}\right)^{1/2}}{a/a_0}. \tag{2.102}$$

Following a perfectly analogous process for the other integrals (although one involving a slightly more laborious process of algebraic manipulation) we obtain $I_2 = 2, I_3 = 0, I_4 = I_1 - 2$.

Substituting these results in (2.96) we get a second order asymptotically correct (disregarding boundary effects at the ends) expression for the fluid velocity induced by a uniformly dense stokeslet distribution along a thin filament

$$u_i(\mathbf{r}) = \frac{1}{4\pi\eta\varepsilon}\left(f_i + \delta_{1i} f_1 + |\mathbf{f}| O(\varepsilon)\right), \tag{2.103}$$

where $\varepsilon = \frac{a_0}{2\log 2L}$. We have therefore showed that $f_1 = 2\pi\eta\varepsilon u_1$, $f_2 = 4\pi\eta\varepsilon u_2$ and $f_3 = 4\pi\eta\varepsilon u_3$. Thus, for an asymptotically thin filament up to a certain approximation it is reasonable to state that the ratio of friction coefficients $\zeta_n/\zeta_t \rightarrow 2$, which was our goal. As was already mentioned, Lighthill (and others after him) have improved upon the accuracy of the resistive theory approach outlined here, but the relative simplicity of the method has kept it in widespread use and it remains a useful first approximation to hydrodynamic interactions.

Unlike the full framework of slender body theory, which would require us to solve boundary integral equations simultaneously with a set of equations for the filament shape (or, as in the case of some current approaches in the regularized stokeslets method [70], add an additional corrective integral term to the equations of motion), resistive force theory lets us easily formulate a friction tensor (the inverse of the mobility tensor) for the equation of motion (2.93)

$$\boldsymbol{\mu}^{-1} = \zeta_n\left(\mathbf{I} + \frac{\zeta_t - \zeta_n}{\zeta_n}\frac{\partial \mathbf{r}}{\partial s} \otimes \frac{\partial \mathbf{r}}{\partial s}\right), \tag{2.104}$$

with the additional note that, as will be seen later, after the equations of motion are cast in dimensionless form, only the ratio ζ_n/ζ_t remains as the sole free parameter in the mobility tensor, thereby avoiding the need to explicitly calculate the friction coefficients.

The preceding description of Stokesian hydrodynamics has established an exact description of the hydrodynamic interactions in the simple case of two spheres through the Oseen tensor and an approximate description of the case of more complicated bodies in the form of slender body theory. However, this is approach necessarily limited to fairly simple bodies and the general problem is analytically intractable. It is, however, possible to extend the approach used for the Oseen tensor to the case of many spheres and thereby model more complicated bodies as a discrete collection of spheres. This leads to two distinct methods known as the method of reflections and the method of induced forces. We will briefly describe the theoretical underpinnings of both, focusing primarily on the method of reflections since it is used far more extensively in this work.

The idea behind the method of reflections is essentially to iteratively calculate the flow field induced by arbitrarily many spheres in a series of corrective terms under the approximation that additional spheres essentially reflect the flow field from one sphere to the next. The theoretical foundation for this is given by the well known theorems of Faxen [41] which for the case of a translating sphere (with radius a) in Stokes flow yield

$$\mathbf{v}_{sphere} = \mu^t \mathbf{F}_{sphere} + \left(1 + \frac{1}{6} a^2 \boldsymbol{\nabla}^2\right) \mathbf{u}(\mathbf{r})|_{\mathbf{r}=\mathbf{r}_{sphere}}, \tag{2.105}$$

where $\mathbf{u}(\mathbf{r})|_{\mathbf{r}=\mathbf{r}_{sphere}}$ denotes the fluid velocity at the surface of the sphere.

A similar law exists for the case of rotational motion, but due to the restrictions mentioned previously we remain within the realm of translational motion here.

In a system of N spheres, any given sphere i acted upon by a force $\mathbf{F}_i$ and located in an entirely quiescent fluid moves according to Stokes' law

$$\mathbf{v}_i^{(0)} = \mu^t \mathbf{F}_i = (6\pi\eta a)^{-1} \mathbf{F}_i. \tag{2.106}$$

Since in a real system of N potentially moving spheres, the flow field will in general assume non-zero values, Stokes' law essentially gives a zeroth order approximation (referred to as the particle self-interaction) to the velocity of any sphere which we will refer to as $\mathbf{v}^0$. Any movement of a single sphere will necessarily impact the motion of any nearby spheres, the velocity of which is directly given by Faxen's theorem (2.105)

$$\mathbf{v}_j^{(1)} = \mu^t \mathbf{F}_j + \left(1 + \frac{1}{6} a^2 \boldsymbol{\nabla}^2\right) \mathbf{u}^{(0)}(\mathbf{r})\Big|_{\mathbf{r}=\mathbf{r}_j}, \tag{2.107}$$

where $\mathbf{u}^{(0)}(\mathbf{r})$ refers to the flow field induced by the sphere velocity $\mathbf{v}_i^{(0)}$. It may be said that the sphere j essentially reflects the flow induced by the movement of sphere i, thereby inducing an appropriate flow field $\mathbf{u}^{(1)}(\mathbf{r})$, with the total flow field being equal to the superposition of the two flows $\mathbf{u}^{(0)}(\mathbf{r})$ and $\mathbf{u}^{(1)}(\mathbf{r})$ due to the linearity of the Stokes equations

$$\mathbf{u}(\mathbf{r}) = \mathbf{u}^{(0)}(\mathbf{r}) + \mathbf{u}^{(1)}(\mathbf{r}). \tag{2.108}$$

The new flow field $\mathbf{u}^{(1)}(\mathbf{r})$, however, now violates the boundary conditions of the original sphere i, requiring a further correction. This may once again be calculated from Faxen's theorem (2.105), taking care to omit the self-interaction term which has already been accounted for both spheres

$$\mathbf{v}_i^{(2)} = \left(1 + \frac{1}{6} a^2 \boldsymbol{\nabla}^2\right) \mathbf{u}^{(1)}(\mathbf{r})\Big|_{\mathbf{r}=\mathbf{r}_i}, \tag{2.109}$$

which again creates a reflected flow field $\mathbf{u}^{(2)}(\mathbf{r})$ that violates the boundary conditions of sphere j and so forth. In effect, we have created an infinite series of corrective terms for the total flow field

$$\mathbf{u}(\mathbf{r}) = \mathbf{u}^{(0)}(\mathbf{r}) + \mathbf{u}^{(1)}(\mathbf{r}) + \mathbf{u}^{(2)}(\mathbf{r}) + ... \tag{2.110}$$

and similarly for the velocities of the individual spheres. This in effect constitutes a power series in terms of the inverse dimensionless particle distance ratio $\frac{a}{r_{ij}}$ (where $r_{ij} = |\mathbf{r}_j - \mathbf{r}_i|$) which has been shown to be unconditionally convergent [56].

Before elaborating on the specifics of calculating the terms of the series (2.110) we must also remark that the series as given here only involves two sphere interactions. In truth, given a system of more than two spheres any flow reflected by an arbitrary sphere exerts an influence on every single constituent of the whole system. These kinds of many body interactions can also be included in the expansion, though it requires significant additional effort and comes at a considerable computational cost (see the excellent textbook of Dhont [21] for a comprehensive treatment of three body interactions).

For the purposes of this work (and most practical uses of the method of reflections found in current scientific literature), it is sufficient to consider the truncated (up to order $(a/r_{ij})^3$) two body mobility tensor known as the Rotne-Prager-Yamakawa tensor [21]:

$$\mu_{ij} = \left(\mathbf{I} + \frac{a^2}{6}\nabla^2\right)\mathbf{G}(\mathbf{r}_{ij}) = \frac{1}{8\pi\eta r_{ij}}\left(\left(1 + \frac{2a^2}{3r_{ij}^2}\right)\mathbf{I} + \left(1 - \frac{2a^2}{r_{ij}^2}\right)\mathbf{r}_{ij} \otimes \mathbf{r}_{ij}\right), \tag{2.111}$$

where the vector $\mathbf{r}_{ij} = (\mathbf{r}_j - \mathbf{r}_i)/r_{ij}$, the scalar quantity $r_{ij} = |\mathbf{r}_{ij}|$ and the whole expression is valid for the case where $r_{ij} > 2a$ for all values of the indices i and j which run over the entire system of arbitrarily many spheres. For (partially or completely) overlapping spheres, the following formulation of the mobility tensor has been shown to be in effect [75]

$$\mu_{ij} = \frac{1}{6\pi\eta a}\left(\left(1 - \frac{9r_{ij}}{32a}\right)\mathbf{I} + \frac{3r_{ij}}{32a}\mathbf{r}_{ij} \otimes \mathbf{r}_{ij}\right). \tag{2.112}$$

Do note that that in the limit of self-interaction when $r_{ij} \to 0$ the expression (2.112) reduces to the standard single sphere mobility of Stokes.

The tensors (2.111) and (2.112) were originally derived using a variational approach by Rotne and Prager [68] and independently by Yamakawa [78]. Since such an approach intrinsically attempts to minimize energy dissipation, the Rotne-Prager-Yamakawa tensor essentially provides an upper bound to the mobility coefficients. There also exist expressions derived much later [75] for hydrodynamic interactions involving rotating spheres, which will not be used in this work for the reasons stated in previous chapters. It can also be shown [75] that both expressions of the Rotne-Prager-Yamakawa tensor are positive definite for all values of r_{ij}, which greatly aids efficient numerical computation of its components. The computational aspects of this and other hydrodynamic approximations will be further explored in Chapter 3.

There remains one final common method of hydrodynamic approximation we have not yet described, known as the method of induced forces. The idea here is to consider the effect of finite sized spheres located within the fluid in terms of the reactive forces induced upon the fluid by the no-slip boundary conditions in effect on the surfaces of said spheres. One may therefore solve the fluid Stokes equations with the additional force density that is the (vectorial) sum of all the individual force densities chosen so that each fluid element located within a sphere would move with the velocity of the sphere in question: $\mathbf{u}(\mathbf{r}_i + \mathbf{r}_0) = \mathbf{v}_i$ for each $|\mathbf{r}_0| \leq a$ for all $i = 1, 2, ..., N$. The traditional approach of the method of induced forces now calls for expanding the the standard expression for the Stokesian fluid flow (2.80) in terms of vector spherical harmonics [42] and formulating an infinite set of algebraic equations for the coefficients of vector spherical harmonics that in turn determine the fluid flow. Since we employ a previously published and rather well known implementation of this method [44] in this work, we will give a brief overview of the formal approach employed in this implementation. We will not detail the basic concepts of multipole expansions, which are well known in physics. Readers interested in the mathematical basis of irreducible representations of multipole moments are referred to [31].

To utilize the notation of Cichocki *et al* [18], the $(p+1)$ rank force multipole tensor may be written as a function of the individual force density of sphere i as

$$\mathbf{F}^{(p+1)} = \frac{1}{p!} \int \mathbf{r}^{(p)} \mathbf{f}(\mathbf{r}) d\mathbf{r}, \tag{2.113}$$

where $\mathbf{r}^{(p)}$ denotes the p-fold direct product of the position vectors $\mathbf{r}$. The set of irreducible multipole moments is denoted as $\mathbf{f}_{lm\sigma}$ for the indices $l = 1, 2, ...,$ $m = -l, -l+1, ..., l-1, l,$ $\sigma = 0, 1, 2,$ where the three components of $\mathbf{f}_{1m0}$ correspond to the Cartesian components of the total force $\mathbf{F}_i$ exerted on the fluid by the sphere i according to $\mathbf{F}_i = \int \mathbf{f}_i d^3 r$. The force multipole moments may be arranged in an infinite dimensional vector $\mathbf{g}_i = \left(\mathbf{F}_i, \mathbf{T}_i, \mathbf{g}_h^{(0)}, \mathbf{g}_h^{(1)}, ...\right)$, where $\mathbf{g}_h$ formally denotes the higher order multipole components. These may be eliminated by defining the operator P_j which projects the multipole vector $\mathbf{g}_i$ onto the force-torque subspace of the i-th sphere.

An analogous multipole expansion may be written for the velocities, yielding an equivalent infinite dimensional multipole vector $\mathbf{c}_i$, which under projection gives

$$P_i\mathbf{c}_i = \left(\mathbf{u}_i - \mathbf{v}_i(\mathbf{r}_i), \boldsymbol{\omega}_i - \frac{1}{2}\boldsymbol{\nabla}\times\mathbf{v}(\mathbf{r}_i), \mathbf{0}, \ldots\right). \tag{2.114}$$

The multipole vectors are related by the single sphere extended friction matrix $\mathbf{Z}$

$$\mathbf{f}_i = \mathbf{Z}_i\mathbf{c}_i. \tag{2.115}$$

The vector $\mathbf{c}_i$ can be decomposed $\mathbf{c}_i = \mathbf{c}_i^{(0)} - \mathbf{c}_i^{+}$, with $\mathbf{c}_i^{(0)} = (\mathbf{u}_i, \boldsymbol{\omega}_i, \mathbf{0}, \ldots)$. The first vector is known, the second may be expressed as

$$\mathbf{c}_i^{+} = \sum_{j=1}^{N} G_{ij}\mathbf{f}_j, \tag{2.116}$$

where G_{ij} is called the Green matrix, which is a function of the geometry of the problem. Substituting (2.116) and the decomposition of the velocity multipole vector into (2.115) we obtain an exact set of multipole equations in the form

$$\mathbf{f}_i = \mathbf{Z}_i\left(\mathbf{c}_i^{(0)} - \sum_{j=1}^{N} G_{ij}\mathbf{f}_j\right). \tag{2.117}$$

Formally, the solution of (2.117) can be easily expressed in matrix form

$$\mathbf{f} = \mathbf{Z}\left(\mathbf{I} + \mathbf{G}\mathbf{Z}\right)^{-1}\mathbf{c}^{(0)}, \tag{2.118}$$

which leads to the actual friction matrix through the projection operator defined previously

$$\boldsymbol{\zeta} = \mathbf{P}\mathbf{Z}\left(\mathbf{I} + \mathbf{G}\mathbf{Z}\right)^{-1}\mathbf{P}. \tag{2.119}$$

While the solution (2.119) is exact, practical calculation requires truncating the infinite multipole series at some finite order, yielding an approximation scheme for the friction (and therefore mobility) tensors for arbitrary collections of spheres in a Stokesian fluid. We utilize the freely available software library *HYDROLIB* [44] for this purpose, with minor code modifications to facilitate interoperability with our codebase and to be able to use modern compilers (see Chapter 3 for details). This library has been extensively verified and its results compared to experiments as well as direct numerical simulation (DNS) approaches [60], which makes it immensely useful for benchmarking the accuracy of simpler hydrodynamic approximations.

This concludes our brief overview of the basic methods for approximating hydrodynamic interactions. Given the equation of motion (2.93) and the various methods for calculating the mobility tensor we have presented in this section, we only need to derive appropriate boundary conditions to have a complete theoretical model for a single magnetoelastic filament immersed in a Stokesian fluid. Accordingly, this is the subject of the next section.

2.5 Boundary conditions

The purpose of this section is to develop the general form of the boundary conditions relevant to the physical situations considered in this work using the variational derivations of force densities from (2.46) and Appendix B. The implementation details are left for chapter 3 as part of the description of the numerical model.

In general, the ends of the filament can be either free or constrained. Although several types of constraints are possible in principle, we will only explicitly derive the case of a completely fixed end (to be used for modeling artificial cilia), as other types of constraints are straightforward to implement in an analogous fashion. Given the equations of motion (2.93) and (2.66) developed in the previous section, which is a system of two non-linear partial differential equations, a fourth order equation of motion coupled with a second order diffusion equation for the twist density, we need six boundary conditions (four for the radius vector and/or its spatial derivatives and two for the twist density and/or its spatial derivatives) and two initial conditions for the problem to be fully specified.

In the case of free ends, by definition, forces and torques on the ends are zero. Thus, the curvature and twist density are also equal to zero:

$$\kappa|_0^L = \left.\frac{\partial^2 \mathbf{r}}{\partial s^2}\right|_0^L = 0, \tag{2.120}$$

$$\Omega_3|_0^L = 0. \tag{2.121}$$

This immediately gives us four out of the six necessary boundary conditions. The remaining two may be obtained by considering the expressions for the force densities derived in Section 2.3 and Appendix A and noting that in the case of free ends the total force on each end must be equal to zero

$$\left.\left(-A\frac{\partial^3 \mathbf{r}}{\partial s^3} + \Lambda\frac{\partial \mathbf{r}}{\partial s} + \mathbf{F}_{magnetic} + C\Omega_3\frac{\partial \mathbf{r}}{\partial s} \times \frac{\partial^2 \mathbf{r}}{\partial s^2}\right)\right|_0^L = 0. \tag{2.122}$$

The case of a single fixed end is best handled numerically by fixing the position of an end and introducing an appropriate discrete reaction force on neighboring segments of the filament. This is described further in Chapter 3 along with the discretization of the equations of motion and the formulation of the numerical model.

Chapter 3

Numerical model: methodology and implementation

In the previous chapter we established a comprehensive theoretical framework for describing the motion of a single magnetically actuated filament immersed in a Stokesian fluid. However, since the equations of motion obtained there are not amenable to analytic solution, a numerical framework must be developed in order to obtain actual results. In doing so, we will also see how the case of arbitrary many filaments can be seen as a natural extension of the numerical model described in this chapter, thereby giving us the ability to model the ensemble dynamics of magnetic filaments to a reasonable degree of approximation.

3.1 Discrete equations of motion and numerical implementation

In order to obtain a numerically tractable set of equations of motion for the filament described in Chapter 2, we must first discretize the filament. To do so, we divide the filament in p segments of equal length h. The continuous partial differential equations of Chapter 2 will thereby be replaced by a set of algebraic equations describing the dynamics of $p+1$ marker points.

Before proceeding further we also cast the equations of motion in dimensionless form. Length and time are scaled by the filament length L and the characteristic elastic relaxation time $t_e = \zeta_n L^4/A$ respectively. Consequently, the principal dimensionless parameters controlling the dynamics of the filament are the magnetoelastic number Cm (this is the ratio of the magnetic and elastic forces; for instance, in the ferromagnetic case $Cm = MHL^2/A$) and the ratio of the filament length L and the characteristic elastic penetration length $L_e = (A/\zeta_n \omega)^{1/4}$.

The magnetoelastic number is simply the ratio of the magnetic and elastic forces, with M as the magnetization per unit length. The dimensionless frequency of the external magnetic field is therefore given by $\tilde{\omega} = (L/L_e)^4$.

The equations of motion from Chapter 2 may be formally written in a discretized dimensionless form (omitting the tension term which will be handled separately) as

$$\mathbf{v}_i = \boldsymbol{\mu}_i \left(-D_b^{(4)}\mathbf{r} + \mathbf{f}_{magnetic} + D_{tw}^{(1)} (\Omega_3 D^{(1)}\mathbf{r} \times D^{(2)}\mathbf{r}) \right), \tag{3.1}$$

$$\frac{\partial \Omega_3}{\partial t} = d_0 D_{tw}^{(2)} \Omega_3 + \left(D^{(1)}\mathbf{r} \times D^{(2)}\mathbf{r} \right) \cdot D^{(1)}\mathbf{v}, \tag{3.2}$$

where the index $i = 1, 2, ..., p+1$ runs over all the marker points of the filament, $d_0 = C/\zeta_r$ denotes the dimensionless twist diffusion constant while the operators $D^{(1)}$, $D^{(2)}$ and $D^{(4)}$ denote the appropriate order finite differentiation matrices with the property that $D^{(n)}\mathbf{r} \approx \frac{\partial^n \mathbf{r}}{\partial s^n}$. All of the terms in equations (3.1) and (3.2) as well as in the remainder of this work are written in dimensionless form. In terms of implementation, the differentiation operators need to handle both scalar arrays such as $(\Omega_3)_i$ and lists of vectors like $\mathbf{r}_i$, so all lists of vectors are represented as scalar arrays of size $3 \times n$ with the structure $(x_1, y_1, z_1, x_2, y_2, z_2, ..., x_n, y_n, z_n)$ for an arbitrary list of n vectors $\mathbf{r}_i = (x_i, y_i, z_i)$. While the standard finite difference expressions are well known in the literature [1], we also need to take into account the boundary conditions, which is reflected with the appropriate subscripts for the operators $D_b^{(4)}$, $D_{tw}^{(2)}$, $D_{tw}^{(1)}$. This process is outlined in Appendix B.

The magnetic term $\mathbf{f}_{magnetic}$ is easy to handle. In the ferromagnetic case, as was discussed in Chapter 2, the force only acts on the ends of the filament so that in dimensionless form we simply have $\mathbf{F}_{magnetic}\big|_{i=1} = Cm\mathbf{h}$ and $\mathbf{F}_{magnetic}\big|_{i=p+1} = -Cm\mathbf{h}$. In the superparamagnetic case we obtain

$$\mathbf{f}_{magnetic}\big|_{i=2,...,p} = -2Cm \left(\mathbf{h} \cdot D^{(2)}\, \mathbf{r}\big|_{i=2,...,p} \right), \tag{3.3}$$

$$\mathbf{F}_{magnetic}\Big|_{i=1}^{i=p+1} = \left(2Cm(\mathbf{h} \cdot D_m^{(1)}\mathbf{r})\mathbf{h} \right)\Big|_{i=1}^{i=p+1}. \tag{3.4}$$

Note that once again the operator $D_m^{(1)}$ must be formulated in such a way as to incorporate the boundary conditions in the finite differentiation formulation (see Appendix C for implementation details).

Since we neglected to include the tension term in (3.1), we need to handle the condition of inextensibility separately. Although one approach would be to include the tension force density in the equation of motion and then solve a discretized version of the tension equation (2.59), there is another approach that will serve us much better here.

In the case of a discretized filament the condition of incompressibility (2.69) can be reformulated in a useful fashion to further explore the role of the internal tension $\Lambda(s)$. If the filament is discretized by $p+1$ marker points, incompressibility may be enforced by p constraints

$$g_i = (\mathbf{r}_{i+1} - \mathbf{r}_i)^2 = h^2, \tag{3.5}$$

where the index $i = 1, 2, ..., p$. If we now define the $p \times 3(p+1)$ Jacobian matrix of constraints with the components

$$J_{ij} = \frac{\partial g_i}{\partial \mathbf{r}_j}, \tag{3.6}$$

we obtain a new form for the condition of incompressibility, one that is reminiscent of the condition of incompressibility in fluid dynamics

$$\mathbf{J} \cdot \mathbf{v} = 0. \tag{3.7}$$

For the sake of clarity, let us now write an arbitrary part of the (transposed) Jacobian matrix explicitly, using x_i, y_i and z_i to denote the appropriate components of the position vector $\mathbf{r}_i = (x_i, y_i, z_i)$

$$J_{ij}^T = \begin{pmatrix} \vdots & \vdots & \vdots & \vdots & \vdots & \vdots & \vdots & \vdots \\ \cdots & -2(x_j - x_i) & -2(y_j - y_i) & -2(z_j - z_i) & 2(x_j - x_i) & 2(y_j - y_i) & 2(z_j - z_i) & \cdots \\ \vdots & \vdots & \vdots & \vdots & \vdots & \vdots & \vdots & \vdots \end{pmatrix} \tag{3.8}$$

Considering that the stretching force density (2.48) may be approximated by standard first order finite differences as

$$\mathbf{f}_i^{stretching} = \frac{\partial}{\partial s}\left(\Lambda_i \frac{\partial \mathbf{r}_i}{\partial s}\right) \approx \Lambda_{i+1} \frac{\mathbf{r}_{i+1} - \mathbf{r}_i}{h^2} - \Lambda_i \frac{\mathbf{r}_i - \mathbf{r}_{i-1}}{h^2}, \tag{3.9}$$

it should be apparent from (3.8) that the Jacobian constraint matrix can be used to express the discretized stretching force density as

$$\mathbf{f}_{stretching} \approx -\mathbf{J}^T \frac{\boldsymbol{\Lambda}}{2h^2}. \tag{3.10}$$

If we denote all of the discretized force densities except the stretching force density as $\mathbf{f}_0$ so that the discrete equation of motion in matrix form reads $\mathbf{v} = \boldsymbol{\mu}\left(\mathbf{f}_0 + \mathbf{f}_{stretching}\right)$, (3.7) and (3.10) immediately yield the following discrete equation of motion

$$\mathbf{J}\boldsymbol{\mu}\left(\mathbf{f}_0 - \mathbf{J}^T \frac{\boldsymbol{\Lambda}}{2h^2}\right) = \mathbf{0}. \tag{3.11}$$

Our goal now is to use the Jacobian matrix and the constraint of inextensibility to exclude the internal tension $\boldsymbol{\Lambda}$ from the equation of motion entirely so as to avoid the necessity of explicitly calculating the tension, which would require a new differential equation in addition to the equation of motion. Rearranging (3.11) gives

$$\mathbf{J}\boldsymbol{\mu}\mathbf{f}_0 = \mathbf{J}\boldsymbol{\mu}\mathbf{J}^T \frac{\boldsymbol{\Lambda}}{2h^2}. \tag{3.12}$$

It is now straightforward to express the tension

$$\frac{\boldsymbol{\Lambda}}{2h^2} = \left(\mathbf{J}\boldsymbol{\mu}\mathbf{J}^T\right)^{-1} \mathbf{J}\boldsymbol{\mu}\mathbf{f}_0. \tag{3.13}$$

If we now recall (3.10), we can simply reinsert the tension (3.13) in the discrete equation of motion to obtain an expression that no longer requires us to explicitly calculate the tension itself

$$\mathbf{v} = \boldsymbol{\mu}\left(\mathbf{f}_0 - \boldsymbol{\mu}\mathbf{J}^T\left(\mathbf{J}\boldsymbol{\mu}\mathbf{J}^T\right)^{-1}\mathbf{J}\mathbf{f}_0\right) = \boldsymbol{\mu}\left(\mathbf{I} - \boldsymbol{\mu}\mathbf{J}^T\left(\mathbf{J}\boldsymbol{\mu}\mathbf{J}^T\right)^{-1}\mathbf{J}\right)\mathbf{f}_0. \tag{3.14}$$

The operator $\mathbf{P} = (\mathbf{I} - \boldsymbol{\mu}\mathbf{J}^T\left(\mathbf{J}\boldsymbol{\mu}\mathbf{J}^T\right)^{-1}\mathbf{J})$ satisfies the property $\mathbf{P}^2 = \mathbf{P}$ and may be interpreted as an orthogonal projection operator that essentially projects a filament configuration to a configuration in the space of allowed motions for an appropriately constrained (inextensible) filament. The general approach of using a projection operator to ensure inextensibility is due to Nedelec and Foethke [61], while the adaptation to the case of magnetic filaments was first published in [26].

The discrete equation of motion can be expressed using the newly obtained projection operator as

$$\mathbf{v} = \boldsymbol{\mu}\mathbf{P}\mathbf{f}_0, \tag{3.15}$$

which coupled with the twist diffusion equation (3.2) finally gives the full set of spatially discrete equations that fully characterize the dynamics of an elastic, magnetic filament immersed in a Stokesian fluid, assuming that any applicable boundary conditions are properly accounted for by the differentiation operators described previously. This lets us formulate the following general algorithm to calculate the filament dynamics

1. Define the simulation parameters Cm, L/L_e, p and any relevant parameters for the hydrodynamic approximations.

2. Formulate appropriate initial conditions for the filament position vector $\mathbf{r}_i$ and the twist density Ω_{3i}, if applicable.

3. Calculate all of the differentiation operators $D^{(n)}$ for $n = 1,2,4$.

4. Evolve the filament dynamics, advancing the dimensionless time by a timestep τ:
    (a) compute the Jacobian matrix using (3.6) and (3.5)
    (b) calculate the mobility tensor $\boldsymbol{\mu}$ using the appropriate expressions for the chosen approximation
    (c) compute the projection operator $\mathbf{P} = (\mathbf{I} - \boldsymbol{\mu}\mathbf{J}^T \left(\mathbf{J}\boldsymbol{\mu}\mathbf{J}^T\right)^{-1}\mathbf{J})$
    (d) update any time dependent boundary conditions in the differentiation operators (typically only $D_m^{(1)}$)
    (e) obtain the magnetic force density $\mathbf{f}_{magnetic}$ (see (3.3), (3.4) and the preceding discussion)
    (f) solve the equations of motion using any appropriate numerical method and advance the timestep

5. Repeat step (4) until an arbitrary end time t_{end}.

6. Conduct any desired post-processing of the results, etc.

Two major points in the general numerical algorithm still require further elaboration: the computation of the mobility tensor $\boldsymbol{\mu}$ (4b) and the integration of the equations of motion (4f). In accordance with the methods of approximating hydrodynamic interactions outlined in chapter 2.4, our numerical model currently includes three methods of computing the mobility tensor $\boldsymbol{\mu}$: resistive force theory, the method of reflections up to the Rotne-Prager-Yamakawa level and the method of induced forces as implemented by the software library HYDROLIB [44].

The dimensionless mobility tensor in the resistive force theory approximation (given in dimensional form in (2.104), which only needs to be divided by ζ_n to obtain the dimensionless expression) reads

$$\boldsymbol{\mu}_{RFT}^{-1} = \left(\mathbf{I} + \frac{\zeta_t - \zeta_n}{\zeta_n}\right) D^{(1)}\mathbf{r} \otimes D^{(1)}\mathbf{r}. \tag{3.16}$$

The expression (3.16) introduces a new free dimensionless parameter ζ_n/ζ_t in the numerical model. As derived in chapter 2.4, the limiting value in the case of an infinitely thin filament is ζ_n/ζ_t while ratios in real cases are expected to be in the range $1 \leq \zeta_n/\zeta_t \leq 2$. The effect of different values of the ratio ζ_n/ζ_t on the dynamics of the filament as well as extensive comparisons with more sophisticated hydrodynamic approximations are discussed at length in chapter 4.1.1.

The Rotne-Prager-Yamakawa (RPY) mobility tensor is given in dimensional form in (2.111) and (2.112). Dividing by the classical Stokes friction coefficient for a single sphere $\zeta = 6\pi\eta a$ yields the dimensionless expressions

$$\mu_{ij}^{RPY} = \frac{3}{4}\frac{a}{r_{ij}}\left(\left(1+\frac{2a^2}{3r_{ij}^2}\right)\mathbf{I}+\left(1-\frac{2a^2}{r_{ij}^2}\right)\mathbf{r}_{ij}\otimes\mathbf{r}_{ij}\right),\ r_{ij} > 2a, \tag{3.17}$$

$$\mu_{ij}^{RPY} = \left(1-\frac{9r_{ij}}{32a}\right)\mathbf{I}+\frac{3r_{ij}}{32a}\mathbf{r}_{ij}\otimes\mathbf{r}_{ij},\ r_{ij} \leq 2a, \tag{3.18}$$

where the indices $i, j = 1, 2, ..., p+1$, the scalar parameter $r_{ij} = |\mathbf{r}_j - \mathbf{r}_i|$ and the vectors $\mathbf{r}_{ij}$ are unit vectors, scaled by the scalar norm r_{ij}. As with the resistive force theory approximation, we again have a new dimensionless free parameter in the model, although this time it is considerably more subtle in terms of physical considerations. The expressions (3.17) and (3.18) depend on the radius a of a virtual sphere used to represent an area around an arbitrary marker point on the filament. There is, however, no physical reason in the general case to prefer a particular distance between the spheres. For a linear array of $p+1$ spheres of radius a, situated at a constant distance $\lambda \cdot a$ from each other, the total length reads $L = 2a(p+1) + \lambda ap$. If we recall that the length in all dimensional equations was scaled by the filament length L, the dimensionless sphere radius can be immediately expressed as $a = (2(p+1) + \lambda p)^{-1}$. The intersphere distance λ is thus a free parameter in the Rotne-Prager-Yamakawa approximation of hydrodynamic interactions within the context of our numerical model. Since the expressions (3.17) and (3.18) remain well defined for any values of the relevant parameters, as long as $r_{ij} \neq 0$. There are therefore no additional physical or mathematical considerations to limit the range of values the parameter λ may take unless additional information about the filament structure is provided. On the other hand, this approximation enables us to accommodate a wide range of filament structures should the need arise.

In terms of free parameters, the mobility tensor in the case of the method of induced forces is identical to the Rotne-Prager-Yamakawa approach, as will indeed be the case with all approximations of hydrodynamic interactions that fundamentally deal with arbitrary arrays of spheres. There is, however, a difference in terms of the scales used to cast the relevant quantities in dimensionless form. While the HYDROLIB library produces scale-invariant dimensionless mobility tensors automatically, the length scale is divided by the sphere radius a [44] rather than the filament length L as is done in our model. At each time step we therefore need to re-scale the position vector of the filament marker points $\mathbf{r}_i$ by multiplying it with an appropriate scale factor

$$\mathbf{r}_i^{HYDROLIB} = (2(p+1) + p\lambda)\,\mathbf{r}_i, \tag{3.19}$$

where the parameter λ once again denotes the separation distance between two neighboring spheres in units of sphere radii. The only additional constraint is imposed by the fact that the HYDROLIB library does not handle overlapping spheres, so the intersphere separation distance is strictly required to obey the constraint $\lambda > 0$ while in practice we recommend $\lambda \geq 0.5$ to avoid numerical issues.

Since we have now fully specified the methodology (if not the implementation) of computing all of the quantities required for the dimensionless equations of motion (3.15) and (3.2), it only remains to specify the method of numerical solution of the aforementioned equations.

In order to execute the entirety of the algorithm outlined previously in this chapter, we first created a software package in the well known MATLAB programming environment. The MATLAB language and its associated ecosystem of toolboxes is extremely well suited to the rapid prototyping of numerical applications due to the wide array of in-built numeric calculation and analysis functions as well as the integrated development environment supplied with the software. However, while the performance of matrix/vector operations is usually very good due to the integrated Intel MKL backend library, the efficiency of relatively simple algebraic operations carried out in loops suffers the usual overhead associated with most high level interpreted programming languages. The common solution for performance sensitive applications in the domain of scientific computing is to write code in (comparatively lower level) compiled programming languages such as C++ or Fortran. This in turn bears a considerable cost in terms of additional development time and diminished flexibility of the codebase due to both the increased complexity of the codebase and the lack of dynamic integrated development environments comparable to that of MATLAB.

In our case, as long as hydrodynamic interactions are neglected or computed in the resistive force theory approximation, the computational cost of the algorithm is dominated by matrix multiplication and factorization operations and the MATLAB implementation is therefore close to optimal. This changes radically if we decide to simulate the effect of hydrodynamic interactions in the Rotne-Prager-Yamakawa tensor approximation. With sufficiently large systems of equations ($p > 50$) the computation time is dominated by the calculation of the mobility tensor. Since we also aim to simulate the dynamics of multiple hydrodynamically coupled filaments (described in more detail in the next chapter) an alternative implementation becomes highly desirable to ensure scalability. For this purpose we employ the *Julia* programming language [9][8], a newly developed high-level dynamic programming language developed at the Massachusetts Institute of Technology (MIT) with a considerable emphasis on efficient scientific computing while retaining the general ease of use associated with languages such as MATLAB and Python. In addition to having a fairly rich standard library for the purposes of numeric computation, its syntax also bears considerable similarities to the MATLAB language, letting us port MATLAB code to Julia with minimal effort. In doing so we have obtained a performance advantage of roughly two orders of magnitude in limiting cases where the computation time is dominated by the calculation of the Rotne-Prager-Yamakawa tensor, enabling us to conduct simulations that would have normally taken days in less than an hour. This immense performance differential in certain cases is largely explained to a first approximation by Julia's implementation of an efficient just-in-time (JIT) compiler which automatically generates a highly optimized statically typed machine code representation of any function written in the high level language itself, as long as it satisfies certain restrictions.

In both languages we implement two different approaches to integrating the equations of motion (3.15) and (3.2) with different computational advantages. First, we discretize both equations using the method of lines (MOL), replacing the spatial derivatives with finite difference analogues and obtaining a large system of ordinary differential equations. While a basic explicit first order Euler scheme that would transform the system of ODEs into a set of algebraic expressions is trivial to implement, there are considerable advantages to employing a variable order multistep solver intended for numerically stiff problems (which quickly becomes the case as the frequency of the external magnetic field is increased due to the disparity between the time scales of the physical phenomena involved). For this reason we employ the *ode15s* function in the MATLAB programming environment. A comparable capability is provided by the well known and extensively tested *Sundials* [43] library available from the Lawrence Livermore National Laboratory. An easy to use interface to this library is available under the name *Sundials.jl* through the integrated package manager of the Julia programming environment.

However, in addition to the MOL approach we also implement an implicit backward Euler scheme [1] for the many cases where the twist may be neglected. This lets us use much larger timesteps than any explicit scheme and is a single-step scheme (whereas the different multistep methods require multiple evaluations of the right hand side terms, which is quite expensive computationally), thereby vastly decreasing the amount of mobility tensors we need to compute over any fixed interval of time. The backward Euler scheme also has the advantage of unconditional numerical stability. Unfortunately, due to the velocity-dependent term in the twist diffusion equation (3.2) there is no way to formulate a fully implicit computational scheme that would include the effects of twist without incurring significant computational overhead.

In order to obtain the implicit backward Euler (IBE) formulation of our equations, we discretize the time dependence in (3.15) as follows

$$\frac{\mathbf{r}^{(t+\tau)} - \mathbf{r}^{(t)}}{\tau} = \boldsymbol{\mu}\mathbf{P}\left(D_b^{(4)}\mathbf{r}^{(t+\tau)} + \mathbf{f}_{magnetic}^{(t)}\right), \tag{3.20}$$

where the superscripts t and $t+\tau$ denote denote the dimensionless time. Multiplying both sides by τ and adding and subtracting $D_b^{(4)}\mathbf{r}^{(t)}$ in the bracketed right hand side term we get

$$\mathbf{r}^{(t+\tau)} - \mathbf{r}^{(t)} = \tau\boldsymbol{\mu}\mathbf{P}\left(D_b^{(4)}\mathbf{r}^{(t+\tau)} - D_b^{(4)}\mathbf{r}^{(t)} + D_b^{(4)}\mathbf{r}^{(t)} + \mathbf{f}_{magnetic}^{(t)}\right), \tag{3.21}$$

which may be immediately rearranged to yield

$$\left(\mathbf{I} - \tau\boldsymbol{\mu}\mathbf{P}D_b^{(4)}\right) \cdot \left(\mathbf{r}^{(t+\tau)} - \mathbf{r}^{(t)}\right) = \tau\boldsymbol{\mu}\mathbf{P}\left(D_b^{(4)}\mathbf{r}^{(t)} + \mathbf{f}_{magnetic}^{(t)}\right), \tag{3.22}$$

which represents a set of linear algebraic equations formally solved by inverting the matrix $\left(\mathbf{I} - \tau\boldsymbol{\mu}\mathbf{P}D_b^{(4)}\right)$ (in practice, methods utilizing LU decompositions are much more efficient). The *mldivide* function in the MATLAB programming environment is used to solve equation (3.22) once all the necessary quantities have been computed, this allows for automatic selection of the appropriate method of matrix decomposition based on the symmetry properties of the coefficient matrix $\left(\mathbf{I} - \tau\boldsymbol{\mu}\mathbf{P}D_b^{(4)}\right)$ at runtime. The backslash operator from the Julia standard library provides equivalent functionality and is used in the Julia implementation of the IBE scheme. In practice, we find that using the IBE scheme when the effects of twist are neglected often (but not always) leads to much smaller computation times at comparable accuracy, as shown in chapter 3.3. It is also worth noting that the codebase of the numerical model is deliberately structured very modularly, so that new hydrodynamic approximations, boundary conditions, force density terms and entire solution schemes can be implemented with minimal effort, reusing the existing code as much as possible. Great care is also taken to dynamically analyze the the input parameters and determine what calculations are required in each particular case. Because of this, the implementation of more advanced approximations, the effects of twist, etc. introduces virtually no overhead in terms of computational efficiency whenever they are not directly employed.

3.2 Multiple filaments

In the previous chapter we established a complete numerical model for simulating the dynamics of a magnetoelastic filament immersed in a Stokesian fluid under the action of an external magnetic field utilizing different levels of approximation for the hydrodynamic interactions. In this chapter we will demonstrate that the aforementioned approach is in fact sufficiently flexible as to be straightforwardly generalized to the case of arbitrarily many hydrodynamically coupled filaments with minimal modifications.

Since we stated at the very beginning of our theoretical model in Chapter 2 that we disregard the effect of the magnetic filament on the surrounding field, it follows that in the case of several filaments they will not be magnetically coupled in any way. Thus, the only coupling we need to consider is through momentum transfer via hydrodynamic interactions. This is something resistive force theory clearly cannot accommodate without further modifications in the form of approximate interaction factors. We shall therefore only consider the Rotne-Prager-Yamakawa tensor approximation and the method of induced (as used in the HYDROLIB library) in this chapter. Both approaches yield mobility tensors for arbitrary configurations of identical spheres, so no modifications to the parts of the numerical model responsible for computing the mobility tensor are necessary, we simply compute the total mobility tensor for $N \cdot (p+1)$ marker points for N filaments.

In order to solve the equations of motion for an arbitrary amount of filaments, we simply compute the individual projection operators, force densities and terms of the twist diffusion equation for each filament separately (this may be done in parallel) and arrange them in the ensemble equations of motion

$$\mathbf{v} = \boldsymbol{\mu}\mathbf{P}\mathbf{f}_0, \tag{3.23}$$

$$\frac{\partial \Omega_3}{\partial t} = d_0 D^{(2)}_{tw} \Omega_3 + \left(D^{(1)}\mathbf{r} \times D^{(2)}\mathbf{r} \right) \cdot D^{(1)}\mathbf{v}, \tag{3.24}$$

where $\mathbf{v} = (\mathbf{v}_{1,1}, \mathbf{v}_{1,2}, \ldots, \mathbf{v}_{1,p+1}, \mathbf{v}_{2,1}, \ldots, \mathbf{v}_{N,(p+1)})$ so that the velocity vector with the indices i, j denotes the velocity of the j-th marker point of the i-th filament and similarly for vectors $\mathbf{f}_0$ and $\mathbf{r}$. Analogously, the ensemble twist density reads $\Omega_3 = \Omega_{3,ij}$ for $i = 1, 2, \ldots, N$ and $j = 1, 2, \ldots, p+1$. The total mobility tensor is denoted by $\boldsymbol{\mu}$ and computed according to (3.17) and (3.18) (using the ensemble position vector $\mathbf{r}$) if the Rotne-Prager-Yamakawa tensor approximation is used or using the HYDROLIB library. Finally, the total projection operator $\mathbf{P}$ can be expressed in diagonal block matrix form as

$$\mathbf{P} = \begin{pmatrix} \mathbf{P}_1 & \mathbf{0} & \mathbf{0} & \cdots & \mathbf{0} \\ \mathbf{0} & \mathbf{P}_2 & \mathbf{0} & \cdots & \mathbf{0} \\ \mathbf{0} & \mathbf{0} & \mathbf{P}_3 & \cdots & \mathbf{0} \\ \vdots & \vdots & \vdots & \ddots & \vdots \\ \mathbf{0} & \mathbf{0} & \mathbf{0} & \cdots & \mathbf{P}_N \end{pmatrix}, \tag{3.25}$$

where the $3(p+1) \times 3(p+1)$ matrices $\mathbf{P}_i$ denote the individual filament projection operators for $i = 1, 2, \ldots, N$.

While the formalism employed here is very straightforward, we have in fact implicitly made one additional approximation in our approach. Namely, in order to compute the single filament projection operators $\mathbf{P}_i$ we must employ mobility tensors of size $3(p+1) \times 3(p+1)$ as per our definition of the projection operator $\mathbf{P} = \left(\mathbf{I} - \boldsymbol{\mu}\mathbf{J}^T \left(\mathbf{J}\boldsymbol{\mu}\mathbf{J}^T\right)^{-1} \mathbf{J}\right)$. In using what is in effect a single filament mobility tensor for this part of the calculation we essentially neglect a part of the long range hydrodynamic coupling in order to retain the overall simplicity of the formalism defined here. While we expect the error introduced thereby to be very small (especially for filaments that are comparatively far apart), this is one potential point where improvements may be sought in future work.

Naturally, while the capability to describe ensembles of arbitrarily many filaments has been developed, in practice the number of filaments is severely constrained by available computational resources due to the scaling of the computational cost of calculating large mobility tensors with increasing numbers of marker points. This issue is explored further in the next section.

3.3 Numerical accuracy and computational performance

The purpose of this section is to briefly sketch the basic computational properties of the numerical model empirically and establish the practical limitations in terms of the parameter sets we are reasonably able to use on current computer hardware.

First of all, we need not worry about numerical stability in the strict sense of the term, since in the IBE scheme numerical stability is guaranteed by the basic properties of the backward Euler method itself, whereas in the MOL approach we only employ solvers that feature automatic stability control (and employ variable size timesteps). Nevertheless, choosing overly large timesteps in the IBE scheme risks not fully resolving the dynamics of the system, thereby obtaining numerically correct but physically inaccurate results. In the

τ	$\Delta_{\omega=4096}$	$\Delta_{\omega=20736}$	time, s
$5\cdot10^{-5}$	1.1616	0.9943	28
$2\cdot10^{-5}$	0.6765	0.9621	69
$1\cdot10^{-5}$	0.2564	0.3104	140
$5\cdot10^{-6}$	0.2059	0.1320	282
$2\cdot10^{-6}$	0.1476	0.0263	642
$1\cdot10^{-6}$	0.1235	0.0084	1326

Table 3.1 Relative errors with different dimensionless timesteps τ in the IBE scheme.

parameter ranges that are of physical interest this is primarily controlled by the choice of the dimensionless frequency (or, equivalently, the ratio L/L_e), which ultimately drives the filament.

We therefore first look at the relative errors introduced by the use of different timesteps in the IBE scheme by comparing the resulting total displacement of the center of mass coordinate in the direction of motion for a ferromagnetic microswimmer with free ends located entirely in the $x-y$ plane (see Section 4.1.1 for a detailed description of the physical properties of this configuration) to the same quantity obtained through the use of the MOL scheme with variable timesteps, the latter being considered exact for the purposes of this comparison. Since we are only evaluating the effect of different timesteps here, hydrodynamic interactions were approximated at merely the resistive force theory level (with the classical value $\zeta_n/\zeta_t = 2$), the number of marker points was $p = 200$ for the IBE scheme and $p = 50$ for the MOL scheme, the magnetoelastic number was $Cm = 400$. All calculations were run until $t_{end} = 0.025$, at which point the total displacement of the center of mass y coordinate was recorded, the results are shown in Table 3.1. The end time was chosen so that the stable periodic regime of the filament's motion would have already been established for several periods at both frequencies, after which point any errors would grow linearly. Nevertheless, we must note that for most of the physical situations modelled in Chapter 4 of this work much larger values of t_{end} are required, so all the computation times given in this section are smaller than those typically seen for a single simulation, often by an order of magnitude. For purposes of consistency in comparing computation times all calculations presented in this chapter were done on the same Intel i7 920-D0 processor running at a constant frequency of 3.8 Ghz. The numerical model fully exploits all available cores for all linear algebra operations of sufficient size and the HYDROLIB library was compiled a modern OpenBLAS linear algebra backend [77] to achieve the same end.

The two frequencies used are chosen to roughly correspond to the opposite ends of the frequency range where propulsion occurs for this particular physical configurations,

p	$\Delta_{\omega=4096}$	$\Delta_{\omega=20736}$	time, s
25	0.1014	0.1502	8
50	0.1270	0.0719	22
75	0.1229	0.0436	57
100	0.1149	0.0292	109
150	0.0997	0.0146	317
200	0.0880	0.0073	635
300	0.0000	0.0000	1860

Table 3.2 Relative errors with different numbers of marker points $p+1$ in the IBE scheme, $\tau = 2 \cdot 10^{-6}$.

otherwise the errors would have little meaning. For the sake of comparison, the computation times for the MOL scheme were $t = 765s$ in the case of the lower frequency and $t = 1556s$ for the higher frequency. The computation times in the IBE scheme naturally do not depend on the choice of frequency, since the timestep is constant. From Table 3.1 we can see that timesteps $\tau \leq 2 \cdot 10^{-6}$ can offer reasonable accuracy and do make the IBE scheme worth using as the computation time is smaller by a factor of 2.5 compared to the MOL scheme. Nevertheless, the errors introduced can also grow to unacceptably large values for particular values of the dimensionless frequency so an initial investigation using the MOL scheme as a point of comparison is always required. It was also observed during calculations with the MOL scheme that while the mean timestep tended to be approximately 10^{-6}, the smallest timesteps occasionally used were on the order of 10^{-8}, whereas the largest could go as high as $3 \cdot 10^{-5}$, a difference of over three orders of magnitude. These results serve to remind us that when dealing with phenomena involving vastly different time scales numerical stability and seemingly reasonable outputs (even for the largest timesteps used here the filament still behaved qualitatively similarly, no obviously unphysical behavior was observed) are no guarantee of accuracy. In the absence of directly comparable analytic or experimental data one must be especially careful about ensuring that the choice of numerical parameters has minimal effect on the accuracy of the results.

We also need to evaluate the impact of the number of marker points chosen to represent a given filament. We do this separately for both numerical schemes because the MOL scheme typically requires far fewer points to attain comparable accuracy. We take the same two frequencies as well as the parameters t_{end}, Cm as in Table 3.1 and calculate the relative errors of the center of mass with respect to the most accurate computation done. The results are shown in Tables 3.2 and 3.3.

p	$\Delta_{\omega=4096}$	$\Delta_{\omega=20736}$	$time_{\omega=4096}$, s	$time_{\omega=20736}$, s
10	1.0963	0.3276	4	7
20	1.0097	0.1092	30	47
30	0.0328	0.0635	109	246
40	0.0244	0.0399	307	643
50	0.0154	0.0258	894	1633
75	0.0000	0.0000	5014	11372

Table 3.3 Relative errors with different numbers of marker points $p+1$ in the MOL scheme.

As we can see, the amount of marker points necessary to attain reasonable accuracy differs by a factor of 4 between the MOL and the IBE scheme. The general pattern of convergence is more reliable in the MOL scheme due to the automatic timestep control. However, the computation time scales cubically in the MOL scheme and only quadratically in the IBE scheme, making the latter quite useful for large values of $p+1$, an especially important property for simulations involving several filaments. The general recommendation is the same as before: for every substantially different frequency of the external field a control calculation using the MOL scheme is advisable before making any claims about the accuracy of results obtained through the use of the IBE scheme. Nevertheless, using the implicit backward Euler (IBE) scheme is justified for computational efficiency when large numbers of marker points or large numbers of simulations for fairly similar frequencies are required.

Finally, to fully appreciate the computational requirements of our numerical model we need to look at the impact of the choice of approximation for hydrodynamic interactions. It is trivial to observe that any cost associated with computing hydrodynamic interactions will grow linearly with the amount of timesteps we have to resolve, however the dependence on the number of marker points $p+1$ is of crucial importance, especially when considering ensembles of filaments. We therefore take the IBE scheme with $\omega = 4096$, $Cm = 400$, $t_{end} = 0.01$, $\tau = 10^{-5}$ and evaluate the total computation times for the resistive force theory approximation, the Rotne-Prager-Yamakawa approximation (in both MATLAB and Julia implementations) and the method of induced forces approximation (utilizing the library HYDROLIB) for several different values of $p+1$. The results of this comparison are given in Table 3.4.

Several major conclusions can be drawn from the data presented in Table 3.4. First, the use of the HYDROLIB library is extremely expensive computationally, slowing down the calculation by more than three orders of magnitude. Furthermore, the computation time for HYDROLIB actually grows faster than for the other methods as the number of marker points is increased. This renders it effectively unusable for practical computations, except to explore

p	t_{RFT}, s	t_{RPY} in MATLAB, s	t_{RPY} in Julia, s	$t_{HYDROLIB}$, s
40	1	50	2	2406
50	2	76	3	3903
60	3	109	4	5852
80	5	193	6	11628
100	8	299	10	21738

Table 3.4 Computation time for different approximations of the mobility tensor.

the accuracy of the other methods in simplified benchmarking scenarios. To illustrate, a typical single computation to explore the dynamics of a magnetic filament for a fixed set of the main simulation parameters (p, Cm, ω, d_0, t_{end}, τ) usually runs up to at least $t_{end} = 0.1$, requires at least $p = 100$ in the implicit backward Euler (IBE) scheme (usually $p = 200$ or $p = 300$) and $\tau = 2 \cdot 10^{(-6)}$, a calculation using HYDROLIB even for a single filament would take approximately 300 hours on the workstation level hardware used in this work. Since explorations of the full parameter space usually require hundreds or thousands of such calculations, the impracticality of relying on the HYDROLIB library for practical research is evident.

On the other hand, while the MATLAB implementation of the Rotne-Prager-Yamakawa tensor also demands significant computational resources (although it is still faster than HYDROLIB by a factor of roughly 50 on average), the Julia implementation is a vast improvement. In particular, the Julia version of the RPY approximation at commonly used values of p is on average slower only by about 20% compared to the resistive force theory. This makes it perfectly feasible to employ the Rotne-Prager-Yamakawa approximation in routine simulations and justifies the time invested in developing a second implementation of the numerical model in the Julia language.

We have now established the basic computational properties of the model developed in previous sections, demonstrated the impact of various parameters on solution accuracy as well as the computational cost of choosing different approximations for hydrodynamic interactions. Due to the lack of directly and quantitatively comparable experimental results or analytic solutions for most of the filament configurations considered in this work, the properties we have shown in this section are crucially important to obtaining accurate results relevant to the appropriate physical situations being investigated. A selection of such results is presented in the next chapter.

Chapter 4

Numerical results and analysis

The purpose of this chapter is to present a reasonably representative selection of the main results obtained from the numerical model developed in Chapter 3 with a particular emphasis on the impact of various approximations to hydrodynamic interactions. While the basic dynamics of most of the filament configurations described in the various sections of this chapter have been explored in previous works using simpler models in the resistive force theory approximation or neglecting hydrodynamic interactions altogether, we analyze the impact of more sophisticated approximations as well as use the computational efficiency of our model to obtain a more general picture of the properties of magnetic filaments in a comprehensive parameter space. Due to the emphasis on hydrodynamic interactions in this work we focus primarily on filaments with free ends, which are known to exhibit periodic swimming behavior in periodically oscillating external magnetic fields. Nevertheless, to showcase the flexibility of our numerical model we also provide an example of a filament configuration with a fixed end - an artificial cilia - and calculate the induced fluid velocities in its vicinity in a wide range of parameters.

The chapter is divided in four major sections, each dedicated to a separate class of magnetic filaments that exhibit considerably varied dynamics when subjected to different configurations of external magnetic fields. We first discuss ferromagnetic filaments with free ends, previously [5] shown to be viable microswimmers. Some basic properties are examined and the available scientific literature used to verify the results of our model. Then we move on to discuss new results obtained using more precise hydrodynamic approximations than previously employed for the analysis of ferromagnetic filaments and quantify the role of twist. The second section of the chapter details artificial cilia producing by constraining one end of a ferromagnetic filament. After establishing the basic properties of such a system we use the capabilities of our model to obtain the flow fields surrounding the rotating ferromagnetic cilia. The third section concerns superparamagnetic filaments with free ends. This presents a further opportunity to verify the results of our model, as the basic dynamics of superparamagnetic filaments in constant fields are well described in the literature. We further present a number of new results demonstrating the existence of a directed propulsive regime in a particular range of the governing parameters when a specific rotating magnetic field is applied. In the fourth section we describe the behaviour of a system that consists of a magnetic dipole and a non-magnetic, elastic tail attached to the dipole. Regions of stable propulsion as well as the impact of various approximations to the hydrodynamic interactions are described. Finally, we consider the dynamics of multiple ferromagnetic filaments in the fifth section of this chapter, demonstrating the existence of a hydrodynamic coupling in systems of two and three filaments.

4.1 Ferromagnetic filaments with free ends

4.1.1 Ferromagnetic microswimmers without twist

Ferromagnetic filaments with free ends under the influence of an external magnetic field are known to undergo two possible modes of deformation: S-like and U-like shapes, depending on the strength of the applied field and the elastic properties on the filament. This has been shown both experimentally and from a theoretical stability analysis back in 2009 by Ērglis *et al* [25]. It was further shown the same year by Belovs and Cēbers [5] that ferromagnetic filaments with free ends could serve as microswimmers in linearly oscillating external magnetic fields by means of a two dimensional numerical model utilizing the tangent angle formalism mentioned in the introductory chapters of this work.

In a constant magnetic field, assuming that the parameters governing the simulation are chosen such that the U-like deformation mode is preferred, the filament forms a loop if the magnetic field is strong enough. Let us begin by examining this behaviour in a two dimensional configuration using the following initial conditions for the shape of the filament

$$x_i = 1 - (0.01\pi/2)^2 ih, \tag{4.1}$$

$$y_i = 0.01\sin(\frac{\pi x_i}{1-(0.01\pi/2)^2}), \tag{4.2}$$

$$z_i = 0, \tag{4.3}$$

and the initial filament position vector is $\mathbf{r}_i = (x_i, y_i, z_i)$ for each value of the index $i = 1, 2, \ldots, p+1$ and $h = \frac{1}{p+1}$. The filament is therefore initially almost straight, only slightly curved in the y direction to provide the initial perturbation that will lead to the development of the U-like deformation mode. A constant magnetic field is applied in the x direction with its strength determined by the magnetoelastic number Cm. Each numerical calculation is then run until a final stable configuration is attained. The stopping criterion is that the maximal curvature of the filament has changed by less than 0.1% during the last 100 timesteps taken by the solver. A representative selection of such configurations at different values of the magnetoelastic number is shown in Figures 4.1, 4.2 and 4.3. Since it has been shown in a previous stability analysis that the magnetoelastic number has a critical value π^2 (established as $\pi^2/4$ in [5], however, due to different scale factors the magnetoelastic number used in this work is larger than that in the reference by a factor of 4) below which the filament does not deform, we do not show configurations with $Cm < 10$. From the aforementioned figures it can be seen that at relatively low values of the magnetoelastic number the filament does not bend strongly enough to form loops. This point may be made quantitatively precise utilizing the concept of the writhe introduced in Chapter 2. The writhe of the ferromagnetic filament configurations as a function of the magnetoelastic number is shown in Fig. 4.4. This gives a useful quantitative measure of the loop formation at different magnetoelastic numbers.

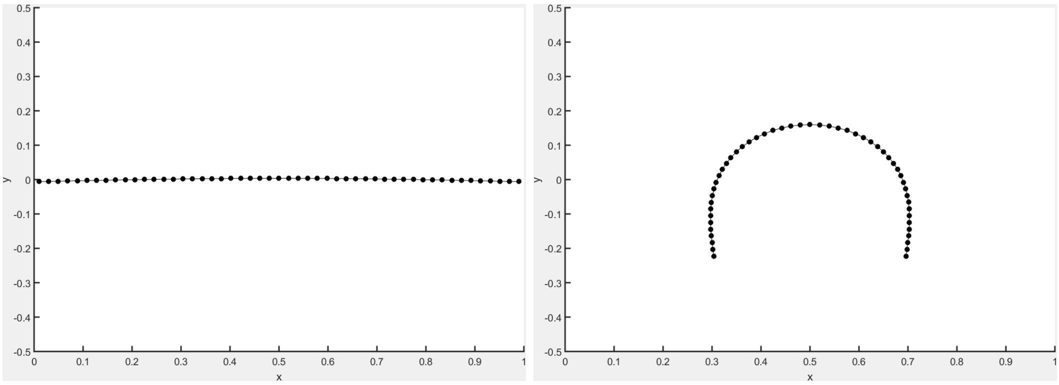

Fig. 4.1 Stable 2D configurations of the ferromagnetic filament in a constant field with $Cm = 10$ (left), $Cm = 15$ (right).

The curvature of the stable two dimensional configurations can be estimated theoretically by solving the following equation in the tangent angle formulation ($\mathbf{t} = (\cos(\theta), \sin(\theta))$)

$$\frac{d^2\theta}{ds^2} + Cm\sin(\theta) = 0, \tag{4.4}$$

which in the case of free ends ($d\theta/ds|_{s=\pm L} = 0$) yields

$$\theta = -2\arcsin(\sin(\theta_m/2)sn\left(\sqrt{Cm}s, \sin^2(\theta_m/2)\right)), \tag{4.5}$$

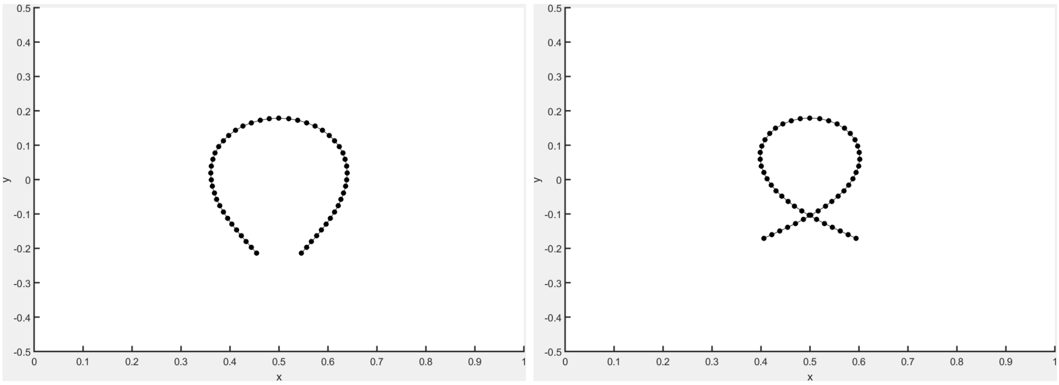

Fig. 4.2 Stable 2D configurations of the ferromagnetic filament in a constant field with $Cm = 20$ (left), $Cm = 30$ (right).

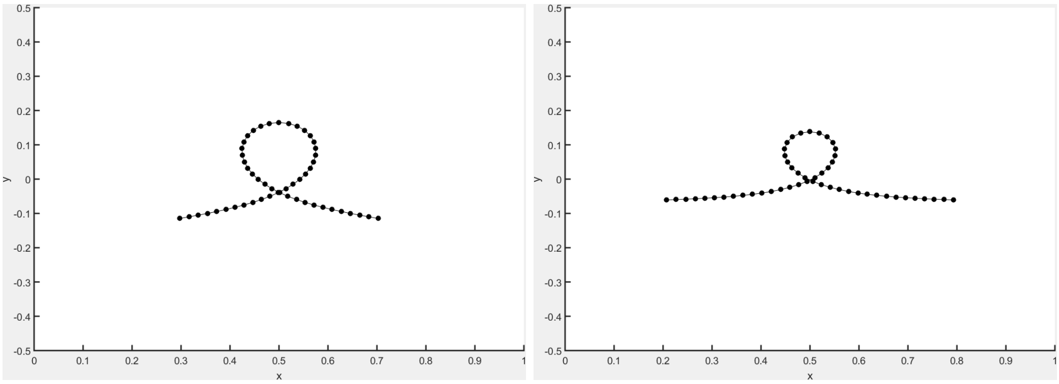

Fig. 4.3 Stable 2D configurations of the ferromagnetic filament in a constant field with $Cm = 50$ (left), $Cm = 100$ (right).

where θ_m denotes the tangent angle at the ends of the filament while the function $sn(x,k^2)$ is the Jacobi elliptic function. It may be shown [26] that asymptotically, for $Cm \geq 10$, the relation $\kappa_{max} = 2\sqrt{Cm}$ describes the maximal curvature quite well. A comparison with the results of our numerical simulations is given in Fig. 4.5. Clearly the results agree very well for magnetoelastic numbers up to about $Cm = 100$, whereupon the numerical maximal curvature continues to increase faster than the theoretical estimate.

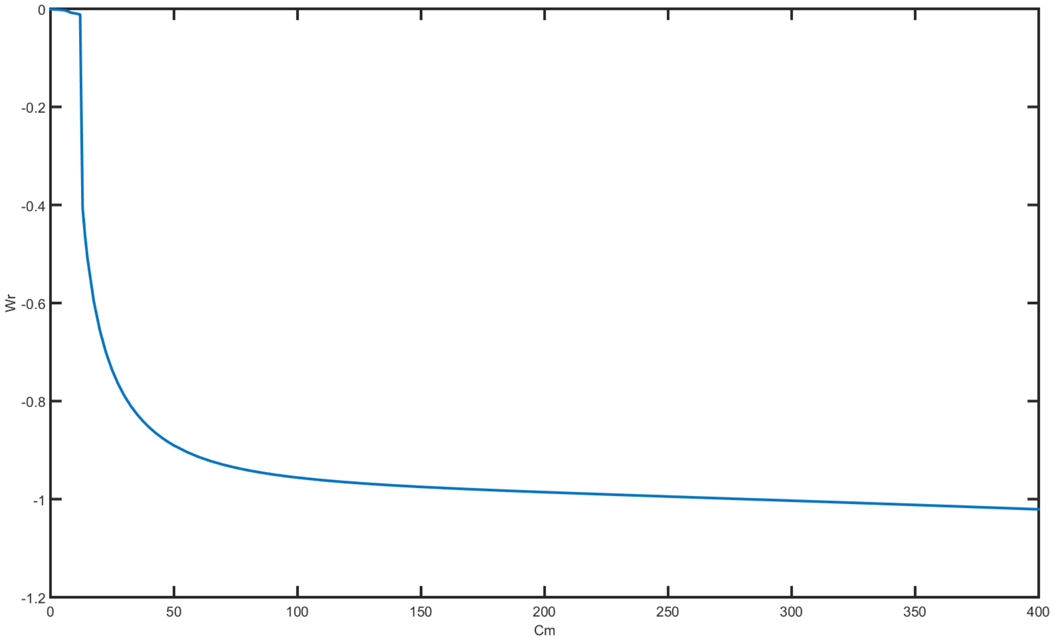

Fig. 4.4 The writhe as a function of the magnetoelastic number.

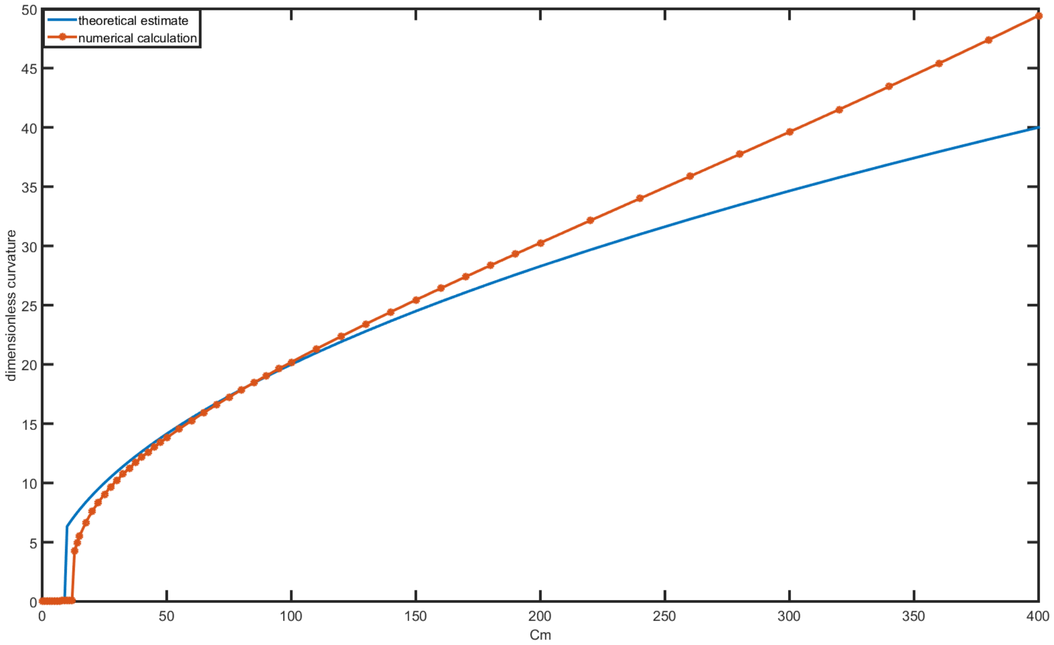

Fig. 4.5 The maximal curvature as a function of the magnetoelastic number: comparing numerical data with the theoretical estimate.

In a previous publication [26] we have shown that the configurations produced by the ferromagnetic filament in a constant field are no longer stable when even very small perturbations from the purely two dimensional state are applied. This result was also verified experimentally and is fully reproduced by the computational model described in this work. We therefore begin our examination of the filament dynamics in a time varying magnetic field by examining an initially two dimensional configuration as defined in equations (4.1) - (4.3).

The magnetic field is linearly oscillating in the x direction so that $\mathbf{H} = Cm(\cos \omega t, 0, 0)$. Since the motion is entirely two dimensional, the effects of twist may be neglected entirely. Our aim here is to determine what values of the magnetoelastic number and the dimensionless frequency of the external magnetic field lead to the largest swimming velocities and what effect the level of approximation for the hydrodynamic interactions has on the filament dynamics.

In order to obtain a comprehensive overview of the swimming velocities as a function of the magnetoelastic number Cm and the dimensionless frequency ω we conduct a series of 2520 simulations in total, which represent over a month of computation time. We look at magnetoelastic numbers in the range $25 \leq Cm \leq 500$ and the ratio $L/L_e = \omega^{1/4}$ in the range $2 \ldots 18$, each time conducting a simulation until a fixed dimensionless end time $t_{end} = 0.1$ and noting the total displacement of the y component (which is in the direction of motion) of the center of mass position relative to the initial state. We conduct all of these simulations both in the resistive force theory approximation (for three different values of the ratio ζ_n/ζ_t: the classical asymptotic value 2 as well as the values 1.75 and 1.5) and in the Rotne-Prager-Yamakawa approximation (for three different values of the inter-sphere distance parameter $\lambda = 0.5, 2, 4$ in units of sphere radii). All calculations are conducted using the method of lines (MOL) scheme (for reasons outlined in Chapter 3), with $p = 100$. The results are shown in Figures 4.6 - 4.11, with the total displacement shown using the color scale displayed on the right side of each figure.

Several conclusions can be drawn immediately. First of all, the classical value $\zeta_n/\zeta_t = 2$ for the resistive force theory approximation to hydrodynamic interactions clearly results in a fairly significant (roughly 20% on average) overestimation of the filament velocity. The value $\zeta_n/\zeta_t = 1.75$ seems quite appropriate for closely located spheres (as can be seen by directly comparing Figure 4.7 with Figures 4.9 and 4.10) while smaller values may still be useful depending on the filament structure. Secondly, the Rotne-Prager-Yamakawa approximation does constrain the region in $Cm - \omega$ space where directed motion takes place more so than resistive force theory, irrespective of the particular value of the anisotropic friction ratio (see, for instance, the contrast between Fig. 4.7 and Fig. 4.9). There is a range

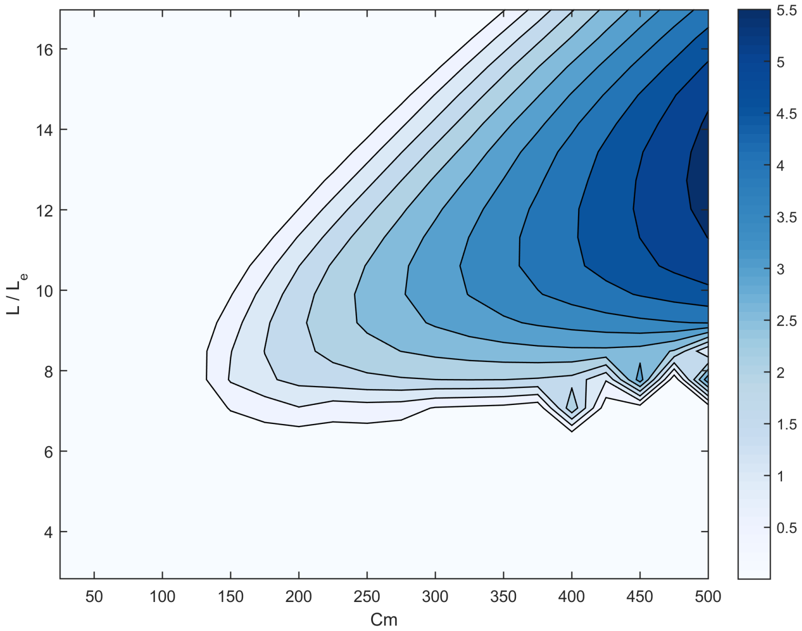

Fig. 4.6 The total displacement in the y direction y_c at dimensionless time $t = 0.1$ using resistive force theory. $\zeta_n/\zeta_t = 1.5$.

of frequencies (roughly between $L/L_e \approx 8$ and $L/L_e \approx 10$, though a slight dependence on the magnetoelastic number also exists) at which directed motion occurs in the resistive force theory approximation, but not in the more accurate Rotne-Prager-Yamakawa approach. This is a qualitative difference between both approximations for our use case that could not be found without the comprehensive computational effort undertaken to explore the filament motion throughout the parameter space $Cm - \omega$. We also note that despite the stringent attention to the choice of numerical parameters described in Chapter 3.3 the border regions in Figures 4.6 - 4.11 where periodic motion only just begins to occur still show signs of numerical effects. A more detailed investigation of filament dynamics in precisely these regions may help further elucidate the effects of different hydrodynamic approximations in the future.

In the absence of directly relevant experimental data that could confirm our results quantitatively in this particular case, questions must still be asked regarding the accuracy of the Rotne-Prager-Yamakawa approximation we have employed. Reproducing the numerical results shown here using the more accurate HYDROLIB library to calculate hydrodynamic interactions in the method of induced forces approximation would require many years of computation time and is not practically feasible at the present time. Nevertheless, we may take a particular representative pair of values for the magnetoelastic number and the

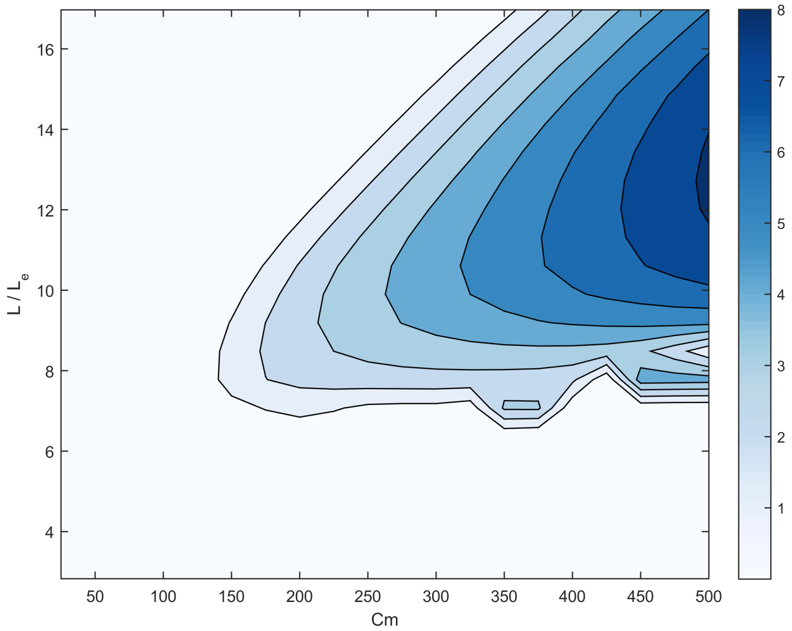

Fig. 4.7 The total displacement in the y direction y_c at dimensionless time $t = 0.1$ using resistive force theory. $\zeta_n/\zeta_t = 1.75$.

dimensionless field frequency and explore the role of hydrodynamic interactions in more detail. Figures 4.12 and 4.13 show the time evolution of the y coordinate of the center of mass of the filament in all three methods of calculating hydrodynamic interactions we have thus far implemented in our numerical model: the resistive force theory approximation, the RPY tensor and the HYDROLIB library.

For the parameters chosen here it seems that the benchmark HYDROLIB calculation closely mirrors the Rotne-Prager-Yamakawa results as long as the sphere separation distance $\lambda = 0.5$, with differences of a few percent at most as measured in the total displacement of the filament's center of mass in the direction of motion. The difference between the two methods grows substantially as the separation distance λ is increased. With respect to the resistive force theory approximation, the *de facto* standard approximation in the literature, it seems to hold up to the Rotne-Prager-Yamakawa approximation rather well as long as appropriate values of the anisotropic friction coefficient ratio ζ_n/ζ_t are chosen. However, as we saw in the discussion of the results shown in Figures 4.6 - 4.11, the seemingly close correspondence may be somewhat deceptive as the RPY approximation introduces qualitative changes in specific regions of the parameter space $Cm - \omega$.

Let us now look at the regions of $Cm - \omega$ space where we have the major differences between the resistive force theory (RFT) and Rotne-Prager-Yamakawa (RPY) approximations.

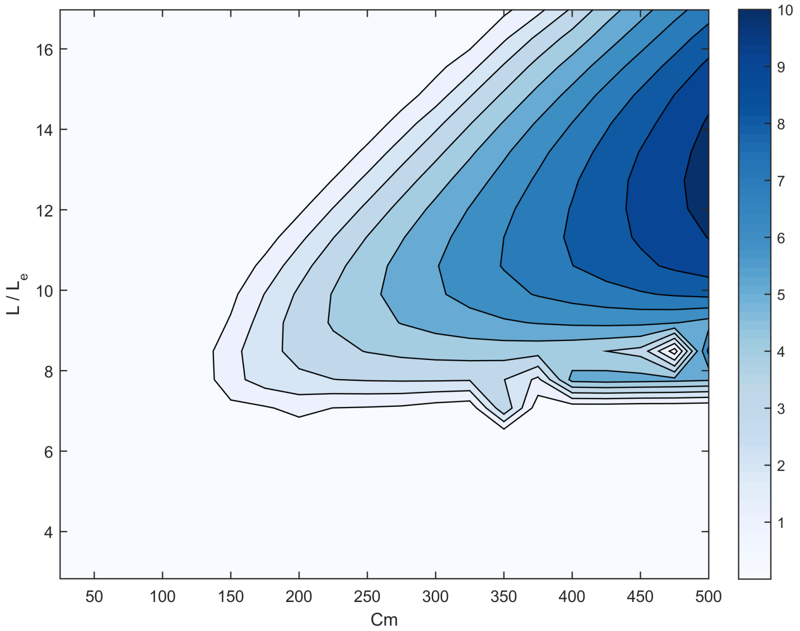

Fig. 4.8 The total displacement in the y direction y_c at dimensionless time $t = 0.1$ using resistive force theory. $\zeta_n/\zeta_t = 2$.

If we take $Cm = 288$ and $\omega = 4800$ ($L/L_e = 8.32$) and look at the dependence of the center of mass y coordinate on time, as depicted in Fig. 4.14, the reason for the discrepancy becomes clear immediately: the U-shape of the filament, which was perpetually stable in the resistive force theory approximation as long as the initial configuration was located entirely in the $x-y$ plane, is only metastable in the RPY approximation. This is a fundamental departure from the results we have reported previously [27] and has not been described before. To show the progression of this phenomenon in more detail we have plotted a series of 12 projected snapshots of the filament configurations in the $x-y$ and $y-z$ planes in Figures 4.15 - 4.27. It is interesting to note that fairly substantial quantitative differences in the filament shape appear immediately even during the regime of stable planar motion, as seen in Figures 4.15 - 4.19. Looking at a later period of motion starting with Figure 4.20 we see that the filament calculated in the RPY approximation begins to deform in a fundamentally three dimensional way despite the initial configuration being entirely planar. This ultimately leads (see Figures 4.22 and 4.23 in particular) to the filament loop relaxing through the third dimension exactly as we had previously found in the case where the initial configuration was slightly perturbed out of the $x-y$ plane (published in [26]). This explains how the change from the resistive force theory (RFT) approximation which merely assigns anisotropic friction coefficients to the full Rotne-Prager-Yamakawa (RPY) mobility tensor which can potentially (and, in

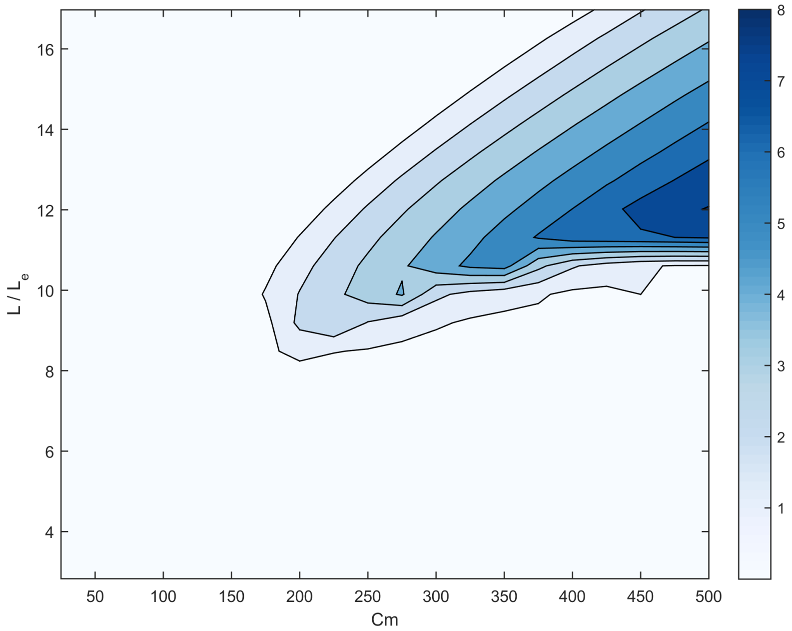

Fig. 4.9 The total displacement in the y direction y_c at dimensionless time $t = 0.1$ using the Rotne-Prager-Yamakawa tensor at $\lambda = 0.5$.

this case, actually does) qualitatively affect the entire shape of the filament leads to this new instability. It therefore appears that even strictly constraining the initial state of the ferromagnetic microswimmer to the $x - y$ plane cannot assure long term stable planar motion when more accurate representations of hydrodynamic interactions are taken into account.

The time after which the filament relaxes to the S-like shape is determined by the parameters Cm and ω. Since the figures 4.6 - 4.11 show results calculated up to $t = 0.1$, whereas Fig. 4.14 shows that the metastable swimming regime only lasts up to approximately $t = 0.009$, it may be concluded that by choosing appropriate values for the governing parameters it is possible to prolong the swimming regime considerably. Nevertheless, from the results described here it is evident that the accuracy of the approximations used to model hydrodynamic interactions is crucial to predicting the properties of ferromagnetic microswimmers.

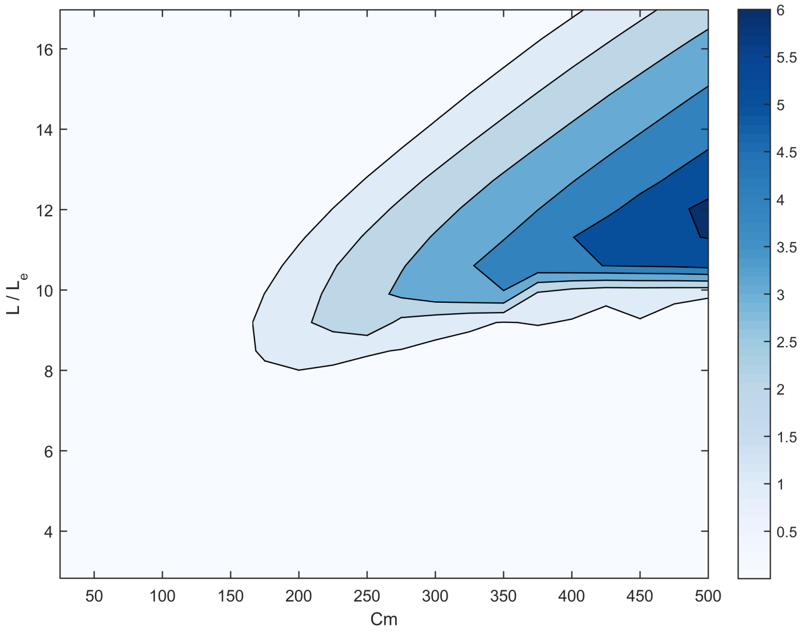

Fig. 4.10 The total displacement in the y direction y_c at dimensionless time $t = 0.1$ using the Rotne-Prager-Yamakawa tensor at $\lambda = 2$.

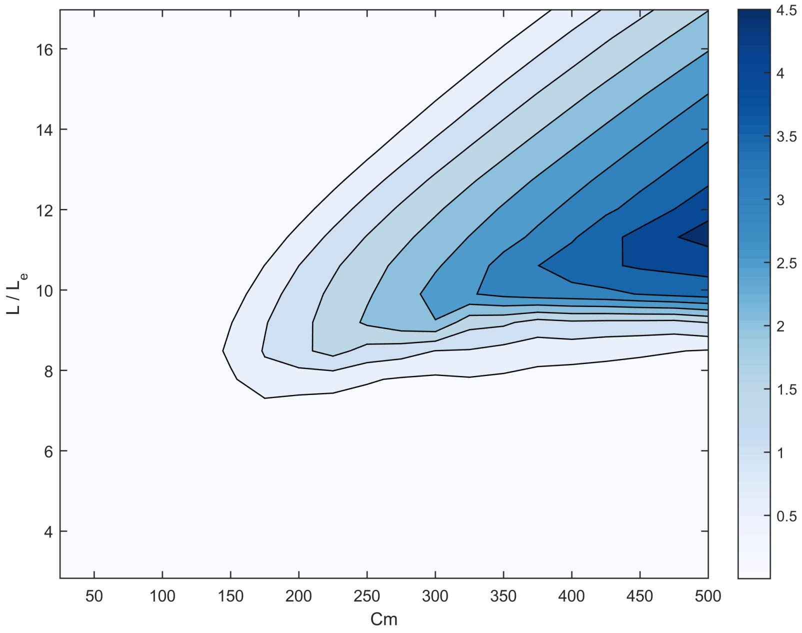

Fig. 4.11 The total displacement in the y direction y_c at dimensionless time $t = 0.1$ using the Rotne-Prager-Yamakawa tensor at $\lambda = 4$.

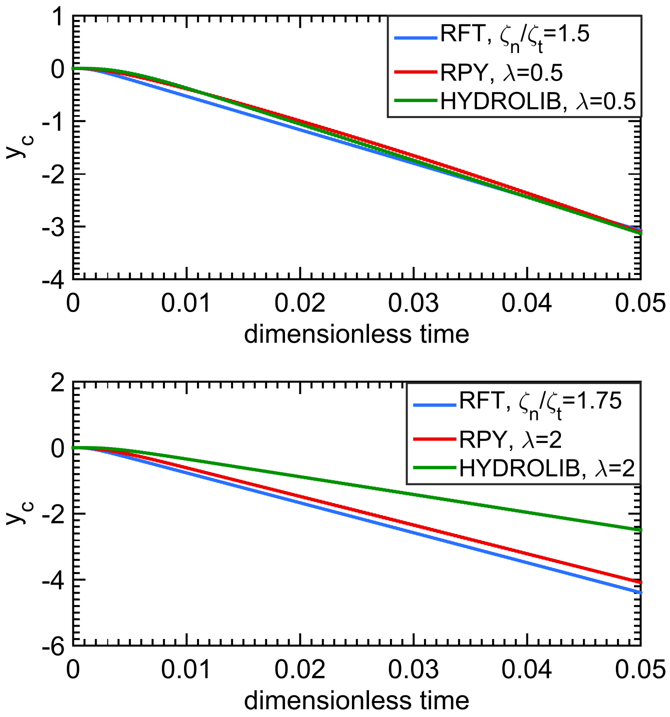

Fig. 4.12 The y coordinate of the center of mass as a function of dimensionless time: resistive force theory and more sophisticated methods. $Cm = 400$, $\omega = 20880.25$.

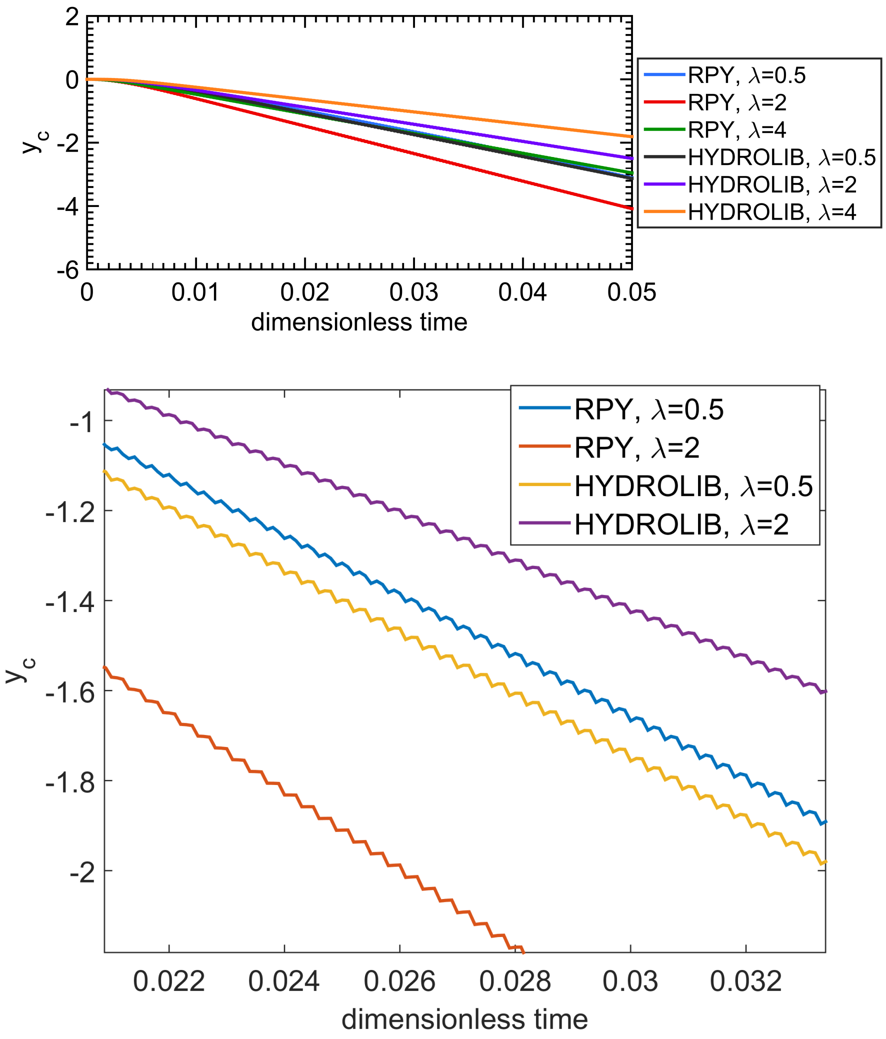

Fig. 4.13 The y coordinate of the center of mass as a function of dimensionless time: a closer look at the precision of the RPY approximation. $Cm = 400$, $\omega = 20880.25$.

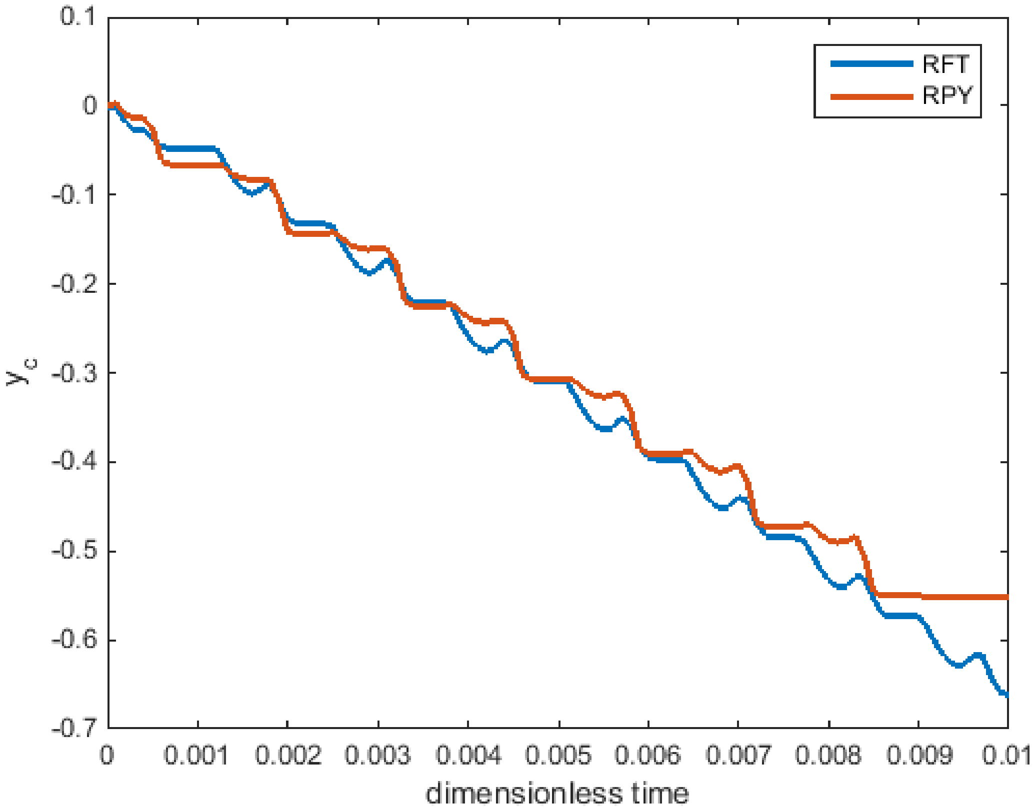

Fig. 4.14 The y coordinate of the center of mass as a function of dimensionless time at $Cm = 288$, $\omega = 4800$, $\zeta_n/\zeta_t = 1.75$, $\lambda = 0.5$.

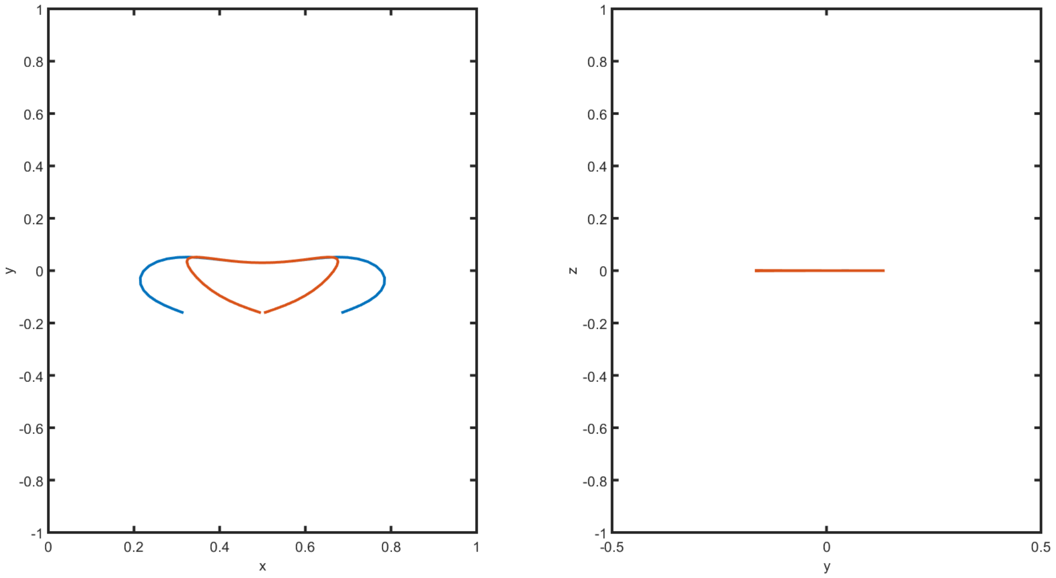

Fig. 4.15 The filament shape at $t = 0.002$, $Cm = 288$, $\omega = 4800$, $\zeta_n/\zeta_t = 1.75$, $\lambda = 0.5$ in the RFT (blue) and RPY (red) approximations.

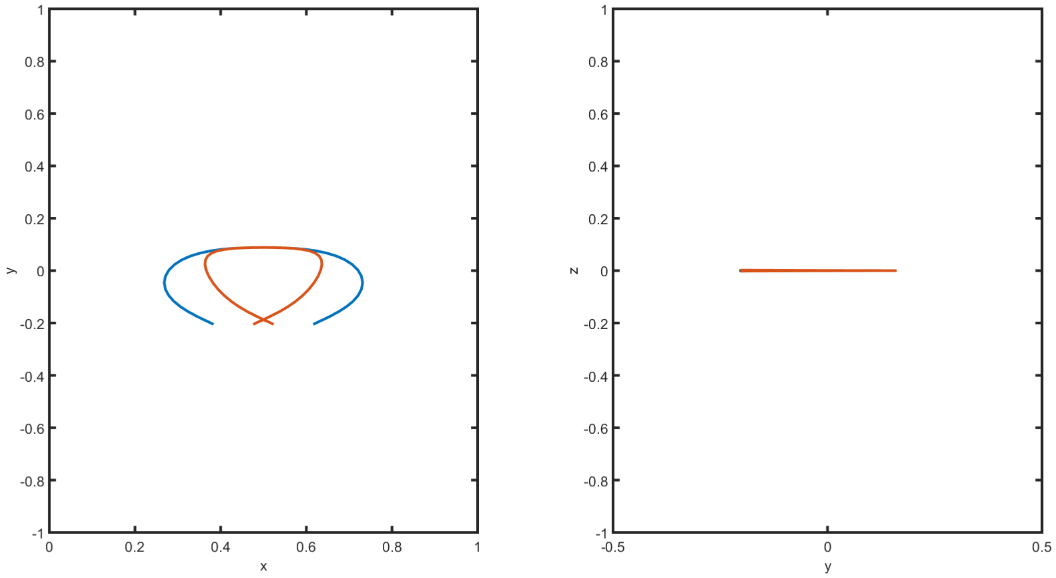

Fig. 4.16 The filament shape at $t = 0.003$, $Cm = 288$, $\omega = 4800$, $\zeta_n/\zeta_t = 1.75$, $\lambda = 0.5$ in the RFT (blue) and RPY (red) approximations.

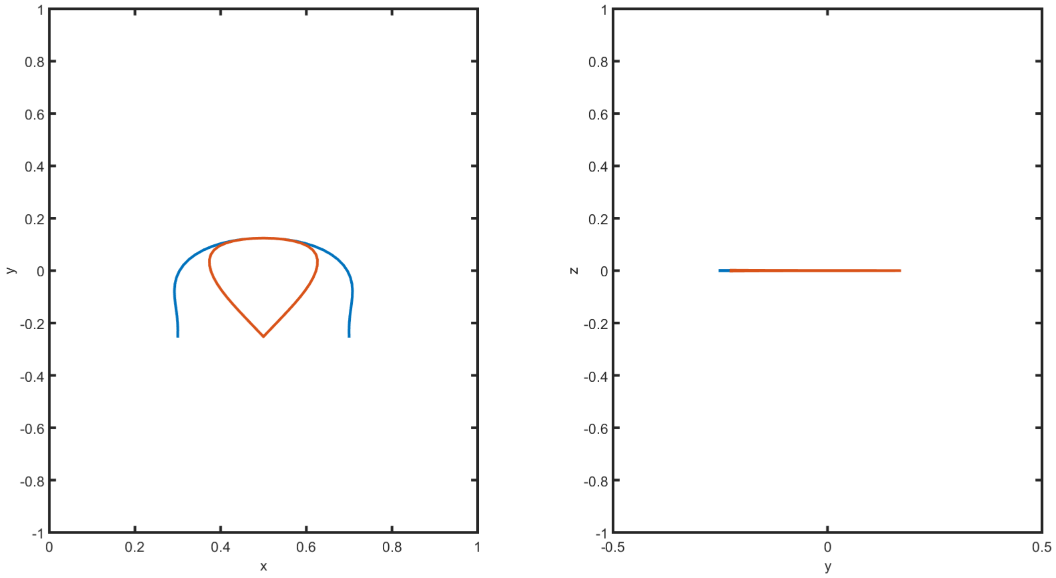

Fig. 4.17 The filament shape at $t = 0.004$, $Cm = 288$, $\omega = 4800$, $\zeta_n/\zeta_t = 1.75$, $\lambda = 0.5$ in the RFT (blue) and RPY (red) approximations.

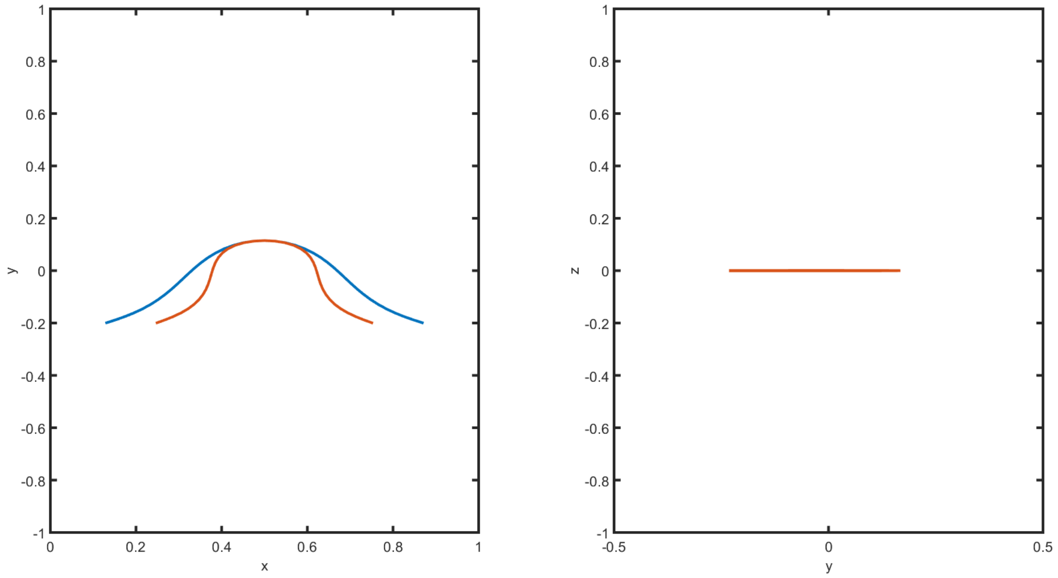

Fig. 4.18 The filament shape at $t = 0.005$, $Cm = 288$, $\omega = 4800$, $\zeta_n/\zeta_t = 1.75$, $\lambda = 0.5$ in the RFT (blue) and RPY (red) approximations.

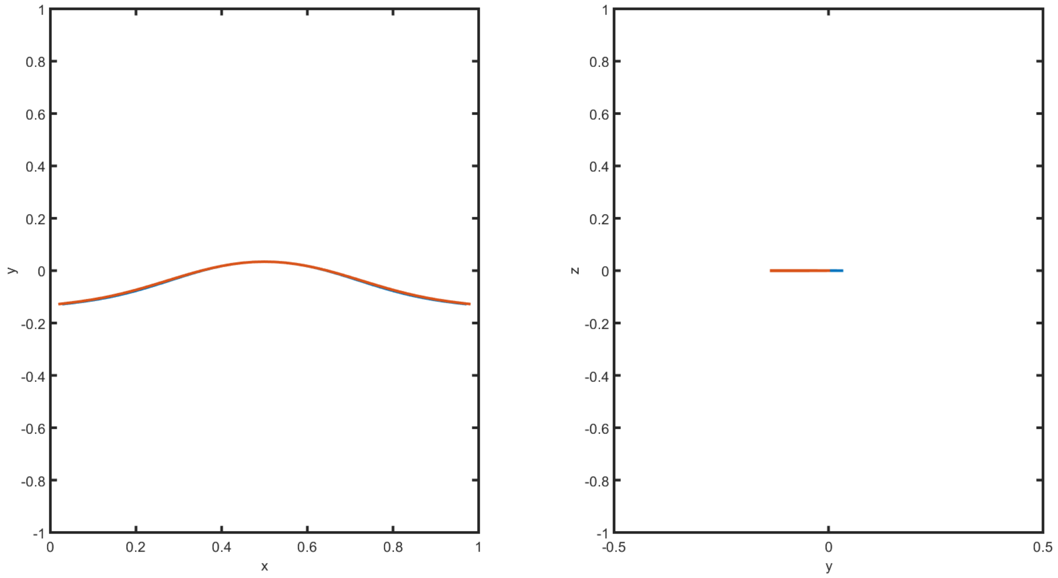

Fig. 4.19 The filament shape at $t = 0.006$, $Cm = 288$, $\omega = 4800$, $\zeta_n/\zeta_t = 1.75$, $\lambda = 0.5$ in the RFT (blue) and RPY (red) approximations.

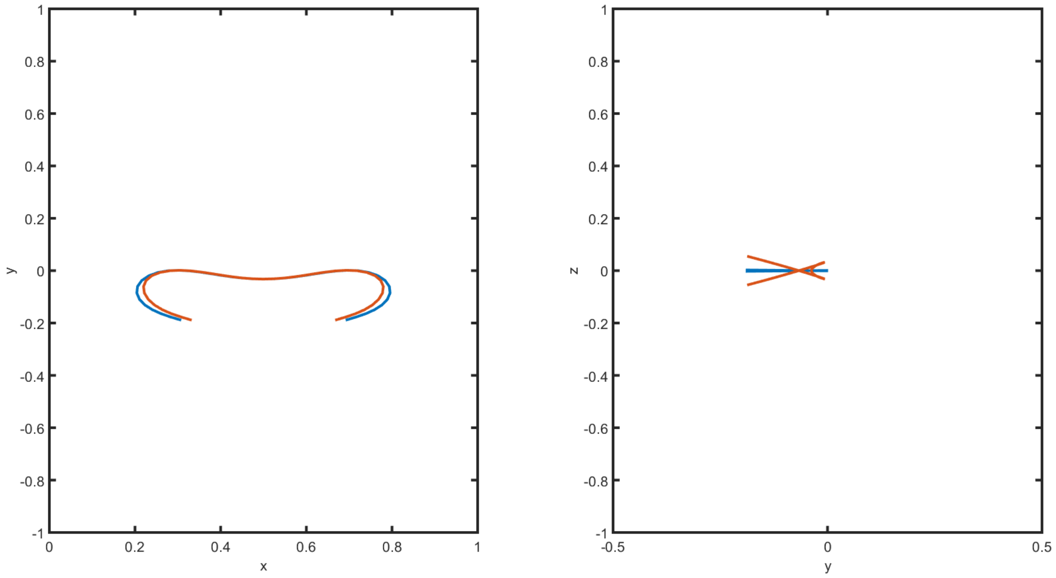

Fig. 4.20 The filament shape at $t = 0.013$, $Cm = 288$, $\omega = 4800$, $\zeta_n/\zeta_t = 1.75$, $\lambda = 0.5$ in the RFT (blue) and RPY (red) approximations.

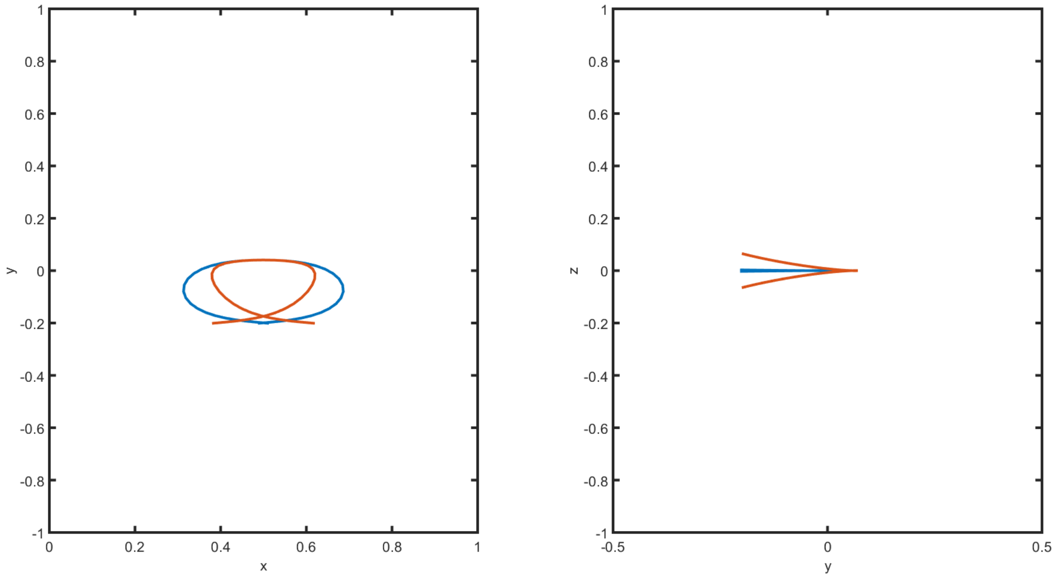

Fig. 4.21 The filament shape at $t = 0.014$, $Cm = 288$, $\omega = 4800$, $\zeta_n/\zeta_t = 1.75$, $\lambda = 0.5$ in the RFT (blue) and RPY (red) approximations.

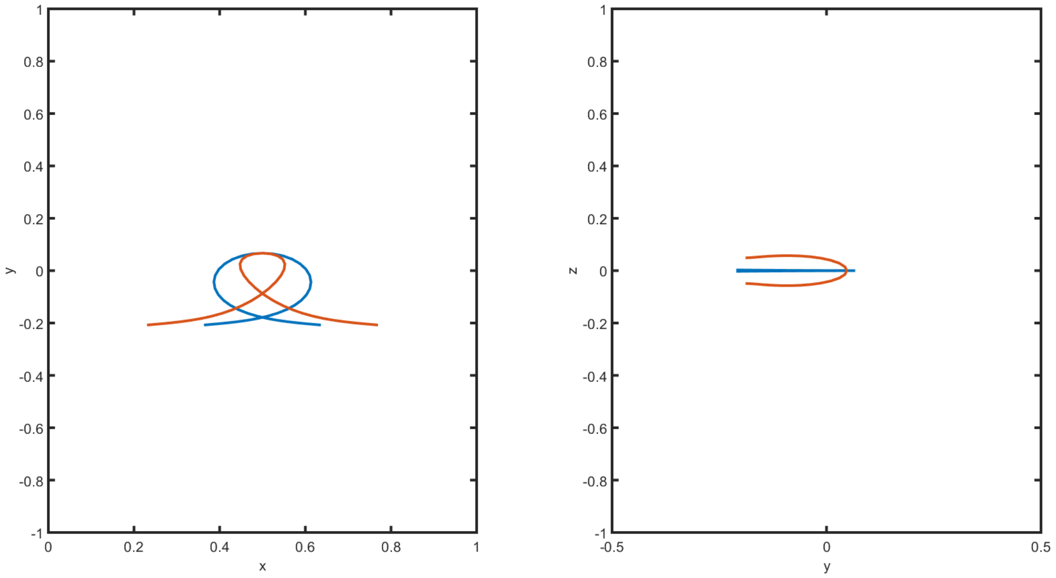

Fig. 4.22 The filament shape at $t = 0.015$, $Cm = 288$, $\omega = 4800$, $\zeta_n/\zeta_t = 1.75$, $\lambda = 0.5$ in the RFT (blue) and RPY (red) approximations.

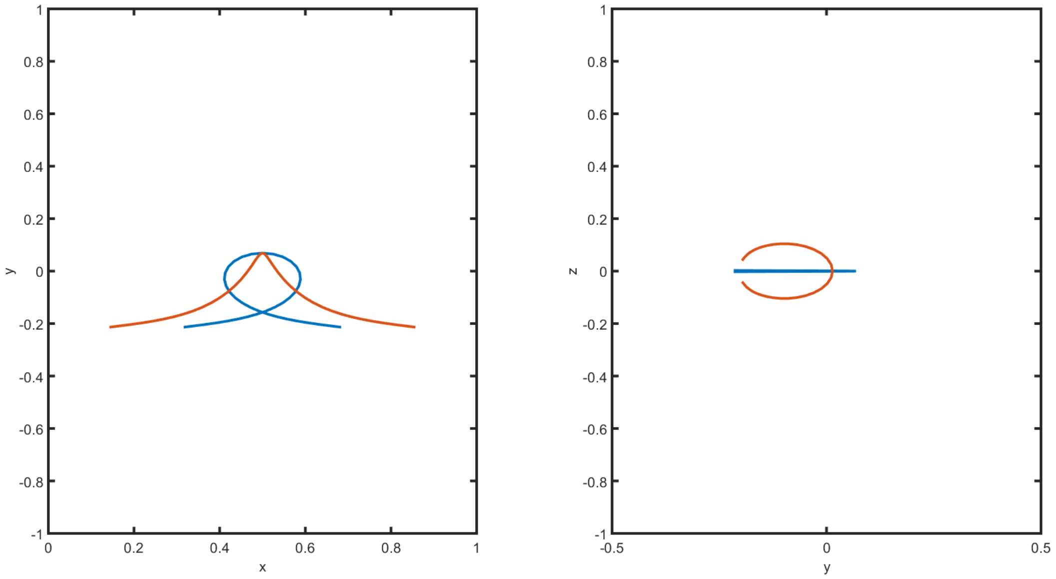

Fig. 4.23 The filament shape at $t = 0.016$, $Cm = 288$, $\omega = 4800$, $\zeta_n/\zeta_t = 1.75$, $\lambda = 0.5$ in the RFT (blue) and RPY (red) approximations.

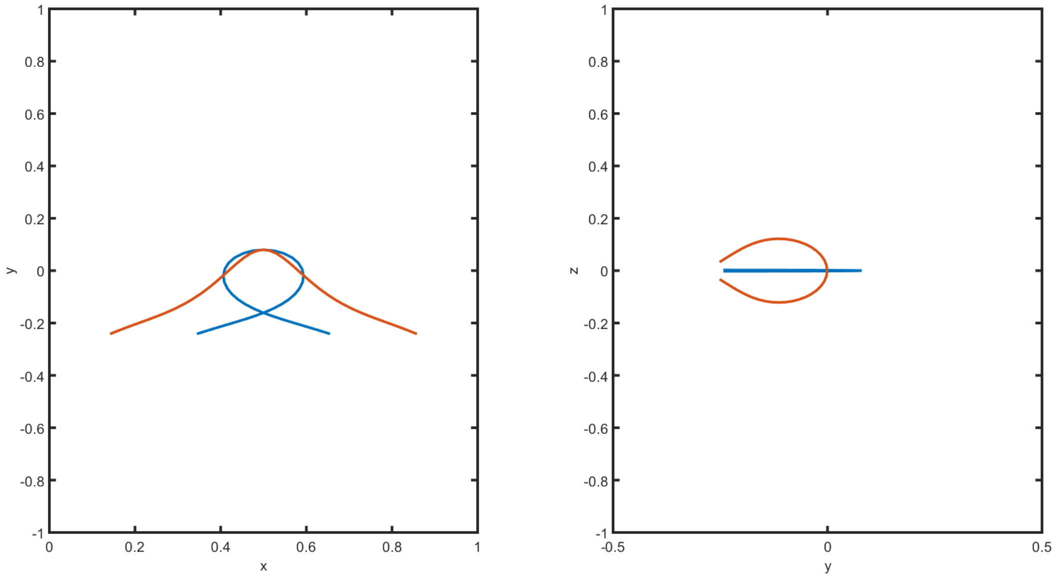

Fig. 4.24 The filament shape at $t = 0.017$, $Cm = 288$, $\omega = 4800$, $\zeta_n/\zeta_t = 1.75$, $\lambda = 0.5$ in the RFT (blue) and RPY (red) approximations.

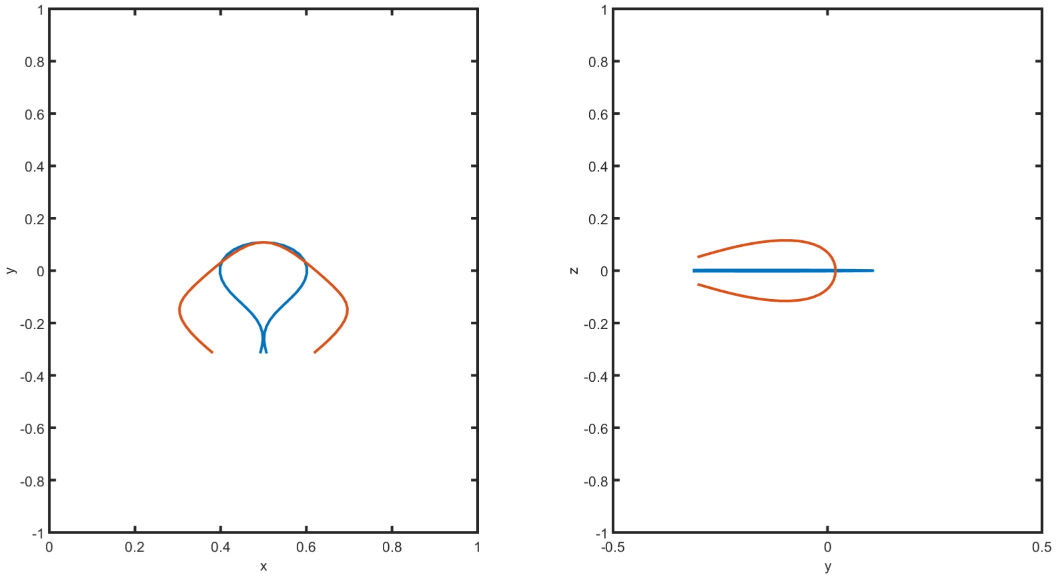

Fig. 4.25 The filament shape at $t = 0.018$, $Cm = 288$, $\omega = 4800$, $\zeta_n/\zeta_t = 1.75$, $\lambda = 0.5$ in the RFT (blue) and RPY (red) approximations.

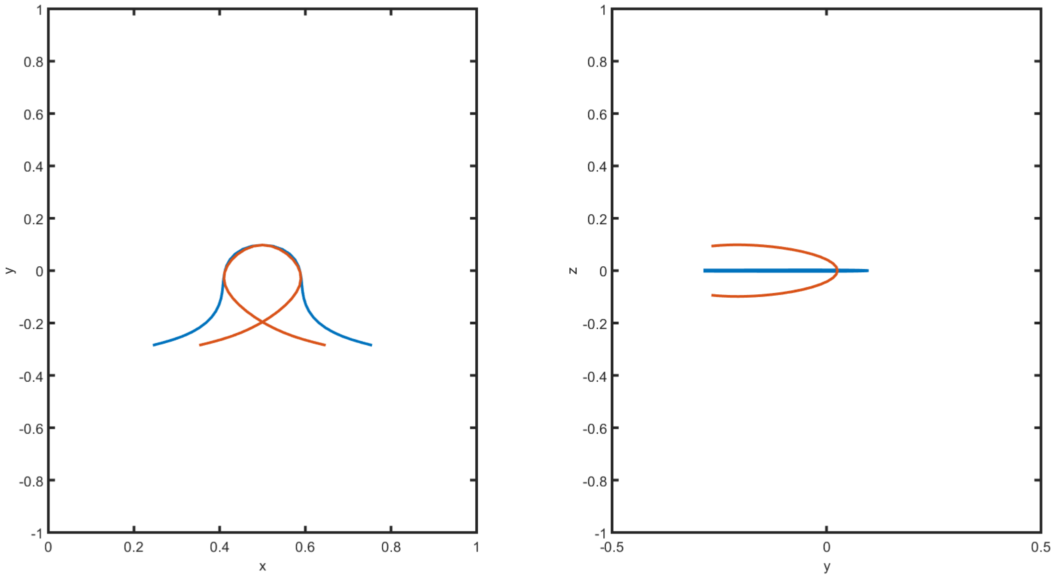

Fig. 4.26 The filament shape at $t = 0.019$, $Cm = 288$, $\omega = 4800$, $\zeta_n/\zeta_t = 1.75$, $\lambda = 0.5$ in the RFT (blue) and RPY (red) approximations.

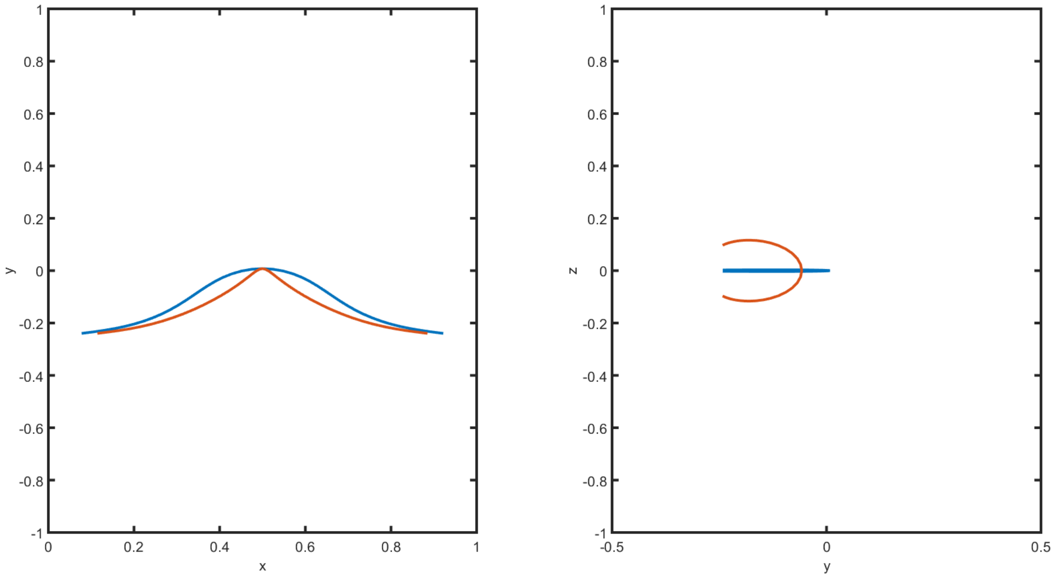

Fig. 4.27 The filament shape at $t = 0.02$, $Cm = 288$, $\omega = 4800$, $\zeta_n/\zeta_t = 1.75$, $\lambda = 0.5$ in the RFT (blue) and RPY (red) approximations.

4.1.2 The role of twist in ferromagnetic microswimmers

In the previous section we analyzed the swimming behavior of a two dimensional configuration of the ferromagnetic filament where the effects of twist were absent by definition. Let us now explore the full three dimensional dynamics of the same configuration including the effects of twist. The initial conditions are unchanged for the initial x_i and y_i (given in (4.1) and (4.2) respectively), however this time we also impose a slight perturbation in the z direction

$$z_i = \alpha x_i, \tag{4.6}$$

where α is an arbitrary small constant parameter. The role of different values of α in a constant magnetic field has been explored in previous work [26], for the purposes of this discussion we shall take $\alpha = 10^{-4}$. Ultimately, the larger the value of α the faster the filament will relax to a stable state in which the filament's center of mass is stationary.

We begin by examining the filament configurations for a representative set of parameter values chosen to correspond to those used in a previous work, where the basic filament dynamics were described in the resistive force theory approximation and neglecting the effects of twist [27]. We show two important snapshots of the dynamics of the filament in Figures 4.28 and 4.29, where four different filament configurations (resistive force or RPY hydrodynamics, with or without the effects of twist) are superimposed on top of each other at the same instant to show the differences. These results enable us to distinguish the relative importance of the effects of twist from the impact of different hydrodynamic approximations. As seen in Fig. 4.28, the two cases where the Rotne-Prager-Yamakawa tensor was used relax to the stable S-like state faster than the two configurations that employed the resistive force theory approach of anisotropic friction coefficients. Fig. 4.29 shows a much later stage where all four filaments have transitioned to the stable S-like state and shows that, despite the fairly small twist diffusion constant used ($d_0 = 1$) the use of a more accurate approximation for the calculation of the hydrodynamic interactions has a considerably larger impact on the overall dynamics of the filament than the effects of twist. These conclusions are further supported by the time dependence of the center of mass coordinate in the y direction (the direction of motion for the U-like metastable state before it relaxes to the S-like state and the filament's center of mass ceases to swim), shown in Figures 4.30 and 4.31 for different values of the twist diffusion constant d_0 and in both the resistive force theory and the RPY approximation. To further illustrate the role of twist as distinct from any impact of hydrodynamic approximations, we also show snapshots of filament configurations at different times computed in the RFT approximation with $d_0 = 1$ in $x - y$ and $x - z$ projections shown in Figures 4.32, 4.33 and 4.34. All three snapshots are taken during the transition period from the propulsive U-like state and the stationary S-like state, since the effects of twist are non-existent in purely planar motion. It is easy to see from these three snapshots that while taking the effects of twist into account does induce minor quantitative changes in the shape of the filament during the transitionary regime, these do not affect the overall dynamics of the filament in any qualitatively important way and may be reasonably neglected in many cases of practical interest.

It may be concluded that for the kind of ferromagnetic microswimmers studied in this work the effects of twist are not particularly important unless the filament's twist diffusion constant is extremely small whereas hydrodynamic interactions play a crucial role and their accurate calculation is of paramount importance to precisely calculating the dynamics of the microswimmers.

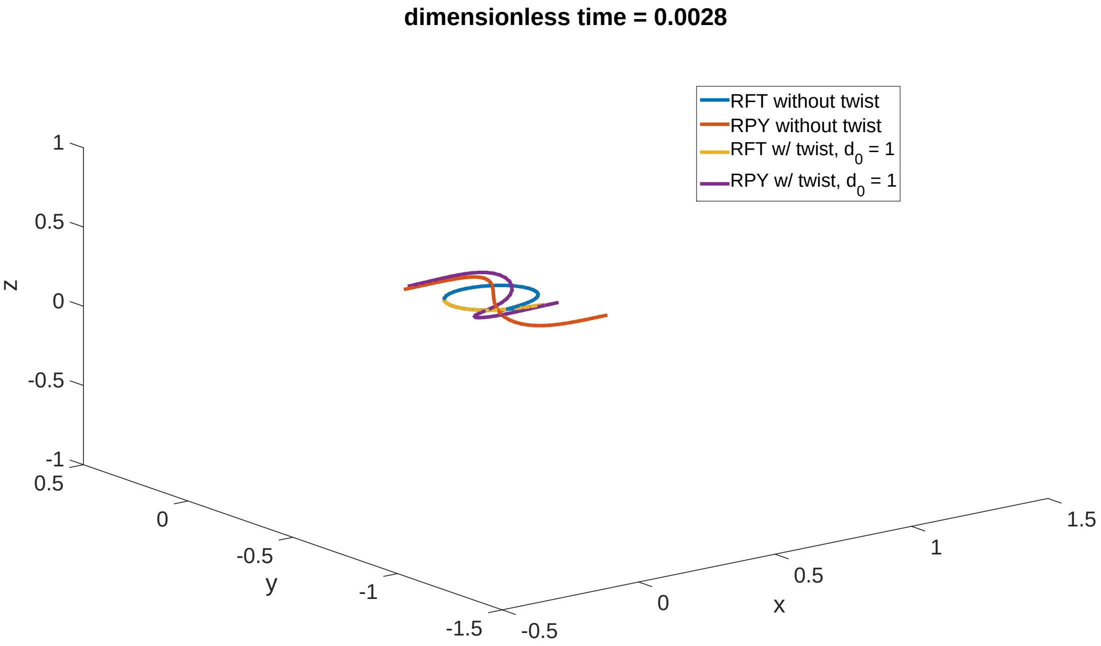

Fig. 4.28 The role of twist and different hydrodynamic approximations in the dynamics of the fully 3D ferromagnetic microswimmer at $t = 0.0028$. $\alpha = 10^{-4}$, $Cm = 288$, $\omega = 4800$, $\lambda = 0.5$, $\zeta_n/\zeta_t = 1.75$.

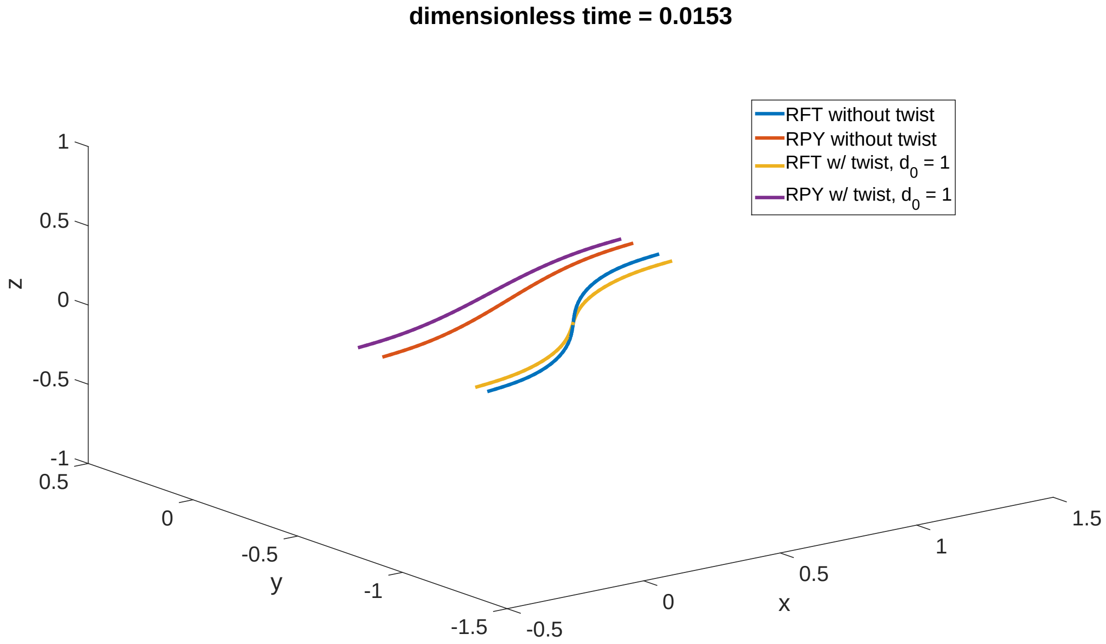

Fig. 4.29 The role of twist and different hydrodynamic approximations in the dynamics of the fully 3D ferromagnetic microswimmer at $t = 0.0153$. $\alpha = 10^{-4}$, $Cm = 288$, $\omega = 4800$, $\lambda = 0.5$, $\zeta_n/\zeta_t = 1.75$.

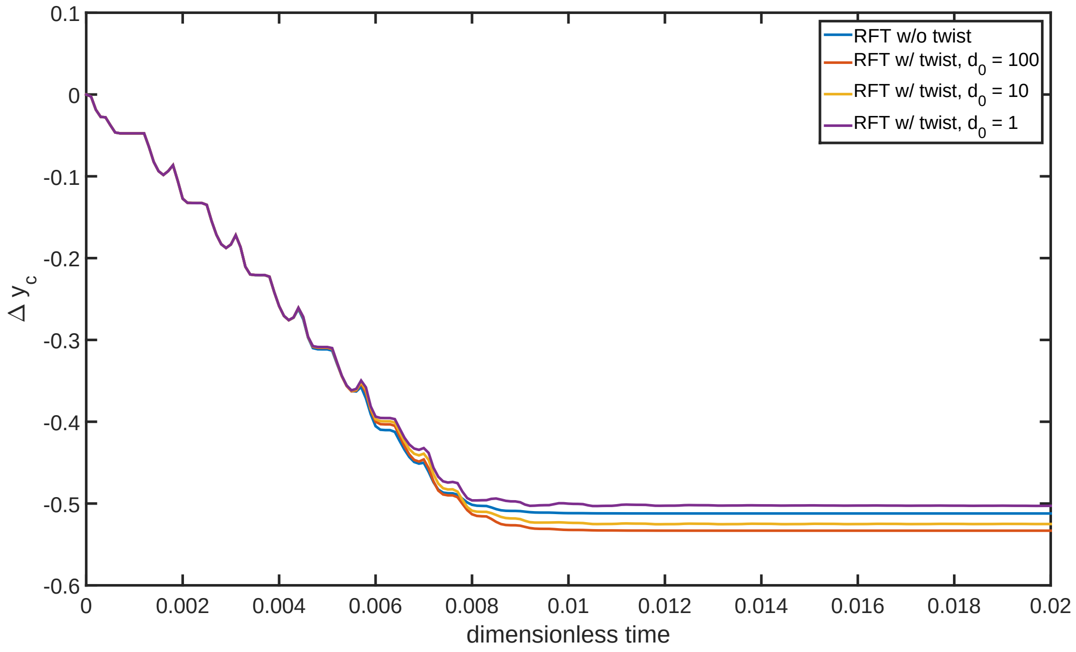

Fig. 4.30 The role of twist at different values of the twist diffusion constant in the dynamics of the fully 3D ferromagnetic microswimmer in the resistive force theory (RFT) approximation. $\alpha = 10^{-4}$, $Cm = 288$, $\omega = 4800$, $\zeta_n/\zeta_t = 1.75$.

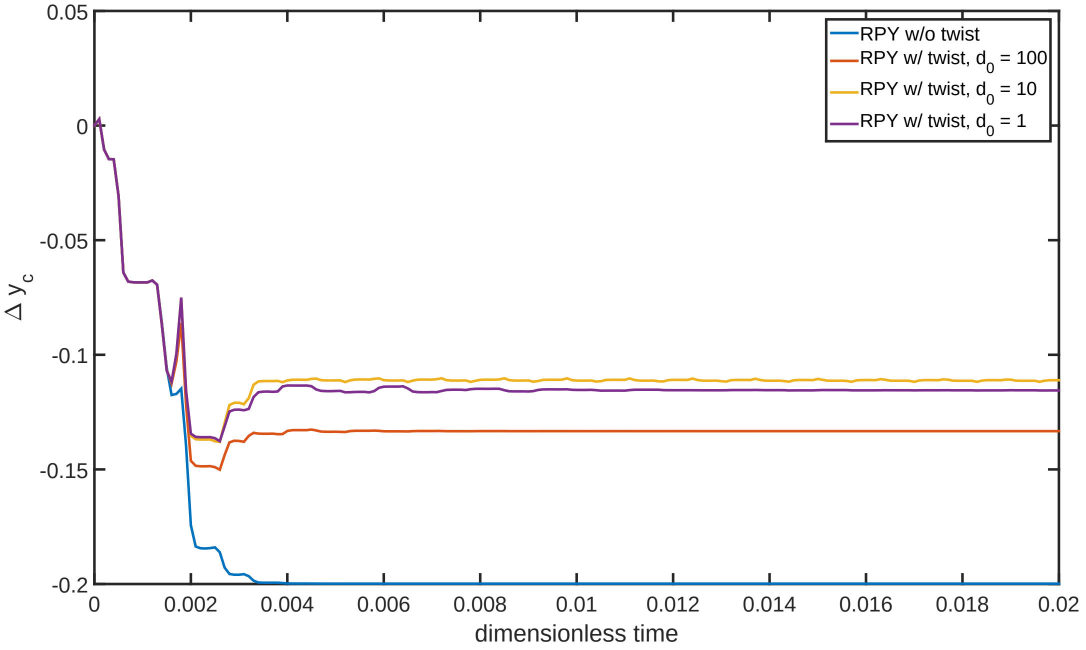

Fig. 4.31 The role of twist at different values of the twist diffusion constant in the dynamics of the fully 3D ferromagnetic microswimmer in the Rotne-Prager-Yamakawa (RPY) approximation. $\alpha = 10^{-4}$, $Cm = 288$, $\omega = 4800$, $\lambda = 0.5$.

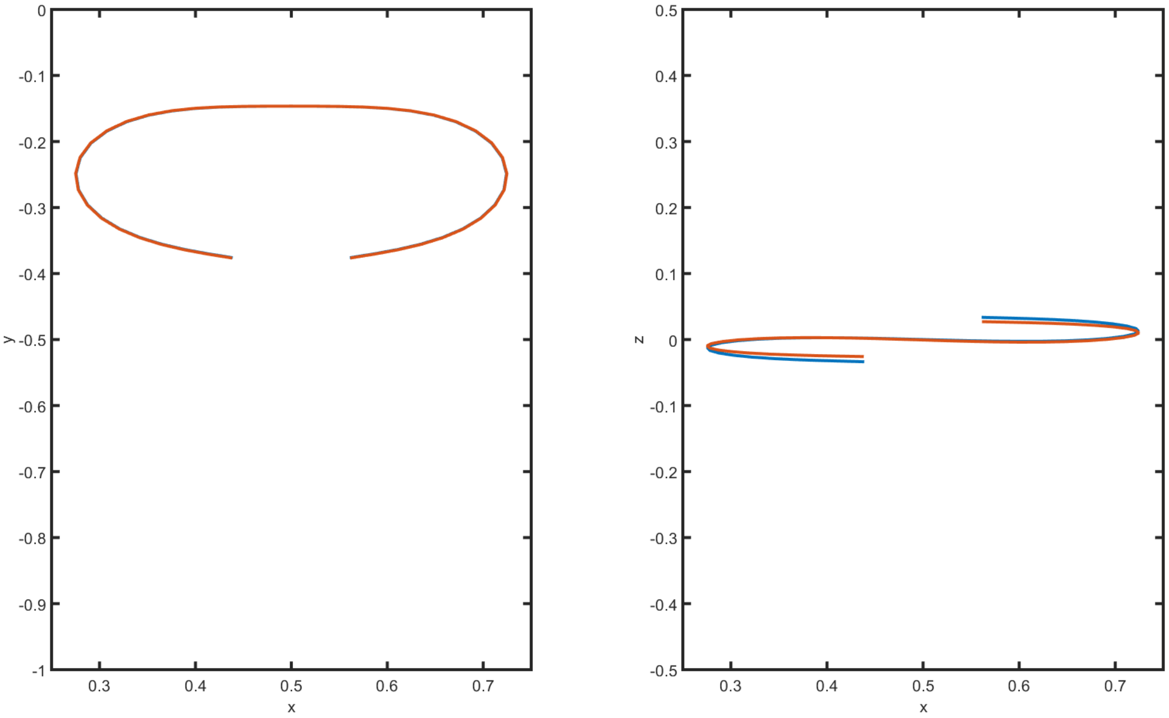

Fig. 4.32 Comparison of the filament shapes with (shown in red) and without (shown in blue) the effects of twist taken into account. Dimensionless time $t = 0.0039, Cm = 288, \omega = 4800$.

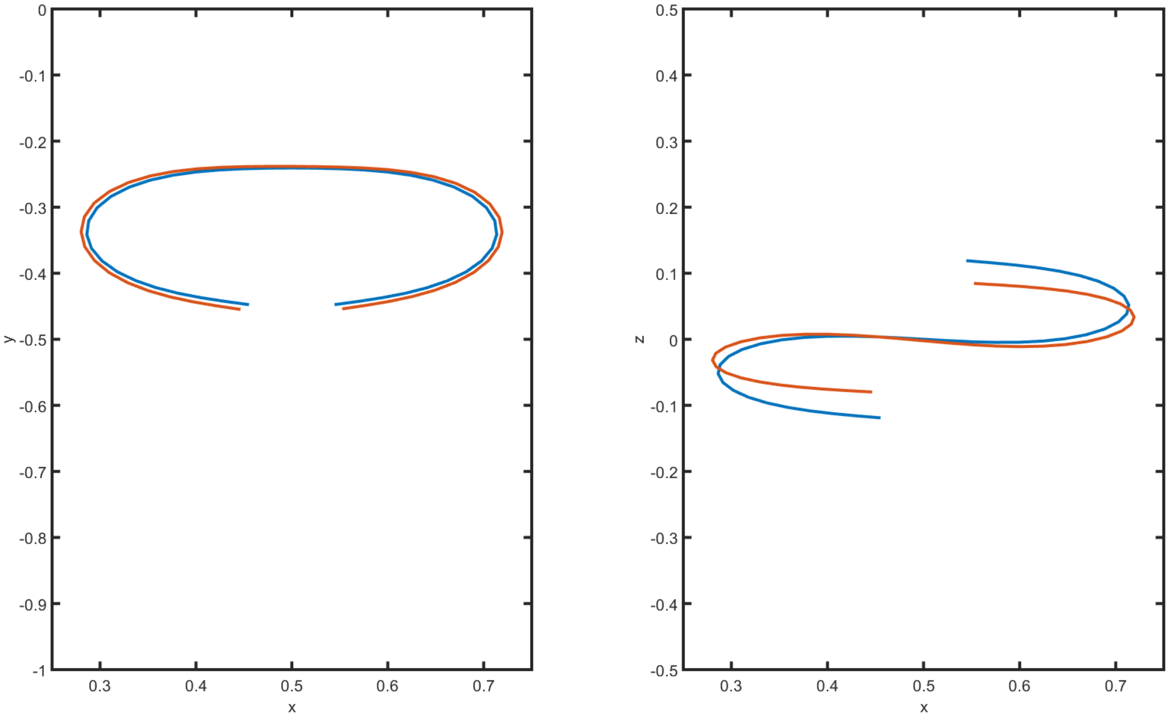

Fig. 4.33 Comparison of the filament shapes with (shown in red) and without (shown in blue) the effects of twist taken into account. Dimensionless time $t = 0.0052, Cm = 288, \omega = 4800$.

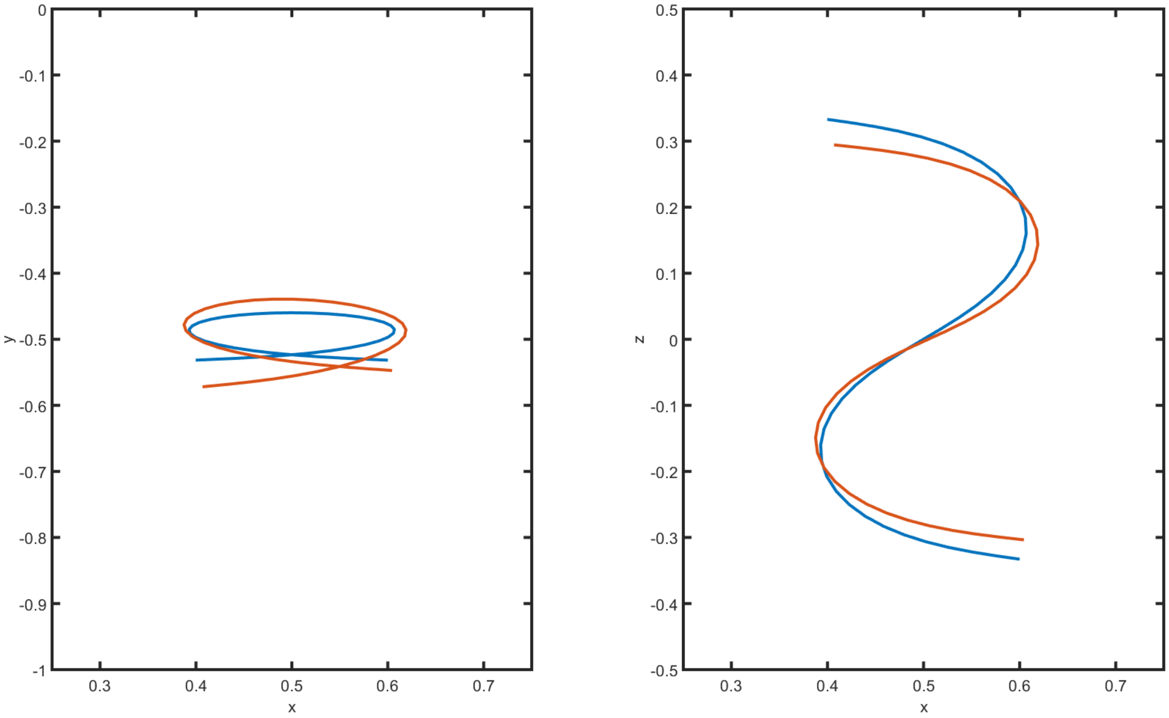

Fig. 4.34 Comparison of the filament shapes with (shown in red) and without (shown in blue) the effects of twist taken into account. Dimensionless time $t = 0.0078, Cm = 288, \omega = 4800$.

4.2 Ferromagnetic filaments with a fixed end (cilia)

The typical model situation for a ferromagnetic filament with a fixed end is as an artificial cilia, with a view towards potential application as a microfluidic mixer. In this scenario one of the filament's ends is fixed (considered to be attached to a wall located in the $x-y$ plane, though we do not consider the hydrodynamic effects of the wall for simplicity) and the other is free to be actuated by an external rotating magnetic field. We have described the basic dynamics of such a system in a previous work [14], neglecting hydrodynamic interactions and the effects of twist entirely. While the latter may indeed be neglected from physical considerations, as we would naturally expect a high twist diffusion constant for any artificial cilia useful for mixing microfluids, the effect of hydrodynamic interactions is worth investigating. While it is natural to expect any corrections to the shape of the cilia to be quantitative rather than qualitative, the approximation of hydrodynamic interactions will also enable us to calculate the flow fields induced by the ciliary motion, which is in turn of crucial importance to describing the efficiency of any prospective mixing device.

The filament is initially defined to be perfectly straight in the z direction. An external magnetic field rotating in the $x-y$ plane is then applied so that $\mathbf{H} = Cm(\cos\omega t, \sin\omega t, 0)$. The magnetic field then induces bending in the filament, the extent of which depends on the value of the magnetoelastic number, and the bent filament rotates synchronously with the external magnetic field. An example of a typical filament configuration is shown in Fig. 4.35 for different types of hydrodynamic approximations. Evidently, while the basic mode of behavior remains, the degree to which the filament bends is changed substantially. It should be noted, however, that neither resistive force theory nor the Rotne-Prager-Yamakawa tensor take into account the shielding effect of the wall, which will introduce an error dependent on the distance from the wall. Appropriate corrections will be introduced into the model in the future.

The use of the Rotne-Prager-Yamakawa tensor and the linearity of the Stokes equations enables us to calculate the flow fields that surround the cilia. In Chapter 2.4 we obtained the expression (eq. (2.80))

$$\mathbf{u}(\mathbf{r}) = \int \mathbf{G}(\mathbf{r}-\mathbf{r}') \cdot \mathbf{f}(\mathbf{r}') d\mathbf{r}'. \tag{4.7}$$

In the context of our numerical model, each marker point essentially exerts a force $\mathbf{f}_i = \sum_{j=1, j\neq i}^{p+1} \boldsymbol{\mu}_{ij}^{-1} \mathbf{v}_j$ on the surrounding fluid, which lets us calculate the fluid velocity at an arbitrary point by numerically integrating (4.7). In order to avoid numerical issues with

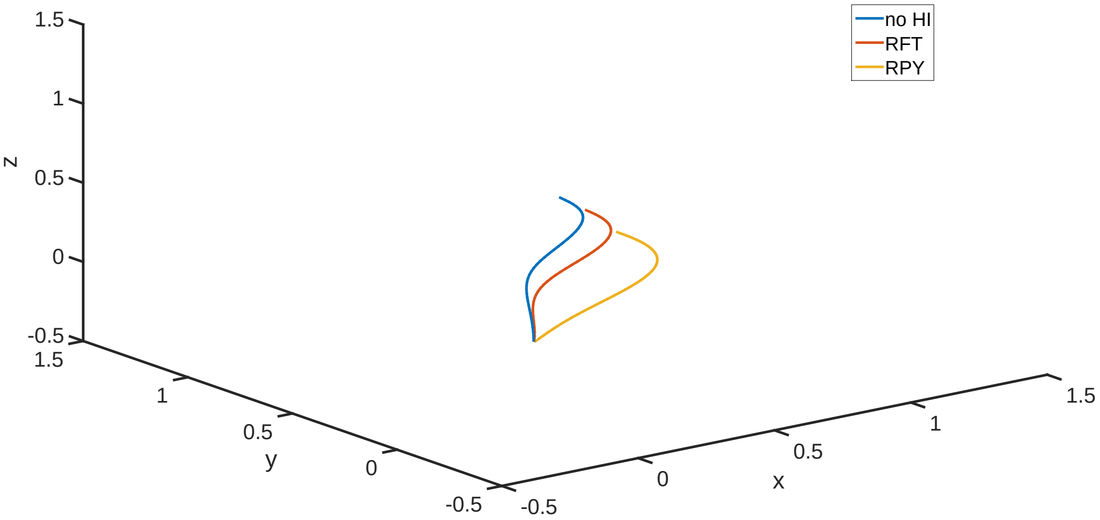

Fig. 4.35 Filament configuration at $t = 0.02$ for different hydrodynamic approximations. $Cm = 288$, $\omega = 4800$, $\zeta_n/\zeta_t = 1.75$, $\lambda = 0.5$.

the integral (4.7), we employ a regularized version introduced by Cortez [19], which in dimensionless form reads

$$\mathbf{J}_\varepsilon = \frac{|\mathbf{r}|^2 + 2\varepsilon^2}{(|\mathbf{r}|^2 + \varepsilon^2)^{3/2}}\mathbf{I} + \frac{\mathbf{r} \otimes \mathbf{r}}{(|\mathbf{r}|^2 + \varepsilon^2)^{3/2}}, \tag{4.8}$$

where ε is a small regularization parameter. We use the value $\varepsilon = 0.02$. An example of a typical 3D flow field obtained from (4.7) is shown in Fig. 4.36. Since the full 3D visualization is difficult to interpret directly, we also show two $x - y$ projections at two different z coordinates - $z = 0.5$ in 4.37 and $z = 1$ in 4.38. Evidently, the rotating filament induces a circular flow pattern generally conducive to fluid mixing. At $z \leq 1$ a vortex close to the filament may be seen (Fig. 4.37), whereas the flow above the filament (Fig. 4.38) the flow pattern is more uniform.

In order to understand the impact of the primary dimensionless parameters that govern the motion of the filament - Cm and the dimensionless frequency ω we proceed analogously to Section 4.1.1 and conduct a comprehensive series of simulations for a wide range of values of these parameters and measure the resulting fluid velocity at a fixed point. Since the overall flow pattern does not change qualitatively so long as the external field remains confined to rotating in the $x - y$ plane, we expect the results to be indicative of the kind of values for

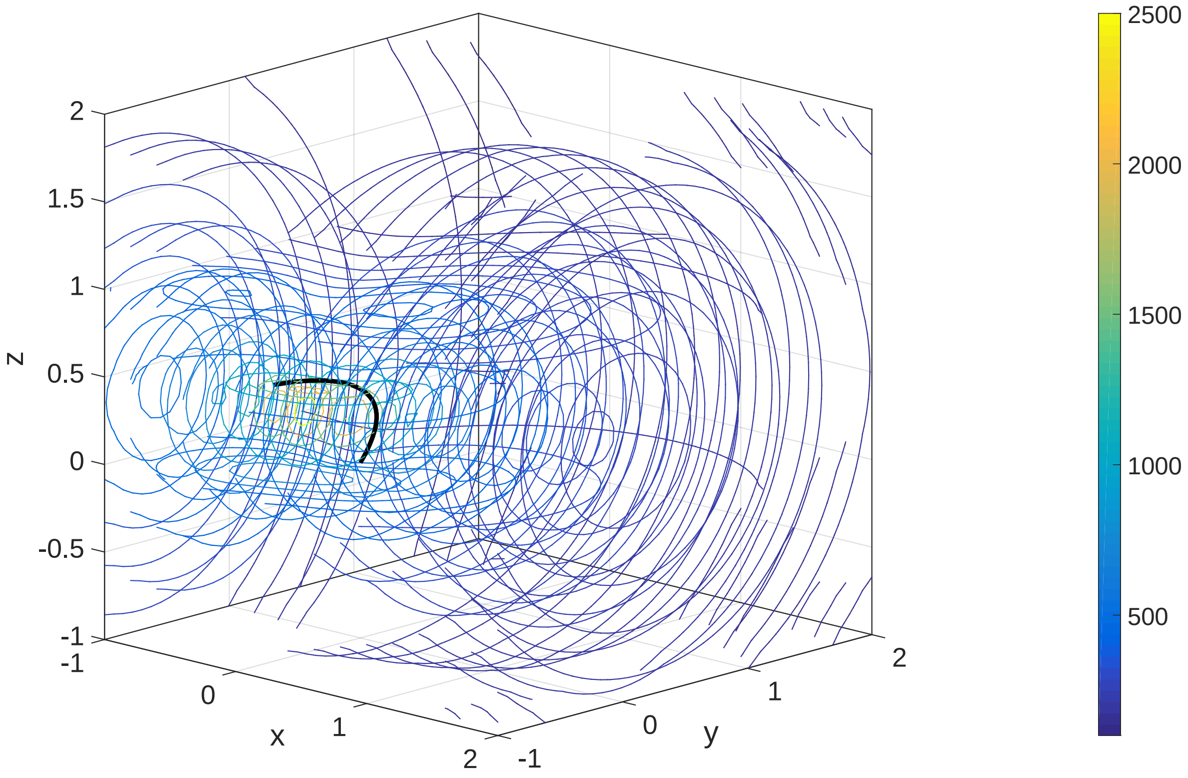

Fig. 4.36 Flow field induced by the rotating filament at $t = 0.005$, the contour lines denote the dimensionless fluid velocity magnitude. $Cm = 288$, $\omega = 4800$, $\lambda = 0.5$.

Cm and ω that might be chosen for a reasonably efficient microfluidic mixer. The mean dimensionless fluid velocity values at the point $\mathbf{r}_0 = (1, 1, 0.5)$ as functions of the parameters Cm and $L/L_e = \omega^{1/4}$ are shown in Fig. 4.39. We can see that as the magnetoelastic number Cm is increased, the range of dimensionless frequencies at which the mean fluid velocity is largest is more and more constrained.

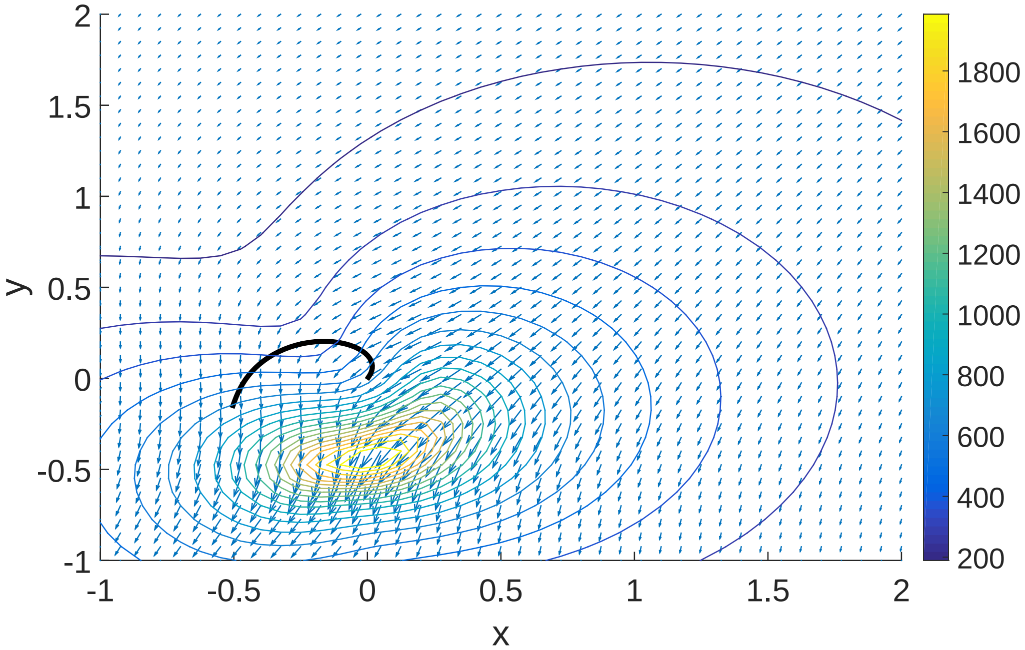

Fig. 4.37 Flow field induced by the rotating filament at $t = 0.005$ in the $x-y$ plane at $z = 0.5$, the contour lines denote the dimensionless fluid velocity magnitude while the arrows show the direction and magnitude of the velocity vectors. $Cm = 288$, $\omega = 4800$, $\lambda = 0.5$.

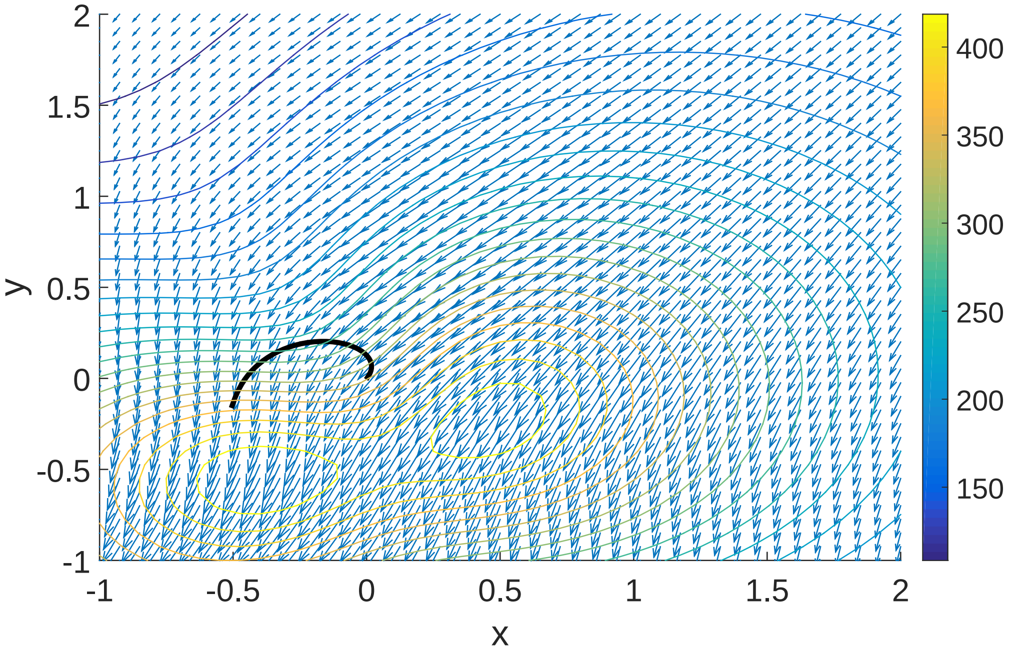

Fig. 4.38 Flow field induced by the rotating filament at $t = 0.005$ in the $x-y$ plane at $z = 1$, the contour lines denote the dimensionless fluid velocity magnitude while the arrows show the direction and magnitude of the velocity vectors. $Cm = 288$, $\omega = 4800$, $\lambda = 0.5$.

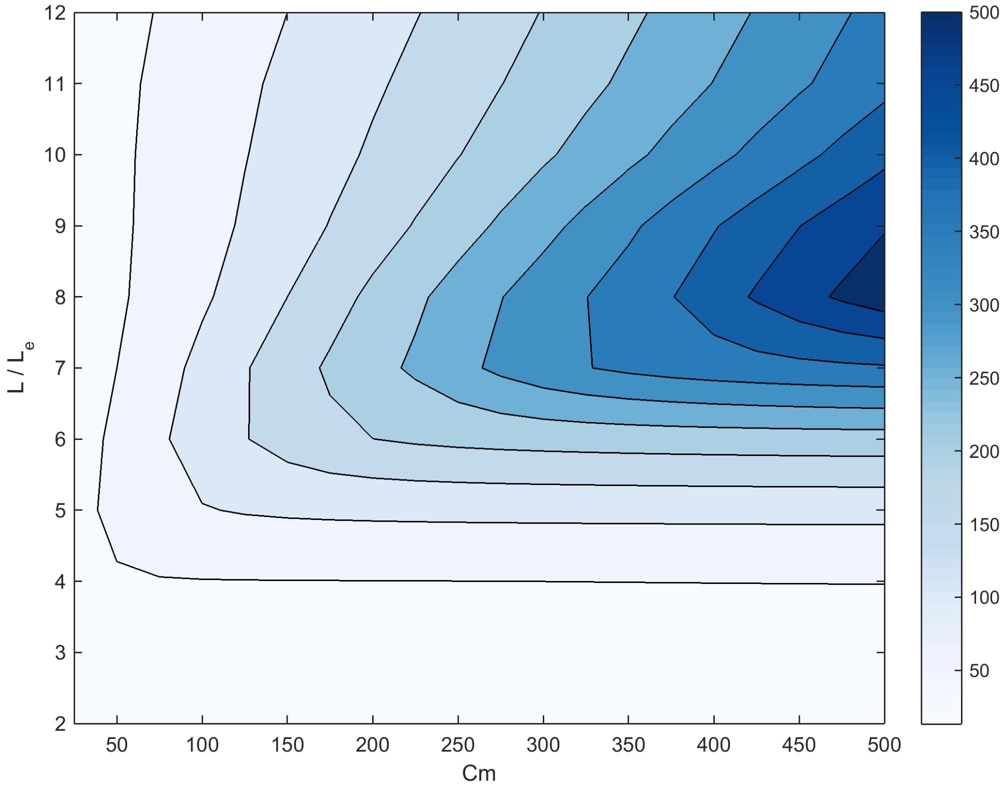

Fig. 4.39 Mean dimensionless fluid velocity induced by the rotating filament at $t = 0.005$ at the point $\mathbf{r}_0 = (1, 1, 0.5)$, the contour lines denote the dimensionless fluid velocity magnitude quantified by the color scale shown on the right. $\lambda = 0.5$.

4.3 Superparamagnetic filaments

Up until this point in the chapter we have only concerned ourselves with ferromagnetic filaments. While it is true that most of the research we have done is focused on ferromagnetic filaments, the model we have formulated in Chapters 2 and 3 describes superparamagnetic filaments as well. The basic dynamics of superparamagnetic filaments with free ends are well known. In a constant magnetic field, the filaments form hairpin-like shapes [12], which are metastable. In a time varying field these hairpins may swim depending on the kind of field that is applied.

We begin by once again taking advantage of an opportunity to verify the results of our model against the existing literature. To do so, we apply a constant magnetic field in the y direction and set the initial conditions of the filament to the same two dimensional configuration we used to investigate the basic properties of ferromagnetic filaments in section 4.1.1. These are given by equations (4.1), (4.2) and (4.3). We therefore have an almost straight configuration slightly bent in the direction of the applied field. Since superparamagnetic filaments tend to align with the external field, this represents a suitable setting to observe the formation of the metastable hairpin-like shapes.

We carry out numerical simulations over a wide range of values for the magnetoelastic number Cm using the same stopping condition as before - each calculation is carried out until the change in the maximal curvature in the filament over the last 100 timesteps decreases below 0.1%. A representative series of resulting configurations is given in Figures 4.40, 4.41, 4.42 and 4.43. Of the eight configurations portrayed in the aforementioned figures the first five are examples the characteristic hairpin shapes described in [12], [13] and elsewhere, while the last three correspond to the higher order deformation modes described by Ērglis *et al* in [13]. Both types of shapes have also been observed experimentally (also detailed in [29]).

The shapes observed in numerical calculations using the model established in this work fully conform to the critical values of the magnetoelastic number described in [13] and previous works. In particular (here and elsewhere the critical values will be given in accordance with the definition of the magnetoelastic number used in this work which may differ by a constant factor of 4 from publications that use $2L$ for the length of the filament), the critical value for the hairpin formation (referred to as the first odd mode in the reference article) is given as $Cm_c = \pi^2/2$ and we observe hairpin formation starting from $Cm \approx 5$. The higher order shapes are described in [29] at $Cm = 32$, we also begin to observe them in the interval $30 < Cm < 35$. This result constitutes a further verification of our model, in particular the implementation of superparamagnetic filaments appears to be in full accordance with previous results (where direct comparison is possible), including results derived from entirely different formulations of the governing equations (such as the tangent angle formalism) which have been verified experimentally. In addition, the maximal curvature of the metastable superparamagnetic filament shapes as a function of the magnetoelastic number *Cm* is given in Fig. 4.44.

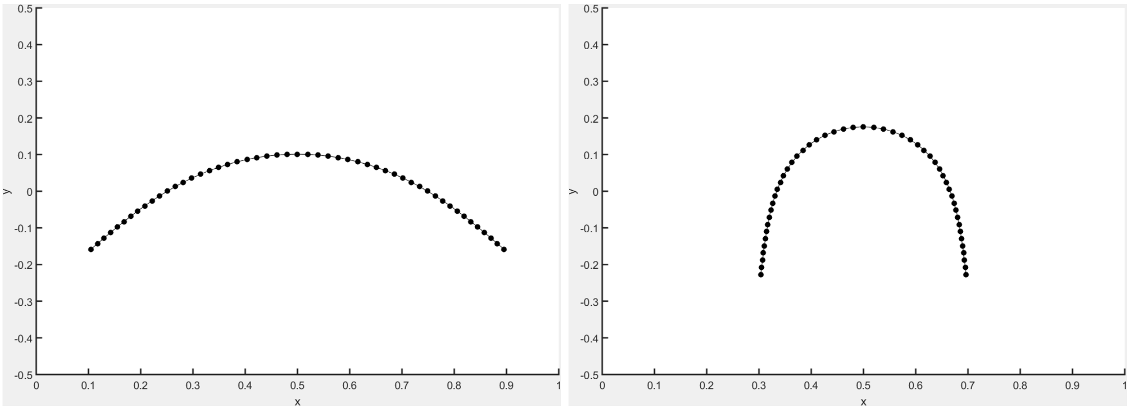

Fig. 4.40 2D hairpin configuration of the superparamagnetic filament in a constant field with $Cm = 6$ (left), $Cm = 8$ (right).

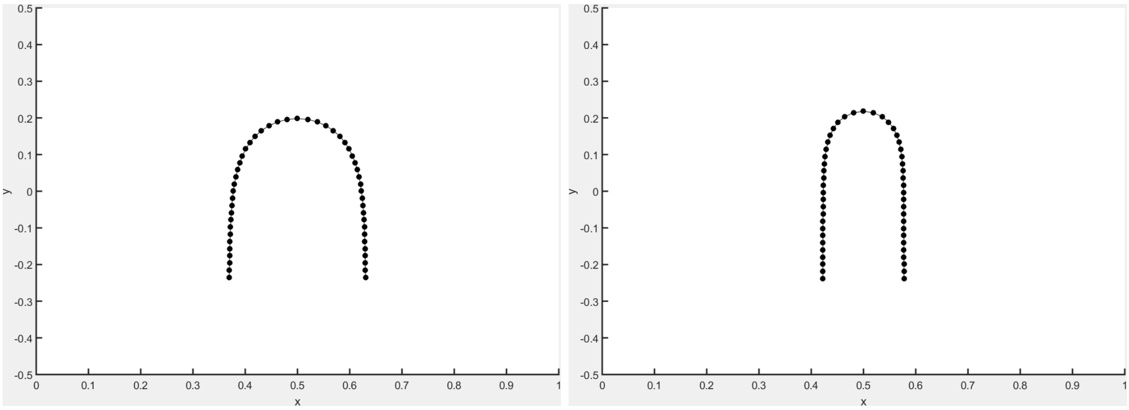

Fig. 4.41 2D hairpin configuration of the superparamagnetic filament in a constant field with $Cm = 12$ (left), $Cm = 20$ (right).

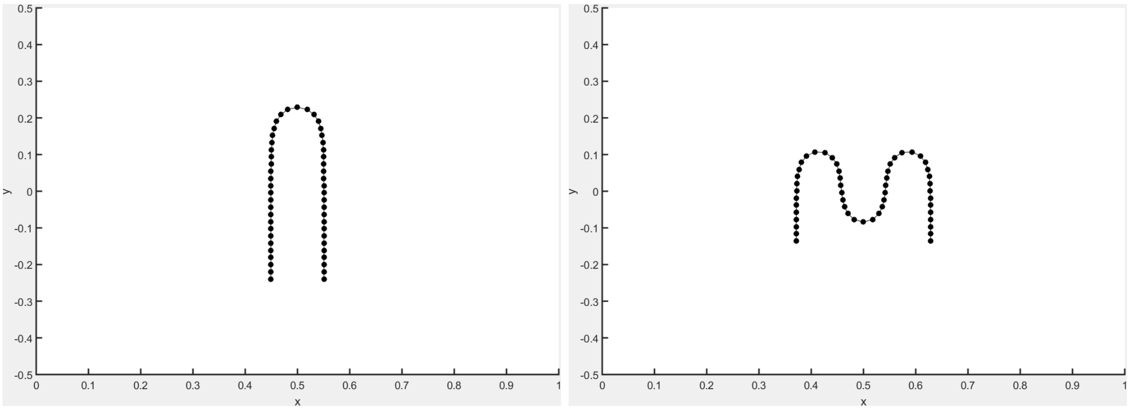

Fig. 4.42 2D hairpin configuration of the superparamagnetic filament in a constant field with $Cm = 30$ (left), $Cm = 35$ (right).

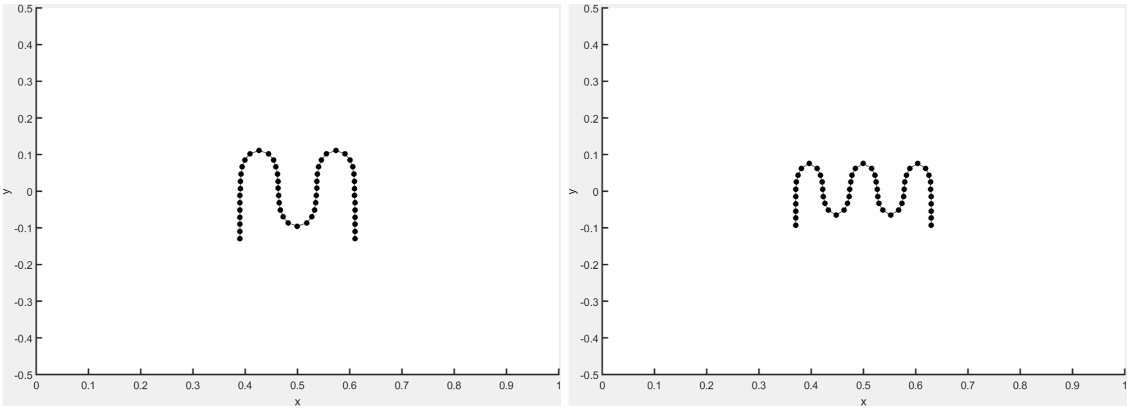

Fig. 4.43 2D configuration of the superparamagnetic filament in a constant field with $Cm = 40$ (left), $Cm = 50$ (right).

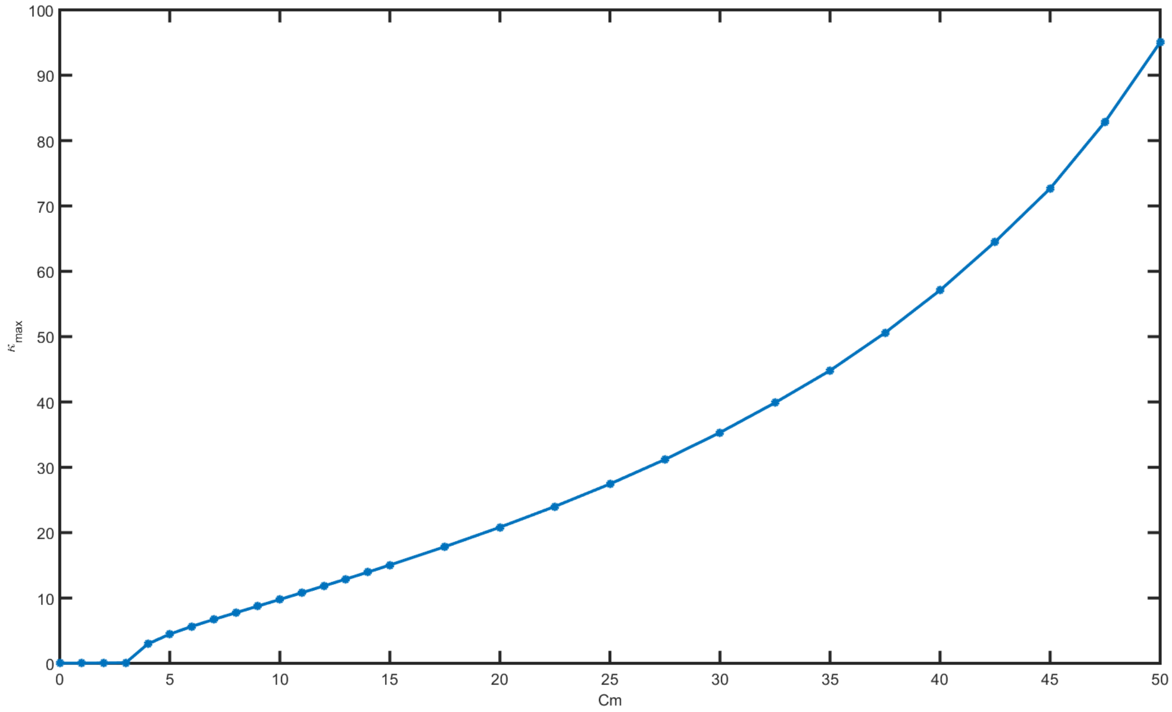

Fig. 4.44 Maximal curvature κ_{max} of the metastable superparamagnetic configurations in a constant field as a function of the magnetoelastic number Cm.

Partly inspired by the recent article of Vach and Faivre [73] we explore the dynamics of the filament in a magnetic field configuration that is somewhat different from those described in most of the pre-existing literature. The field is given by $\mathbf{H} = Cm(\sin(\beta\cos(\omega t)), \cos(\beta\cos(\omega t)), 0)$, with β as a new free parameter. The purpose of using such a field is to facilitate swimming in a particular direction, specified by the parameter β. All calculations in this section are conducted in the resistive force theory approximation with the classical value $\zeta_n/\zeta_t = 2$. Our parameter space is therefore expanded to $Cm - \omega - \beta$. Using the implicit backward Euler (IBE) scheme with a timestep of $2 \cdot 10^{-6}$ and a pre-formed hairpin (obtained from a linear configuration in the $x-y$ plane using a constant magnetic field as described previously in this section) as an initial condition, we explore the filament velocity over a representative number of identical periods of motion as a function of each of the three parameters while holding the other two constant. In the case of a constant $\beta = 0.5$ the filament exhibits a stable pattern of motion, but only within a narrow range of the parameters Cm and ω, as shown in figures 4.45 and 4.46, respectively.

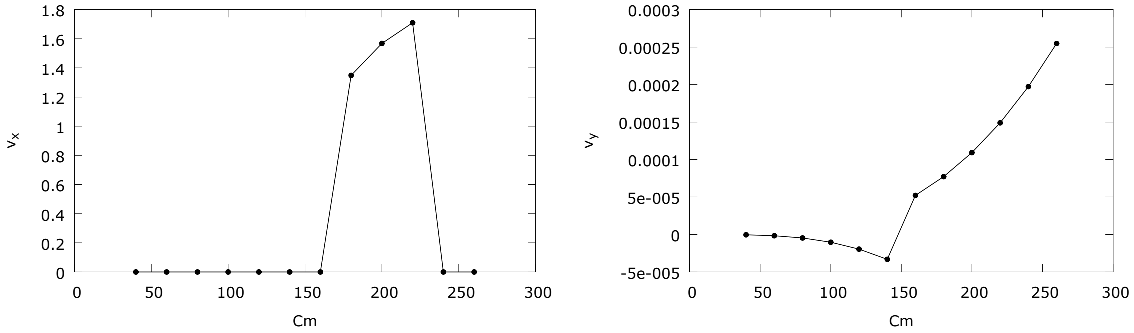

Fig. 4.45 Mean dimensionless filament velocity as a function of the magnetoelastic number Cm for $\beta = 0.5$, $\omega = 16000$.

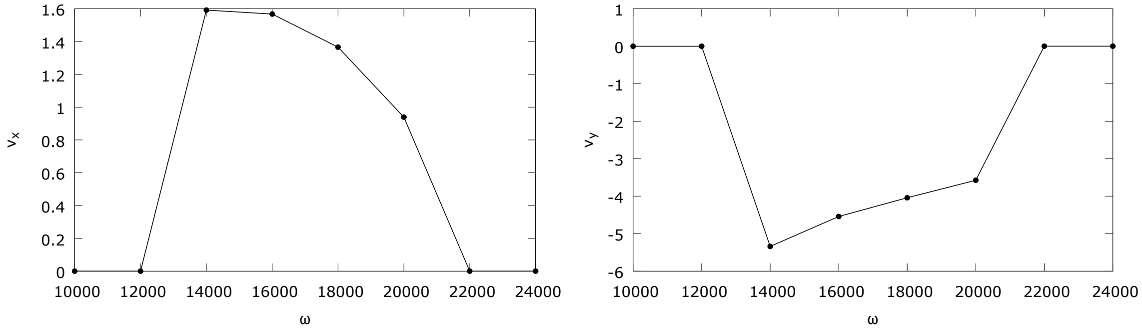

Fig. 4.46 Mean dimensionless filament velocity as a function of the dimensionless field frequency ω for $\beta = 0.5$, $Cm = 200$.

The dependence of the dimensionless filament velocity on the newly introduced parameter β is somewhat more intriguing. As shown in Fig. 4.47, there appears to be a quadratic dependence of the velocity on increasing values of the parameter β until a particular critical value at approximately $\beta_{critical} \approx 1.2$, after which the motion ceases abruptly. To the best of our knowledge, this finding has not been described before and may warrant further investigation should the configuration prove interesting for potential applications.

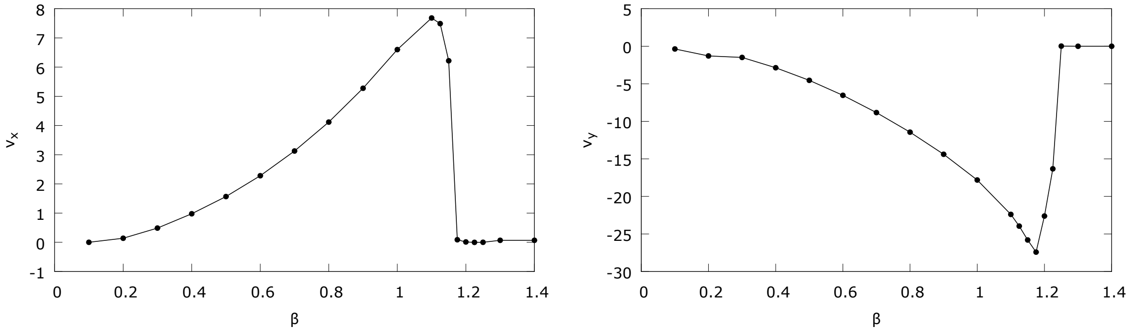

Fig. 4.47 Mean dimensionless filament velocity as a function of the parameter β for $\omega = 16000$, $Cm = 200$.

4.4 Magnetic dipole with an elastic tail

In the last few years a great deal of attention has been garnered by efforts to develop efficient externally actuated targeted delivery mechanisms for biomedical applications. In particular, in light of two recent articles by Pak, Gao *et al* [63] [34] which detailed the properties of a system consisting of a permanent magnet attached to a non-magnetic flexible tail we have been motivated to consider a new filament configuration where a flexible non-magnetic tail is attached to a magnetic dipole.

Due to the comprehensive nature of the numerical model and its theoretical underpinnings described in Chapters 2 and 3, only minimal modifications to our model are required to accommodate this new configuration. In particular, the only magnetic force we apply to the filament now comes in the form of a single boundary condition on the dipole itself, which in dimensionless form reads

$$\left.\frac{\partial^2 \mathbf{r}}{\partial s^2}\right|_{s=L} = Cm\left(\mathbf{h} - (\mathbf{h}\cdot\mathbf{t})\mathbf{t}\right), \tag{4.9}$$

where the magnetoelastic number is now defined as $Cm = mHL/A$ with the dipole moment m. The overall dynamics are controlled by the magnetoelastic number Cm, the ratio of the total filament length L to the elastic penetration length $L_e = (A/\zeta_N \omega)^{1/4}$ and the ratio of the dipole length L_d and the total filament length L. In terms of the numerical implementation, the dipole is modeled by the last discretization segment of the whole filament, with the boundary condition given in equation (4.9) replaced by the standard finite difference approximations used throughout this work. Both ends of the segment representing the dipole experience a force that is equal in magnitude and opposite in sign to satisfy the force and moment balance requirements discussed in Chapter 2. As for the dipole length, except where specifically noted otherwise, we use the ratio $L_d/L = 0.1$. The fact that the last segment of the filament now has different length also naturally modifies the resistive force theory (RFT) mobility tensor, given in Chapter 3 as

$$\boldsymbol{\mu}_{RFT}^{-1} = \left(\mathbf{I} + \frac{\zeta_t - \zeta_n}{\zeta_n}\right) D^{(1)}\mathbf{r} \otimes D^{(1)}\mathbf{r}, \tag{4.10}$$

since the finite difference operators $D^{(1)}$ naturally include the segment length (see Appendix C for the operator definitions). No such modifications are made to the Rotne-Prager-Yamakawa (RPY) mobility tensor.

Given an initially straight configuration oriented in the z direction it is found that the device exhibits propulsive behavior in both linearly oscillating (in either the x or y directions) and rotating (in the $x-y$ plane) external magnetic fields, swimming perpendicularly to the direction of the applied field. The propulsion is due to a bending deformation wave that propagates from the dipole down the elastic tail and induces a propulsive reaction force in the opposite direction, thus the swimmer propels itself head-first. This may be seen in configuration snapshots taken during a single period of the magnetic field shown in Figures 4.48 and 4.49. We also show a representative example of the center of mass displacement as a function of time in Figure 4.50. It is apparent that the characteristic back and forth pattern of motion that was also observed in ferromagnetic microswimmers (see section 4.1) is only seen during propulsion in a linearly oscillating field, whereas swimming in a rotating magnetic field displays a steady, continuous pattern of motion. It also seems that, all other parameters being equal, swimming in a rotating magnetic field is slightly more efficient.

We have published the results so far outlined in this subsection in an article in the journal *Physical Review E* [55] along with a detailed theoretical analysis of the swimmer dynamics. However, since the publication predates the introduction of more sophisticated approximations of hydrodynamic interactions in our model, it is interesting to further explore the impact of different hydrodynamic approximations on the dynamics of this microswimmer as well as the impact of the dipole length to total length ratio L_d/L.

First, let us review a representative sample of the center of mass displacements obtained using different hydrodynamic approximations. This is shown in Figure 4.51, with RFT_d denoting the resistive force theory mobility tensor calculated taking into account the extended length of the segment containing the dipole, whereas the usual RFT and RPY approximations neglect it. Similarly to our findings in previous filament configurations, it appears that the friction coefficient ratio $\zeta_n/\zeta_t = 1.75$ provides a closer match to the results obtained in the Rotne-Prager-Yamakawa approximation than the classical value $\zeta_n/\zeta_t = 2$. The impact of taking into account the extended length of the last segment of the filament is to slightly increase the velocity of the swimmer, however, the overall pattern of motion remains qualitatively unchanged. An appropriate adjustment to the Rotne-Prager-Yamakawa tensor will be considered in future research.

To broadly appreciate the impact of different frequencies for the external magnetic field (as expressed by the ratio $L/L_e = \omega^{1/4}$) we have calculated the dimensionless velocity of the center of mass of the microswimmer in both linear and rotating field configurations at two representative values of the magnetoelastic number. The results, calculated in the modified resistive force theory (RFT) approximation described previously, are shown in Fig. 4.52. The velocities display the usual quadratic dependence on the external field frequency described in previous sections and the published literature, however, it appears that the rotating field configuration produces considerably (by a factor of $1.5-2$ on average) higher swimming velocities, partly explained by the absence of the back and forth movement pattern observed in linearly oscillating fields (see Fig. 4.50 for a comparison). Furthermore, higher magnetoelastic numbers do not merely increase the resulting velocities observed in the motion of the microswimmer but also increase the numerical value of the optimal field frequency.

To complete our computational study of this microswimmer configuration we also analyze the impact of different values of the ratio of the dipole length to the total length of the microswimmer L_d/L in both linearly oscillating and rotating magnetic fields. Once again, the modified RFT approach is used to approximate the effect of hydrodynamic interactions. The results, displayed in Figures 4.53 and 4.54, show a consistent pattern: larger values of the ratio L_d/L are advantageous in comparatively slowly varying magnetic fields but produce the slowest microswimmers when large frequencies are chosen. This effect does not seem to directly depend on the value of the magnetoelastic number.

In summary, we have comprehensively described the general properties of a novel microswimmer assembled by attaching an elastic tail to a magnetic dipole in different configurations of the external magnetic field. The impact of all of the relevant parameters has been quantitatively described and the analysis conducted provides clear guidance to designing efficient magnetic microswimmers.

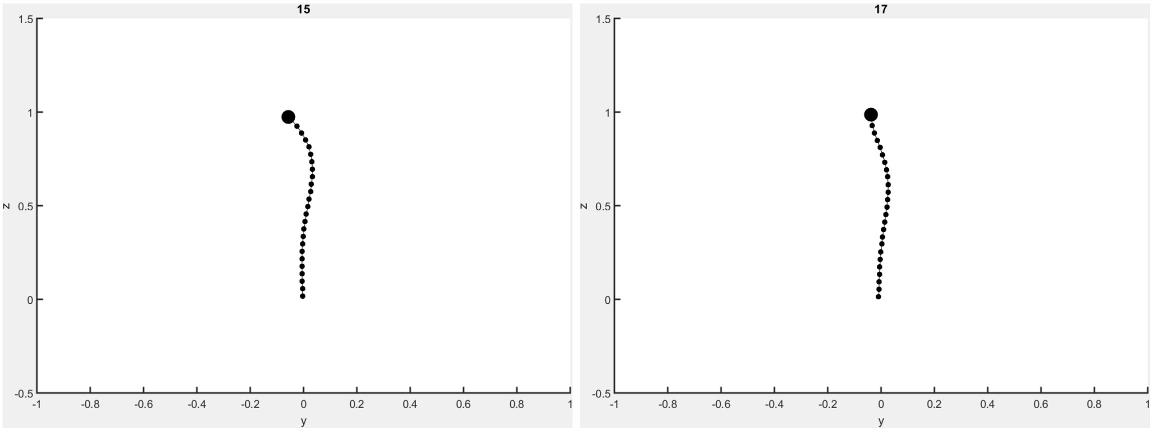

Fig. 4.48 Configuration of a dipole with an elastic tail in a linearly oscillating field at $t = 0.0015$ (left) and $t = 0.0017$ (right). $Cm = 10$, $L/L_e = 7.5$, $\zeta_n/\zeta_t = 1.75$.

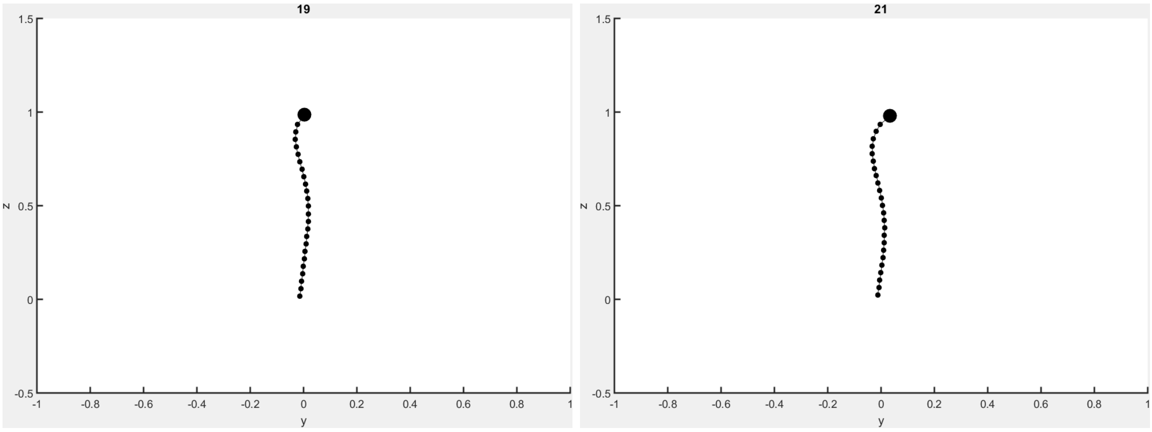

Fig. 4.49 Configuration of a dipole with an elastic tail in a linearly oscillating field at $t = 0.0019$ (left) and $t = 0.0021$ (right). $Cm = 10$, $L/L_e = 7.5$, $\zeta_n/\zeta_t = 1.75$.

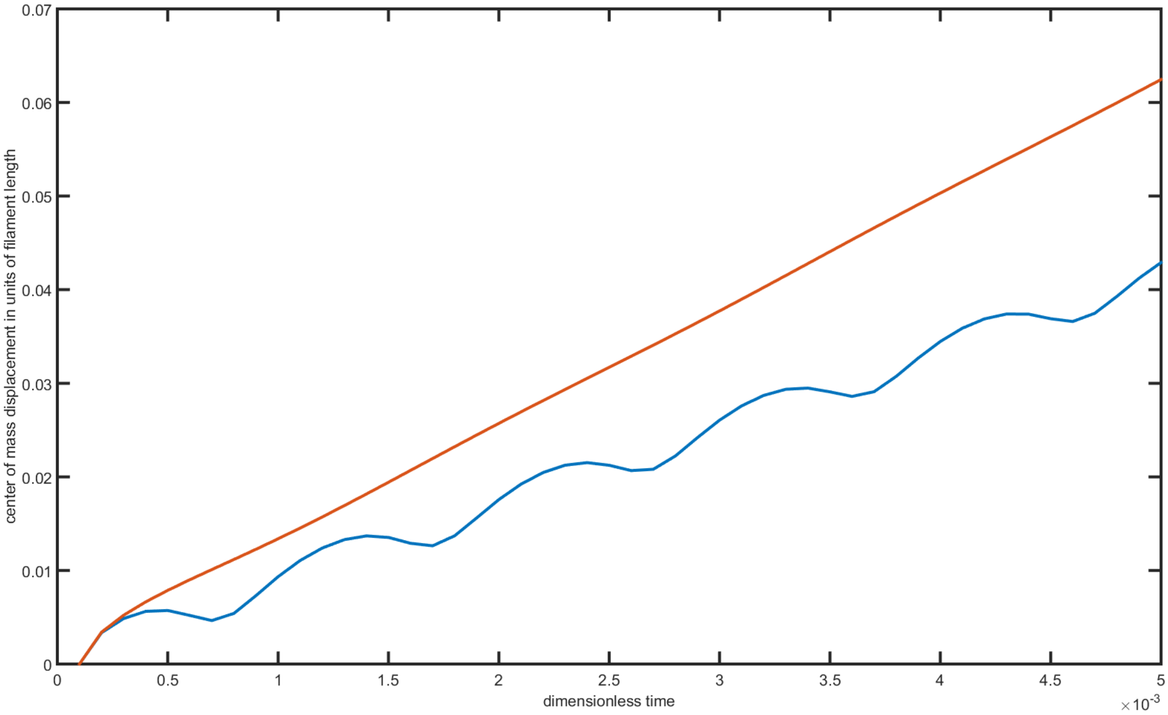

Fig. 4.50 Displacement of the swimmer's center of mass in a linearly oscillating (blue) and rotating (red) magnetic field. $Cm = 10$, $L/L_e = 7.5$, $\zeta_n/\zeta_t = 1.75$.

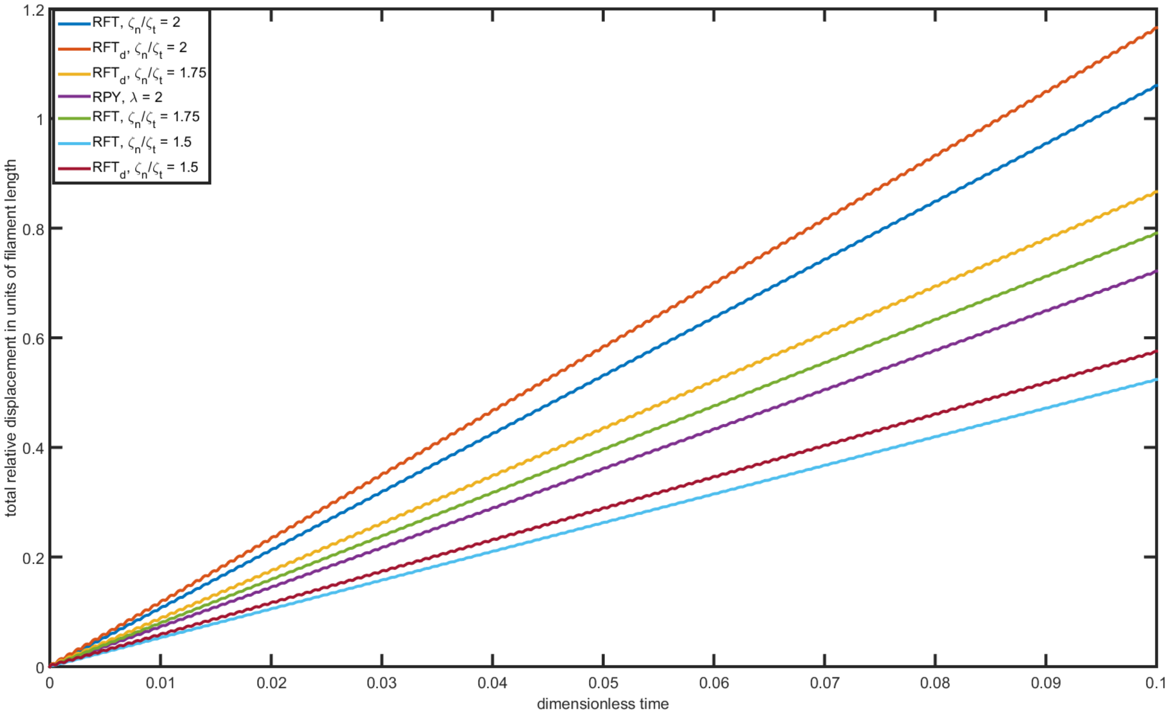

Fig. 4.51 Displacement of the swimmer's center of mass in a linearly oscillating magnetic field using different hydrodynamic approximations. $Cm = 10$, $L/L_e = 8$.

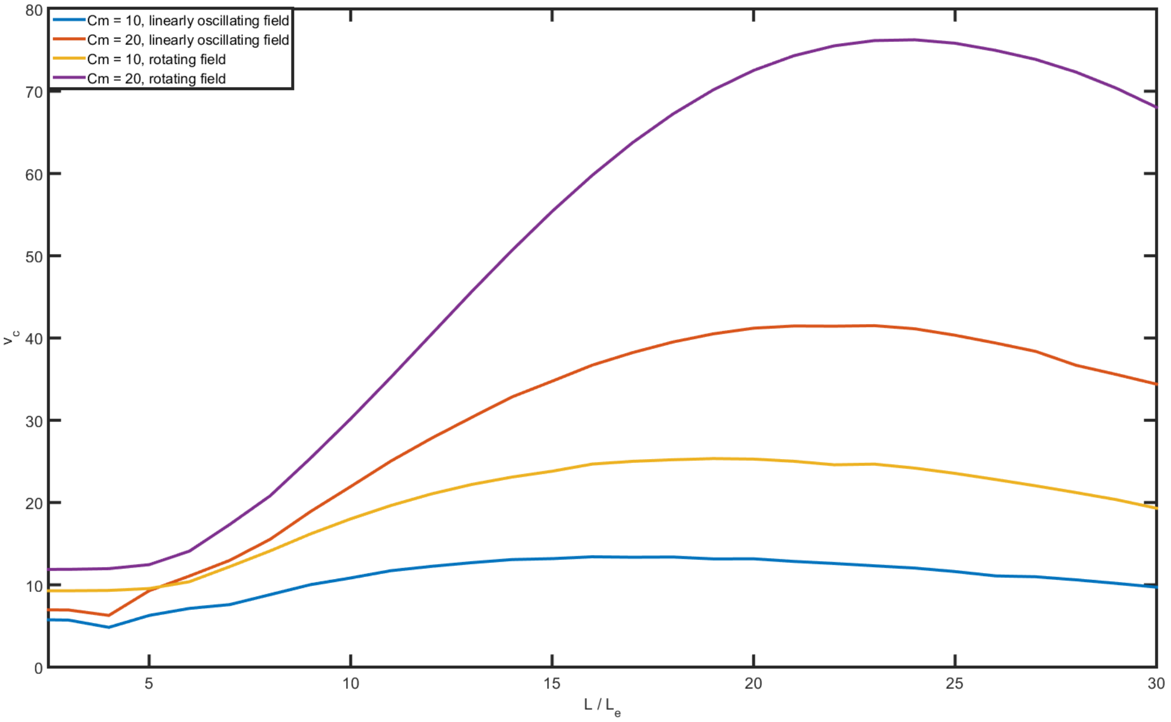

Fig. 4.52 Velocity of the swimmer's center of mass using the modified RFT approximation, $\zeta_n/\zeta_t = 1.75$.

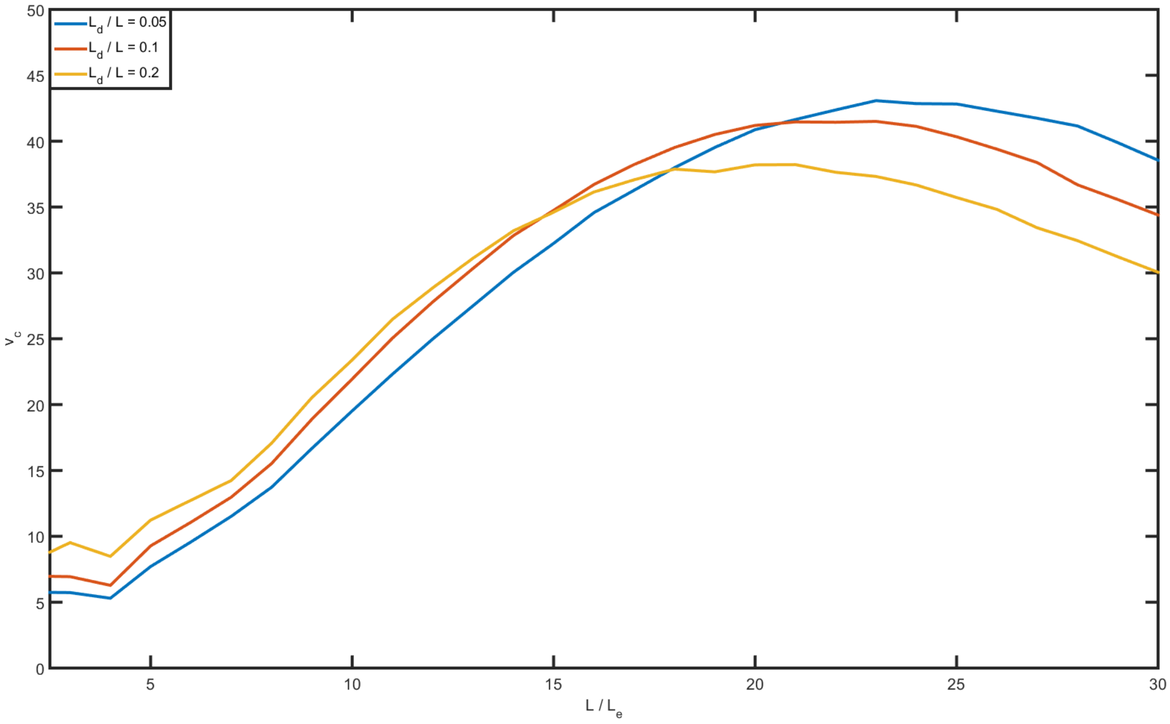

Fig. 4.53 Velocity of the swimmer's center of mass using the modified RFT approximation at different values of the ratio L_d/L in a linearly oscillating field. $\zeta_n/\zeta_t = 1.75$, $Cm = 20$.

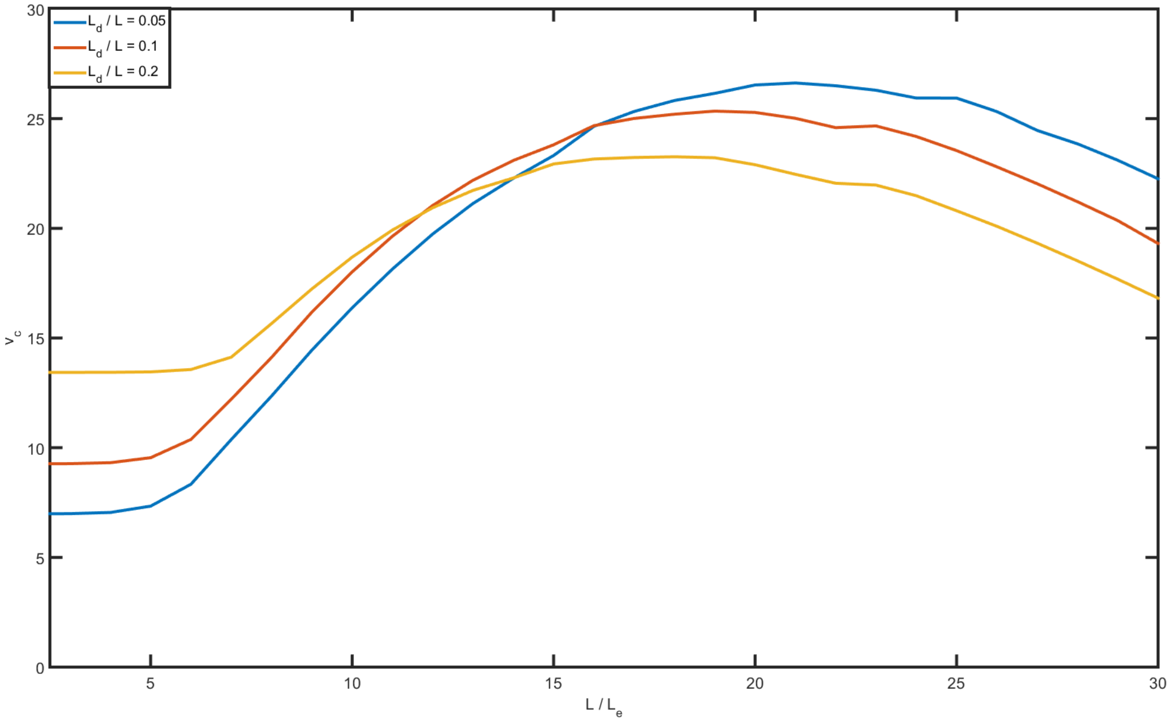

Fig. 4.54 Velocity of the swimmer's center of mass using the modified RFT approximation at different values of the ratio L_d/L in a rotating field. $\zeta_n/\zeta_t = 1.75$, $Cm = 10$.

4.5 Multiple interacting filaments

As we noted in Chapter 3, the way we have formulated our model permits straightforward generalization to an arbitrary number of filaments. While filament ensemble calculations are subject to fairly severe computational constraints, as described in Section 3.3, we do have a brief selection of results to elucidate the hydrodynamic coupling between filaments in small ensembles of two or three filaments.

Let us take the same initial conditions as in sections 4.1.1 and 4.1.2 (for the two dimensional and three dimensional case, respectively) and generalize them to an arbitrary number of ferromagnetic filaments with free ends arranged in a linear sequence in the y direction so that

$$x_i^{(N)} = \left(1-(0.01\pi/2)^2 ih\right), \tag{4.11}$$

$$y_i^{(N)} = 0.01\sin\left(\frac{\pi x_i}{1-(0.01\pi/2)^2}\right) + N\gamma, \tag{4.12}$$

$$z_i^{(N)} = \alpha x_i, \tag{4.13}$$

where N denotes the filament index (running from 1 to the number of filaments in the system) and γ is the distance between two consecutive filaments in the y direction. For the purposes of this section we shall take $\gamma = 1.5$ and $N \leq 3$, where the latter restriction is imposed for computational reasons. The parameter $\alpha = 0$ in the 2D case (see section 4.1.1 for the single filament treatment) and $\alpha = 10^{-4}$ (as in section 4.1.2). All calculations are done using the method of lines (MOL) scheme with $p = 100$ and hydrodynamic interactions are computed to the Rotne-Prager-Yamakawa (RPY) level with $\lambda = 0.5$. Let us first consider the two dimensional case, where we already established in section 4.1.1 that the basic dynamics of the filament consist of a metastable swimming regime which (in the RPY approximation) ultimately resolves into the S-like shape where the filament's center of mass is stationary. In Fig. 4.55 we have juxtaposed this result from section 4.1.1 with the relative y coordinate (with respect to the initial condition) of the center of mass of both filaments in a two filament ensemble, whereas the equivalent three dimensional situation is portrayed in Fig. 4.56. We can see that in both cases the swimming regime is still only metastable just as it was in the case of a single filament, with the relaxation time being approximately conserved. However, unlike the single filament case, the stable S-like shapes which are the ultimate result of both the single filament and the ensemble configurations are no longer stationary. In fact, in the two filament ensemble both filaments appear to be moving towards each other after the relaxation to the stable S-like configurations, solely as a result of hydrodynamic interactions, at least to the level of approximation provided by the Rotne-Prager-Yamakawa tensor. This may be further illustrated by visualizing the resulting flow field at $t = 0.0108$ using the same methodology as in section 4.2, as shown in Fig. 4.57. The two filaments, after relaxing to the stable S-like shapes, appear to have synchronized their periodic oscillations in such a way so as to mirror each other.

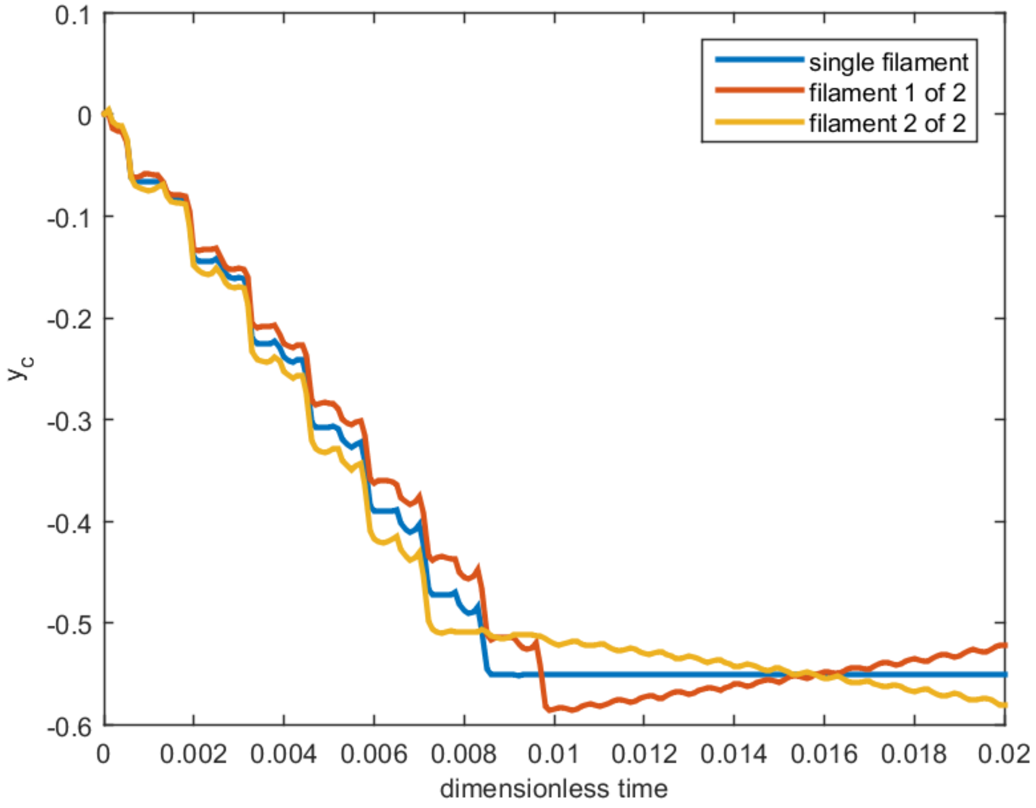

Fig. 4.55 Relative dimensionless center of mass y coordinate for a single filament and a two filament system with respect to dimensionless time in the 2D case. $Cm = 288$, $\omega = 4800$, $\alpha = 0$.

The results for the two filament system inspire a natural level of curiosity with respect to further generalization: what happens if we add more filaments to the ensemble? Given the similarity of both the 2D and 3D cases, it is sufficient to consider the 3D case with $\alpha = 10^{-4}$ and $N = 3$. The results are shown in Fig. 4.58. It appears that the general pattern of the two filament ensemble hold for the two outer filaments in this new configuration, whereas the middle filament is essentially stationary due to the mutually canceling effect of the two outer filaments.

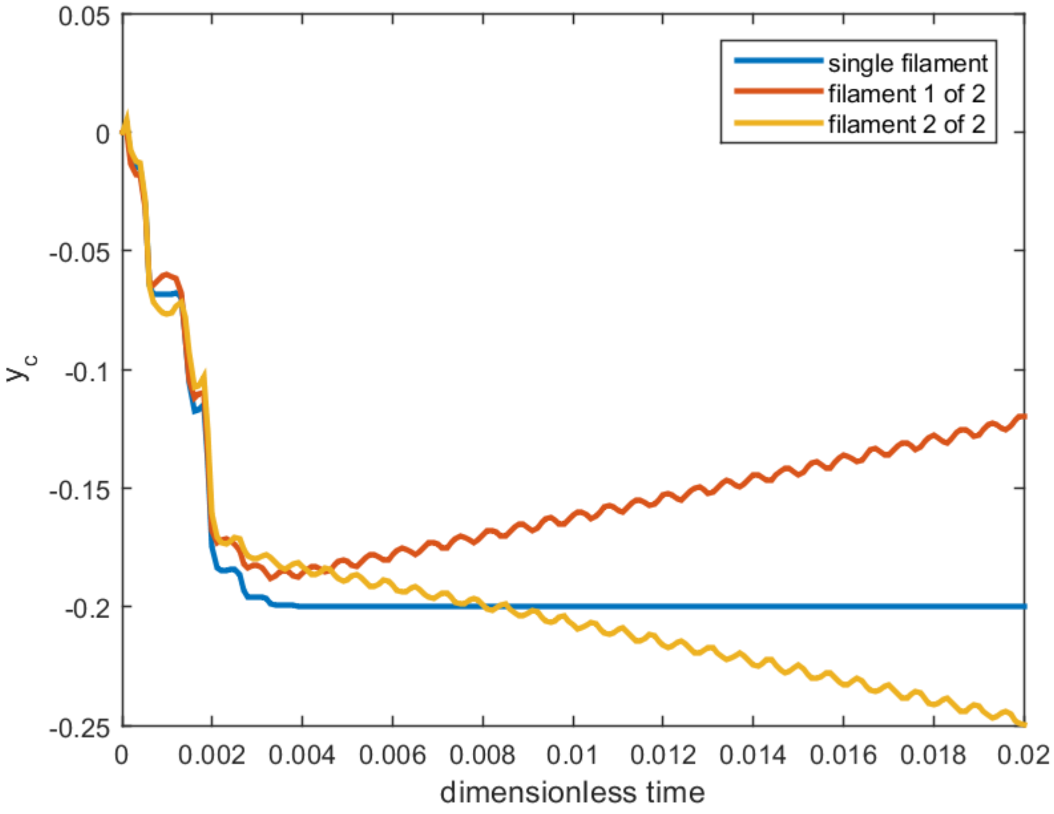

Fig. 4.56 Relative dimensionless center of mass y coordinate for a single filament and a two filament system with respect to dimensionless time in the 3D case. $Cm = 288$, $\omega = 4800$, $\alpha = 10^{-4}$.

The results we have obtained for the ensemble of ferromagnetic swimmers can be generalized to arbitrarily many swimmers as long as the linear array pattern is preserved, with any even number of filaments mirroring the results of the two filament system and any odd number of filaments echoing the results of the three filament ensemble. The methodology outlined here can be used to describe any arrangement of magnetic filaments as long as sufficient computational resources are available.

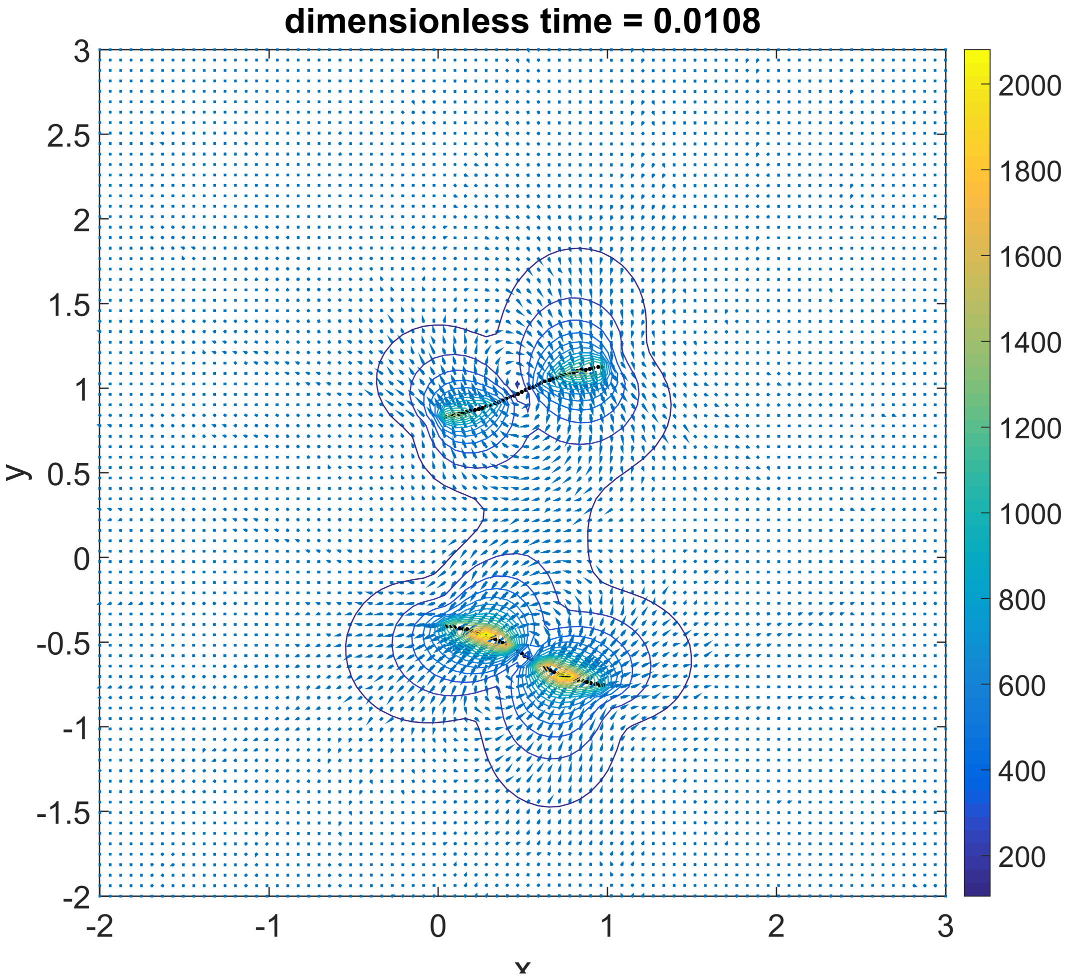

Fig. 4.57 Flow field induced by the two filament system at $t = 0.00108$. $Cm = 288$, $\omega = 4800$, $\alpha = 0$.

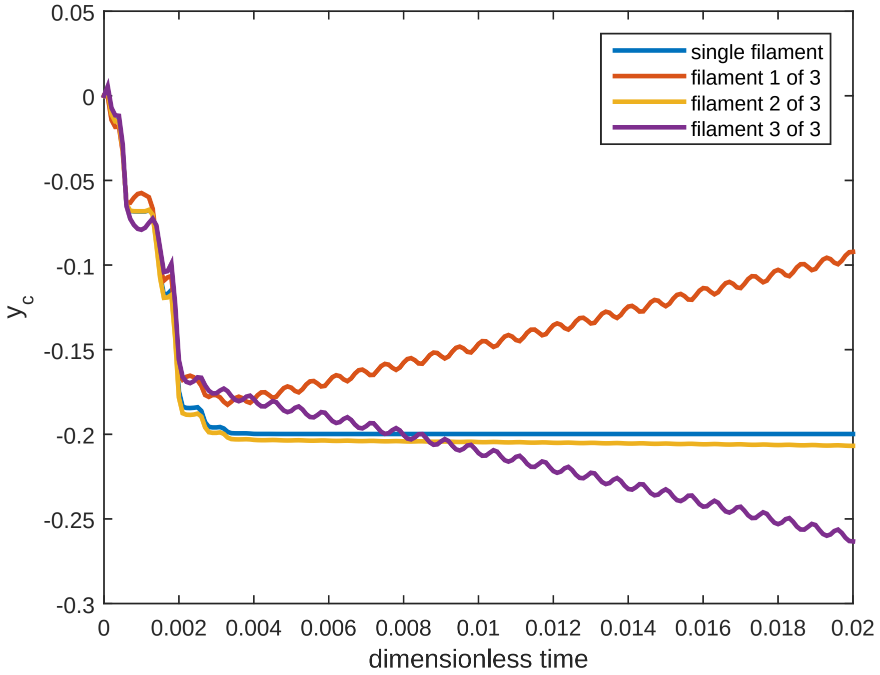

Fig. 4.58 Relative dimensionless center of mass y coordinate for a single filament and a three filament system with respect to dimensionless time in the 3D case. $Cm = 288$, $\omega = 4800$, $\alpha = 10^{-4}$.

Chapter 5

Results overview and future perspectives

In this chapter we briefly summarize the main results obtained in this dissertation and describe potential avenues for further research.

The primary purpose of this work was to construct a comprehensive and flexible computational model that would enable us to numerically obtain accurate descriptions of the dynamics of a wide range of filament configurations under the influence of different configurations of external magnetic fields. We have formulated the theoretical foundations of such a model in Chapter 2 using the known potential energy densities associated with the different phenomena a flexible magnetic filament is subject to when immersed in a Stokesian fluid and actuated by an external time dependent magnetic field. Utilizing a variational approach we then derived the appropriate force densities and formulated equations of motion. We also described three different methods of calculating the mobility tensor used to calculate the impact of hydrodynamic interactions on the filament dynamics.

We then discretized the equations of motion in Chapter 3, constructing two finite difference schemes to solve the discrete equivalents of the governing differential equations and described our dual implementation of the numerical model in two different programming languages - MATLAB and Julia. We also showed how the numerical model we had obtained could be generalized quite straightforwardly to the case of arbitrarily many hydrodynamically coupled filaments. The computational characteristics of the model were examined empirically, establishing both the numerical accuracy with respect to the primary numerical parameters and the computational requirements for calculating the filament dynamics at different levels of approximation. It is shown that certain hydrodynamic approximations - chiefly the method of induced forces, as implemented in the HYDROLIB library, but also some implementations of the Rotne-Prager-Yamakawa tensor are quite expensive computationally on modern computer hardware, even to the point of making certain calculations completely impractical. It is therefore of paramount importance to establish the importance of different levels of hydrodynamic approximations to the dynamics of magnetic filaments in different cases.

We therefore obtained empirical results for the benchmark case of a planar ferromagnetic microswimmer with free ends the dynamics of which we had described in previous work. The accuracy of the Rotne-Prager-Yamakawa approximation was established by comparisons with both the more accurate HYDROLIB library and previous results.

The dynamics of a fully three dimensional ferromagnetic microswimmer were described using the Rotne-Prager-Yamakawa approximation, obtaining a novel result: the swimming regime which was previously considered stable from results obtained in the resistive force theory approximation are in fact merely metastable when more accurate models of hydrodynamic interactions are considered, although the instability can in fact be minimized by an appropriate choice of the primary dimensionless parameters that govern the filament dynamics - the magnetoelastic number Cm and the dimensionless field frequency ω. We also utilize the computational efficiency of our model implementation to map out the parameter space $Cm-\omega$, thereby clearly delineating the precise regions of the parameter space where the level of hydrodynamic approximation matters the most.

We then proceeded to examine the effects of twist on the dynamics of ferromagnetic microswimmers and showed that, even for small values of the dimensionless twist diffusion d_0, the effects of twist are fairly negligible in comparison to the impact of hydrodynamic interactions as calculated to the Rotne-Prager-Yamakawa level. We also find that the dynamics of the ferromagnetic swimmer with the Rotne-Prager-Yamakawa approximation are even more unstable than previously established at the resistive force theory level.

Ferromagnetic cilia are investigated using various approximations to the hydrodynamic interactions. Substantial differences in the filament shape are found compared to previously published data. We also utilize the properties of the Stokes equations to calculate the fluid flow field induced by the rotating cilia and establish the dependence of the mean velocity of the flow in the vicinity of the filament on the governing parameters Cm and ω.

A modified rotating field configuration for superparamagnetic filaments with free ends is employed to characterize the swimming of superparamagnetic filaments at a particular angle, controlled by the external field. The velocities of the swimming filament are calculated in a wide range of the parameters Cm and ω in the resistive force theory approximation, showing that only narrow sets of the field parameters actually permit propulsive motion. It is also shown that the velocity depends approximately quadratically on the newly introduced field parameter β until a critical $\beta \approx 1.2$ is reached, at which point the filament abruptly ceases to swim.

We have investigated a novel system consisting of an elastic tail attached to a magnetic dipole. It is shown that this configuration exhibits propulsive behavior in both linearly oscillating and rotating magnetic fields, with overall higher velocities than the other swimmers considered in this work. The impact of different hydrodynamic approximations as well as the ratio of the dipole length to the overall length of this microswimmer are numerically investigated for different values of the magnetoelastic number Cm and the dimensionless field frequency ω.

Filament ensembles of two and three ferromagnetic swimmers are investigated, establishing the existence of a hydrodynamic coupling between the stable S-like shapes. The same coupling also exists in the three filament system when the outer two filaments are examined, while the middle filament is effectively shielded by the opposite flows induced by the outer filaments.

To summarize, we have constructed a comprehensive model capable of calculating the single and ensemble dynamics of ferromagnetic and superparamagnetic filaments in different external magnetic fields to different levels of approximation and used it to derive a number of novel results, elucidating several previously unknown features of these systems compared to the published literature.

Conclusions

1. A comprehensive numerical model capable of simulating both the single and ensemble dynamics of magnetic filaments has been formulated and implemented in the form of two software packages. It allows one to take into account the effects of bending and twist for both ferromagnetic and superparamagnetic filaments in arbitrary external magnetic fields, handling hydrodynamic interactions at three distinctly different levels of approximation and the flexibility of the model implementation allows for easy extension to different boundary conditions and filament configurations. The accuracy and computational requirements of the model have been extensively investigated.

2. The swimming behavior of ferromagnetic filaments with free ends, previously considered stable at least in the two dimensional case, has been shown to be only metastable when more accurate hydrodynamic approximations are used. The instability has been quantified with respect to the governing parameters of motion - the magnetoelastic number Cm and the dimensionless field frequency ω.

3. The dynamics of ferromagnetic cilia in rotating fields have been investigated taking into account hydrodynamic interactions for the first time. Substantial differences in the filament shape due to the hydrodynamic interactions have been found and the flow fields surrounding the rotating filaments quantified, supporting the potential applications of ferromagnetic artificial cilia in microfluidic mixing.

4. A new kind of microswimmer consisting of an elastic tail attached to a magnetic dipole has been extensively described numerically and shown to be more efficient in terms of swimming velocity than previously proposed types of microswimmers.

5. Small ensembles of ferromagnetic filaments have been investigated numerically, demonstrating the existence of a hydrodynamic coupling between the stable S-like states.

References

[1] Ames, W. F. (2014). *Numerical methods for partial differential equations*. Academic press.

[2] Badano, J. L., Mitsuma, N., Beales, P. L., and Katsanis, N. (2006). The ciliopathies: an emerging class of human genetic disorders. *Annu. Rev. Genomics Hum. Genet.*, 7:125–148.

[3] Batchelor, G. (1970). Slender-body theory for particles of arbitrary cross-section in stokes flow. *Journal of Fluid Mechanics*, 44(03):419–440.

[4] Bayin, S. (2006). Mathematical methods in science and engineering. *John Wiley&Sons, New York.*

[5] Belovs, M. and Cēbers, A. (2009). Ferromagnetic microswimmer. *Physical Review E*, 79(5):051503.

[6] Belovs, M. and Cēbers, A. (2013). Parametric excitation of bending deformations of a rod by periodic twist. *Physical Review E*, 87(2):023202.

[7] Belovs, M., Cīrulis, T., and Cēbers, A. (2009). Equilibrium shapes of twisted magnetic filaments. *Journal of Physics A: Mathematical and Theoretical*, 42(23):235206.

[8] Bezanson, J., Edelman, A., Karpinski, S., and Shah, V. B. (2014). Julia: A fresh approach to numerical computin. *arXiv preprint arXiv:1411.1607.*

[9] Bezanson, J., Karpinski, S., Shah, V. B., and Edelman, A. (2012). Julia: A fast dynamic language for technical computing. *arXiv preprint arXiv:1209.5145.*

[10] Bossis, G., Lacis, S., Meunier, A., and Volkova, O. (2002). Magnetorheological fluids. *Journal of Magnetism and Magnetic Materials*, 252:224–228.

[11] Cēbers, A. (2002). Dynamics of an elongated magnetic droplet in a rotating field. *Physical Review E*, 66(6):061402.

[12] Cebers, A. (2003). Dynamics of a chain of magnetic particles connected with elastic linkers. *Journal of Physics: Condensed Matter*, 15(15):S1335.

[13] Cēbers, A. (2005). Flexible magnetic filaments. *Current opinion in colloid & interface science*, 10(3):167–175.

[14] Cēbers, A. and Livanovičs, R. (2011). Flexible ferromagnetic filaments as artificial cilia. *International Journal of Modern Physics B*, 25(07):935–941.

[15] Chen, D.-X., Brug, J., Goldfarb, R. B., et al. (1991). Demagnetizing factors for cylinders. *Magnetics, IEEE Transactions on*, 27(4):3601–3619.

[16] Chen, S. and Doolen, G. D. (1998). Lattice boltzmann method for fluid flows. *Annual review of fluid mechanics*, 30(1):329–364.

[17] Cheney, E. W. and Light, W. A. (2000). *A course in approximation theory*, volume 101. American Mathematical Soc.

[18] Cichocki, B., Felderhof, B., Hinsen, K., Wajnryb, E., Bl, J., et al. (1994). Friction and mobility of many spheres in stokes flow. *The Journal of chemical physics*, 100(5):3780–3790.

[19] Cortez, R. (2001). The method of regularized stokeslets. *SIAM Journal on Scientific Computing*, 23(4):1204–1225.

[20] Courant, R. and Hilbert, D. (1966). *Methods of mathematical physics*, volume 1. CUP Archive.

[21] Dhont, J. K. (1996). *An introduction to dynamics of colloids*. Elsevier.

[22] Do Carmo, M. P. (1976). *Differential geometry of curves and surfaces*, volume 2. Prentice-Hall Englewood Cliffs.

[23] Drescher, K., Leptos, K. C., Tuval, I., Ishikawa, T., Pedley, T. J., and Goldstein, R. E. (2009). Dancing volvox: hydrodynamic bound states of swimming algae. *Physical Review Letters*, 102(16):168101.

[24] Dreyfus, R., Baudry, J., Roper, M. L., Fermigier, M., Stone, H. A., and Bibette, J. (2005). Microscopic artificial swimmers. *Nature*, 437(7060):862–865.

[25] Ērglis, K., Belovs, M., and Cēbers, A. (2009). Flexible ferromagnetic filaments and the interface with biology. *Journal of Magnetism and Magnetic Materials*, 321(7):650–654.

[26] Erglis, K., Livanovics, R., and Cebers, A. (2010). Three dimensional instability of the flexible ferromagnetic filament loop. *Magnetohydrodynamics*, 46(3):245–256.

[27] Ērglis, K., Livanovičs, R., and Cēbers, A. (2011). Three dimensional dynamics of ferromagnetic swimmer. *Journal of Magnetism and Magnetic Materials*, 323(10):1278–1282.

[28] Ērglis, K., Wen, Q., Ose, V., Zeltins, A., Sharipo, A., Janmey, P. A., and Cēbers, A. (2007). Dynamics of magnetotactic bacteria in a rotating magnetic field. *Biophysical journal*, 93(4):1402–1412.

[29] Ērglis, K., Zhulenkovs, D., Sharipo, A., and Cēbers, A. (2008). Elastic properties of dna linked flexible magnetic filaments. *Journal of Physics: Condensed Matter*, 20(20):204107.

[30] Evans, L. (1998). Partial differential equations.

[31] Fano, U. and Racah, G. (1959). Irreducible tensorial sets.

[32] Filippov, A. (2000). Drag and torque on clusters of n arbitrary spheres at low reynolds number. *Journal of colloid and interface science*, 229(1):184–195.

[33] Fornberg, B. (1988). Generation of finite difference formulas on arbitrarily spaced grids. *Mathematics of computation*, 51(184):699–706.

[34] Gao, W., Kagan, D., Pak, O. S., Clawson, C., Campuzano, S., Chuluun-Erdene, E., Shipton, E., Fullerton, E. E., Zhang, L., Lauga, E., et al. (2012). Cargo-towing fuel-free magnetic nanoswimmers for targeted drug delivery. *small*, 8(3):460–467.

[35] Gardiner, M. B. (2005). The importance of being cilia. *Howard Hughes Medical Institute Bulletin*, 18(64):33–36.

[36] Gauger, E. and Stark, H. (2006). Numerical study of a microscopic artificial swimmer. *Physical Review E*, 74(2):021907.

[37] Gelfand, I. M., , and Fomin, S. V. (2000). *Calculus of variations*.

[38] Gelfand, I. M. and Shilov, G. (1964). Generalized functions. vol. i: Properties and operations.

[39] Goubault, C., Jop, P., Fermigier, M., Baudry, J., Bertrand, E., and Bibette, J. (2003). Flexible magnetic filaments as micromechanical sensors. *Physical review letters*, 91(26):260802.

[40] Gray, J. and Hancock, G. (1955). The propulsion of sea-urchin spermatozoa. *Journal of Experimental Biology*, 32(4):802–814.

[41] Happel, J. and Brenner, H. (1983). *Low Reynolds number hydrodynamics: with special applications to particulate media*, volume 1. Springer Science & Business Media.

[42] Hill, E. (1954). The theory of vector spherical harmonics. *American Journal of Physics*, 22(4):211–214.

[43] Hindmarsh, A. C., Brown, P. N., Grant, K. E., Lee, S. L., Serban, R., Shumaker, D. E., and Woodward, C. S. (2005). Sundials: Suite of nonlinear and differential/algebraic equation solvers. *ACM Transactions on Mathematical Software (TOMS)*, 31(3):363–396.

[44] Hinsen, K. (1995). Hydrolib: a library for the evaluation of hydrodynamic interactions in colloidal suspensions. *Computer physics communications*, 88(2):327–340.

[45] Kamien, R. D. (2002). The geometry of soft materials: a primer. *Reviews of Modern physics*, 74(4):953.

[46] Keller, J. B. and Rubinow, S. I. (1976). Slender-body theory for slow viscous flow. *Journal of Fluid Mechanics*, 75(04):705–714.

[47] Kim, S. and Karila, S. (1991). *Microhydrodynamics: Principles and Selected Applications*. Butterworth-Heinemann.

[48] Lamb, H. (1993). *Hydrodynamics*. Cambridge university press.

[49] Landau, L. and Lifshitz, E. (1976). *Mechanics, vol. 1*.

[50] Landau, L. and Lifshitz, E. (1987). Fluid mechanics: volume 6 (course of theoretical physics).

[51] Landau, L. D., Bell, J., Kearsley, M., Pitaevskii, L., Lifshitz, E., and Sykes, J. (1984). *Electrodynamics of continuous media*, volume 8. Elsevier.

[52] Landau, L. D. and Lifshitz, E. (1986). Theory of elasticity, vol. 7. *Course of Theoretical Physics*, 3.

[53] Li, Z. and Lai, M.-C. (2001). The immersed interface method for the navier–stokes equations with singular forces. *Journal of Computational Physics*, 171(2):822–842.

[54] Lighthill, J. (1976). Flagellar hydrodynamics. *Siam Review*, 18(2):161–230.

[55] Livanovičs, R. and Cēbers, A. (2012). Magnetic dipole with a flexible tail as a self-propelling microdevice. *Physical Review E*, 85(4):041502.

[56] Luke, J. H. (1989). Convergence of a multiple reflection method for calculating stokes flow in a suspension. *SIAM Journal on Applied Mathematics*, 49(6):1635–1651.

[57] Madou, M. J. (2002). *Fundamentals of microfabrication: the science of miniaturization*. CRC press.

[58] Melle, S., Calderón, O. G., Rubio, M. A., and Fuller, G. G. (2002). Rotational dynamics in dipolar colloidal suspensions: video microscopy experiments and simulations results. *Journal of Non-Newtonian Fluid Mechanics*, 102(2):135–148.

[59] Mittal, R. and Iaccarino, G. (2005). Immersed boundary methods. *Annu. Rev. Fluid Mech.*, 37:239–261.

[60] Molina, J. J. and Yamamoto, R. (2013). Direct numerical simulations of rigid body dispersions. i. mobility/friction tensors of assemblies of spheres. *The Journal of chemical physics*, 139(23):234105.

[61] Nedelec, F. and Foethke, D. (2007). Collective langevin dynamics of flexible cytoskeletal fibers. *New Journal of Physics*, 9(11):427.

[62] Oprea, J. (2007). *Differential geometry and its applications*. MAA.

[63] Pak, O. S., Gao, W., Wang, J., and Lauga, E. (2011). High-speed propulsion of flexible nanowire motors: Theory and experiments. *Soft Matter*, 7(18):8169–8181.

[64] Peskin, C. S. (2002). The immersed boundary method. *Acta numerica*, 11:479–517.

[65] Powers, T. R. (2010). Dynamics of filaments and membranes in a viscous fluid. *Reviews of Modern Physics*, 82(2):1607.

[66] Purcell, E. M. (1977). Life at low reynolds number. *Am. J. Phys*, 45(1):3–11.

[67] Roper, M., Dreyfus, R., Baudry, J., Fermigier, M., Bibette, J., and Stone, H. A. (2006). On the dynamics of magnetically driven elastic filaments. *Journal of Fluid Mechanics*, 554:167–190.

[68] Rotne, J. and Prager, S. (1969). Variational treatment of hydrodynamic interaction in polymers. *The Journal of Chemical Physics*, 50(11):4831–4837.

[69] Shelley, M. J. and Ueda, T. (2000). The stokesian hydrodynamics of flexing, stretching filaments. *Physica D: Nonlinear Phenomena*, 146(1):221–245.

[70] Simons, J., Fauci, L., and Cortez, R. (2015). A fully three-dimensional model of the interaction of driven elastic filaments in a stokes flow with applications to sperm motility. *Journal of biomechanics*.

[71] Tian, F.-B., Luo, H., Zhu, L., Liao, J. C., and Lu, X.-Y. (2011). An efficient immersed boundary-lattice boltzmann method for the hydrodynamic interaction of elastic filaments. *Journal of computational physics*, 230(19):7266–7283.

[72] Tornberg, A.-K. and Shelley, M. J. (2004). Simulating the dynamics and interactions of flexible fibers in stokes flows. *Journal of Computational Physics*, 196(1):8–40.

[73] Vach, P. J. and Faivre, D. (2015). The triathlon of magnetic actuation: Rolling, propelling, swimming with a single magnetic material. *Scientific reports*, 5.

[74] Visser, A. (2001). Hydromechanical signals in the plankton. *Marine Ecology-Progress Series*, 222:1–24.

[75] Wajnryb, E., Mizerski, K. A., Zuk, P. J., and Szymczak, P. (2013). Generalization of the rotne–prager–yamakawa mobility and shear disturbance tensors. *Journal of Fluid Mechanics*, 731:R3.

[76] Wolgemuth, C. W., Powers, T. R., and Goldstein, R. E. (2000). Twirling and whirling: Viscous dynamics of rotating elastic filaments. *Physical Review Letters*, 84(7):1623.

[77] Xianyi, Z., Qian, W., and Chothia, Z. (2013). Openblas. *URL: http://xianyi. github. io/OpenBLAS*.

[78] Yamakawa, H. (1970). Transport properties of polymer chains in dilute solution: hydrodynamic interaction. *The Journal of Chemical Physics*, 53(1):436–443.

[79] Zapryanov, Z. and Tabakova, S. (1998). *Dynamics of bubbles, drops and rigid particles*, volume 50. Springer Science & Business Media.

Appendix A

Superparamagnetic energy term derivation

The purpose of this appendix is to compute the energy of the magnetic interaction between the superparamagnetic filament and the external magnetic field. For the purposes of this derivation, the filament is approximated by a semi-infinite paramagnetic cylinder. We also assume knowledge of the theory of classical electromagnetism, giving references where appropriate.

For a general magnetic object subjected to an external magnetic field the interaction energy reads

$$E = -\frac{1}{2}\int_V \mathbf{M}\cdot\mathbf{H}dV, \tag{A.1}$$

where **M** represents the magnetization, **H** is the external field and the integration is done over the volume of the object in question. When an external magnetic field is applied to a paramagnetic object, the orderly alignment of the magnetic dipoles in the material, which we assume to be instantaneous for the purposes of this derivation, gives rise to a non-zero magnetization, directed along the applied field. In component form, this may be given in the following form [51]

$$M_t = \chi H_t^{ext}, \tag{A.2}$$

$$M_n = \frac{\chi}{1+N_n\chi}H_n^{ext}, \tag{A.3}$$

where M_t and M_n denote the tangential (directed along the long axis of the cylinder) and normal (cross-sectional) components of the magnetization **M** respectively, H_t^{ext} and

H_n^{ext} are the appropriate components of the external magnetic field and χ is the magnetic susceptibility. Since the demagnetizing tensor, describing the impact of the object's geometry in inducing the demagnetizing field, is diagonal for ellipsoids [51], it may be reduced to three coefficients, which in our case are $N_1 = N_2 = N_n$ and $N_3 = N_t$. For semi-infinite cylinders the values are well known in the literature: $N_n = 2\pi$, $N_t = 0$ and expressions for arbitrary finite cylinders have also been obtained [15]. The analytic values for semi-infinite cylinders are sufficient for the case of long and thin filaments.

The internal magnetic field induced in the cylinder taking into account the demagnetizing field may be given in the following form

$$H_t^{int} = H_t^{ext}, \tag{A.4}$$

$$H_n^{int} = H_n^{ext} - \frac{N_n}{4\pi} M_n. \tag{A.5}$$

Using the expressions (A.2)-(A.5) we rewrite the scalar product $\mathbf{M} \cdot \mathbf{H}$ from equation (A.1)

$$\mathbf{M} \cdot \mathbf{H} = \chi H_t^2 - \frac{\chi H_n^2}{1 + 2\pi\chi}, \tag{A.6}$$

where we have dropped the superscript in H_t^{ext} and H_n^{ext} for brevity since only the external magnetic field will be referred to from now on. Utilizing the fact that $H_n^2 = H^2 - H_t^2$ we can separate out the terms dependent on the tangential component of the magnetic field, the remaining term is constant and therefore irrelevant to the integration

$$\mathbf{M} \cdot \mathbf{H} = \chi H_t^2 + \frac{\chi H_t^2}{1 + 2\pi\chi} + const. \tag{A.7}$$

We may now formally carry out the integration of the energy given in (A.1), using πa^2 as the cross-sectional area for a cylinder of radius a and keeping an integral factor for ensuring the orientation dependence

$$E = \frac{\pi^2 a^2 \chi^2}{1 + 2\pi\chi} \int (\mathbf{H} \cdot \mathbf{t})^2 ds. \tag{A.8}$$

Rewriting this result in terms of the relative magnetic permeability and separating out the orientation independent part of the magnetic field $\mathbf{H}$ we get

$$E = \frac{a^2 (\mu - 1)^2 H^2}{8(\mu + 1)} \int (\mathbf{h} \cdot \mathbf{t})^2 ds. \tag{A.9}$$

Appendix B

Variational derivation of filament force densities

This appendix details the derivation of the filament force densities from the energies given in Section 2.2. Since the bending and twist force densities were already derived in the aforementioned chapter, we only need to consider the magnetic and stretching force densities here. For brevity, we do not restate the variational arguments presented in Section 2.3 and proceed directly to the calculation of the relevant integrals.

The relevant energies from Section 2.3 are restated here for reference. First, the stretching energy

$$E_{stretching} = \frac{1}{2}\int_0^L \Lambda(s)\left(\frac{\partial \mathbf{r}}{\partial s}\right)^2 ds, \tag{B.1}$$

where $\Lambda(s)$ is the internal tension of the filament. The ferromagnetic energy is given by

$$E_{magnetic} = MH\int_0^L (\mathbf{h}\cdot\mathbf{t})ds = MH\int_0^L \left(\mathbf{h}\cdot\frac{\partial \mathbf{r}}{\partial s}\right) ds, \tag{B.2}$$

where $-M\mathbf{t}$ is the spontaneous magnetization (per unit length) of the filament and H is the strength of the external magnetic field. The superparamagnetic energy is given by

$$E_{magnetic} = M_0\int_0^L (\mathbf{h}\cdot\mathbf{t})^2 ds = M_0\int_0^L \left(\mathbf{h}\cdot\frac{\partial \mathbf{r}}{\partial s}\right)^2 ds. \tag{B.3}$$

where $M_0 = \frac{a^2(\mu-1)^2H^2}{8(\mu+1)}$ and μ denotes the magnetic permeability of the filament with a as its radius.

We now proceed to derive the stretching force density in a manner analogous to the bending energy derived in Section 2.2. The variation of the stretching energy is given by

$$\delta E_{stretching} = \int_0^L \Lambda \mathbf{t} \delta \mathbf{t} ds, \tag{B.4}$$

which can be integrated by parts to yield

$$\delta E_{stretching} = (\Lambda \mathbf{t} \delta \mathbf{r})|_0^L - \int_0^L \frac{\partial}{\partial s}(\Lambda \mathbf{t}) \delta \mathbf{r} ds. \tag{B.5}$$

The relevant force density is now obtained as the functional derivative utilizing the energy variation (B.5)

$$\mathbf{f}_{stretching} = -\frac{\delta E_{stretching}}{\delta s} = \frac{\partial}{\partial s}\left(\Lambda \frac{\partial \mathbf{r}}{\partial s}\right) \tag{B.6}$$

and the boundary terms in (B.5) can be immediately utilized to derive the boundary conditions in section 2.5.

For the ferromagnetic term the variation of the energy (B.2) reads

$$\delta E_{magnetic} = MH \int_0^L \mathbf{h} \cdot \delta \mathbf{t} ds. \tag{B.7}$$

Since the magnetic field unit vector $\mathbf{h}$ is not a function of the arclength, (B.7) can be integrated immediately to yield

$$\delta E_{magnetic} = (MH\mathbf{h} \cdot \delta \mathbf{r})|_0^L. \tag{B.8}$$

Obviously, the appropriate functional derivative gives $\mathbf{f} = \mathbf{0}$ in this case, implying that in the case of a ferromagnetic filament the external magnetic field acts solely upon the ends of the filament.

For the superparamagnetic case the variation of the energy (B.3) reads

$$\delta E_{magnetic} = 2M_0 \int_0^L (\mathbf{h} \cdot \mathbf{t})(\mathbf{h} \cdot \mathbf{t}) ds, \tag{B.9}$$

which may be integrated by parts (again utilizing the fact that $\mathbf{h}$ is not a function of the arclength parameter s) to yield

$$\delta E_{magnetic} = 2M_0 \left((\mathbf{ht})\mathbf{h}\delta \mathbf{r}\right)|_0^L - 2M_0 \int_0^L \left(\mathbf{h}\frac{\partial^2 \mathbf{r}}{\partial s^2}\right) \mathbf{h} \delta \mathbf{r} ds. \tag{B.10}$$

The appropriate functional derivative now gives us the magnetic force density for the superparamagnetic case

$$\mathbf{f}_{magnetic} = -\frac{\delta E_{magnetic}}{\delta s} = 2M_0 \left(\mathbf{h} \frac{\partial^2 \mathbf{r}}{\partial s^2} \right) \mathbf{h}. \tag{B.11}$$

This concludes the derivation of the required force densities for chapter 2.3 and the boundary terms that are used in chapter 2.5.

Appendix C

Derivation of the differentiation operators for the numerical model

The purpose of this appendix is to derive the finite differentiation operators $D^{(1)}$, $D^{(2)}$ and $D^{(4)}$ as well as their modified versions that take into account any relevant boundary conditions. The basic approach to deriving finite difference approximations to the derivatives of smooth functions is well known [1] and so only the main results will be briefly restated here as a starting point for our derivation.

If we take an arbitrary function of a scalar parameter $f(x_i)$, where the parameter x has been discretized in a uniform one dimensional grid with the constant spatial step h using $p+1$ marker points indexed by $i = 1, 2, \cdots, p+1$, the Taylor series expansion for $f(x_{i+1}) = f(x_i + h)$ reads

$$f(x_i + h) = f(x_i) + h \left.\frac{\partial f}{\partial x}\right|_{x_i} + \frac{h^2}{2!} \left.\frac{\partial^2 f}{\partial x^2}\right|_{x_i} + \ldots, \tag{C.1}$$

which may be easily rearranged to express a discrete approximation to the derivative

$$\frac{f(x_i + h) - f(x_i)}{h} = \left.\frac{\partial f}{\partial x}\right|_{x_i} + O(h), \tag{C.2}$$

where we have truncated the series at the first order term with respect to the parameter h, which corresponds to the order of the error introduced by the discrete approximation using a finite h. The left hand side of (C.2) is known as the first order accurate forward difference approximation to the first derivative of the function $f(x_i)$. An identical process of reasoning also yields the first order accurate backwards difference approximation

$$\left.\frac{\partial f}{\partial x}\right|_{x_i} = \frac{f(x_i) - f(x_i - h)}{h} + O(h), \tag{C.3}$$

whereas combining (C.3) and (C.2) gives the second order accurate central difference approximation, as the first order error term cancels out

$$\left.\frac{\partial f}{\partial x}\right|_{x_i} = \frac{f(x_i+h)-f(x_i-h)}{2h} + O(h^2), \tag{C.4}$$

so now the convergence of the approximation as the grid spacing h is decreased is quadratic rather than linear. This process may be continued recursively to obtain even order approximations to the first derivative up to arbitrary order, though it is usually not particularly useful to employ approximations of higher than fourth order due to the oscillations introduced by Runge's phenomenon [17] unless special grids are used.

Let us now generalize this approach to arbitrary order derivatives on arbitrary uniformly spaced grids for any level of accuracy we might wish. Suppose we pick a set of points (called a stencil) we would like to use in an approximate expression for the derivative $\left.\frac{\partial^n f}{\partial x^n}\right|_{x_i} = f^{(n)}$, with known function values $f(x_j) = f_j$, where $j = i-l,\dots,i+r$. Given the auxiliary index $m = -l,\dots,r$, the appropriate Taylor series reads

$$f_{i+m} = f_i + \frac{mh}{1!}f^{(1)} + \frac{m^2h^2}{2!}f^{(2)} + \frac{m^3h^3}{3!}f^{(3)} + \dots \tag{C.5}$$

Multiplying both sides of (C.5) by an arbitrary constant a_m and rearranging immediately yields a set of linear equations for the unknown coefficients a_m, with an equation for each possible value of the index m

$$\left(\sum_{m=-l,m\neq0}^{r} a_m f_{i+m}\right) - \left(\sum_{m=-l,m\neq0}^{r} a_m\right) f_i = \left(\sum_{m=-l,m\neq0}^{r} m a_m\right) \frac{h}{1!} f^{(1)} + \dots \tag{C.6}$$

The coefficient of the n-th derivative is therefore given by $c_n = \sum_{m=-l,m\neq0}^{r} m^n a_m$.

To illustrate this approach, let us take a simple example and use (C.6) to derive the fourth order accurate central difference approximation to the first derivative on the symmetric stencil given by $l = 2$, $r = 2$. We then have $c = (1,0,0,0)$ and the resulting system of equations reads

$$\begin{pmatrix} -2 & -1 & 1 & 2 \\ 4 & 1 & 1 & 4 \\ -8 & -1 & 1 & 8 \\ 16 & 1 & 1 & 16 \end{pmatrix} \begin{pmatrix} a_{-2} \\ a_{-1} \\ a_1 \\ a_2 \end{pmatrix} = \begin{pmatrix} 1 \\ 0 \\ 0 \\ 0 \end{pmatrix}, \tag{C.7}$$

yielding the coefficient vector $a = \frac{1}{12}(1, -8, 8, -1)$, which is well known in the literature. This method is illustrative but not particularly efficient. Fornberg [33] has derived recursive formulas for the derivation of arbitrarily precise approximations of any order derivative on grids that may be non-uniform, we have implemented this as part of our numerical model and therefore have the ability to programmatically generate the necessary coefficients for any desired finite difference approximation. This enables us to switch the approximation order at will.

For the sake of clarity, we list the basic differentiation operators used in Chapter 3 in matrix form with second order accuracy, beginning with the first order operator

$$D_h^{(1)} = \frac{1}{2h} \begin{pmatrix} -3 & 4 & -1 & 0 & 0 & \cdots & 0 \\ -1 & 0 & 1 & 0 & 0 & \cdots & 0 \\ 0 & -1 & 0 & 1 & 0 & \cdots & 0 \\ \vdots & \vdots & \vdots & \vdots & \vdots & \ddots & \vdots \\ 0 & \cdots & 0 & -1 & 0 & 1 & 0 \\ 0 & \cdots & 0 & 0 & -1 & 0 & 1 \\ 0 & \cdots & 0 & 0 & 1 & -4 & 3 \end{pmatrix}. \tag{C.8}$$

Evidently, in order to define such operators for a fixed order of accuracy it is sufficient to specify the diagonal coefficients $(-1/2, 0, 1/2)$ and the boundary coefficients $(-3/2, 2, 1/2)$, noting that the boundary coefficients on opposite ends are equal in magnitude, reversed in order and have opposite signs for odd order derivatives and equal signs for even order derivatives.

Similarly, the diagonal coefficients for the second derivative operator are given by $diag(D^{(2)}) = (1, -2, 1)$, whereas the boundary coefficients are $\delta D^{(2)} = (2, -5, 4, -1)$. The third order derivative operator is specified by $diag(D^{(3)}) = (-5/2, 9, -12, 7, -3/2)$ and $\delta D^{(3)} = (-1/2, 1, 0, -1, 1/2)$, whereas the fourth order derivative operator (using first order accuracy here for numerical reasons) can be written as $diag(D^{(4)}) = \delta D^{(4)} = (1, -4, 6, -4, 1)$.

We have now explicitly specified the finite differentiation operators for the first four derivatives of an arbitrary scalar function defined on a regularly spaced grid. However, as noted in Chapter 3, we also need to consider modified boundary coefficients for some of the operators to take into account the boundary conditions of the filament. In particular, we need to derive the modified operators $D_b^{(4)}$, $D_{tw}^{(1)}$, $D_{tw}^{(2)}$ and $D_m^{(1)}$ used in Section 3.1.

Let us begin with the modified operator $D_m^{(1)}$ used in the calculation of the magnetic force density for the ends of the filament in the case of a superparamagnetic material, since the derivation of the appropriate first derivative is relatively compact and will serve to illustrate the general principle, which we can generalize to the other operators as well.

First of all, we note that all of the modified differentiation operators differ only in the boundary coefficients, so we will only concern ourselves with the derivation of those here. In the case of a superparamagnetic filament with free ends, the boundary condition given in Section 2.5 implies that we need a differentiation operator for the first derivative that takes into account the fact that the second derivative must be equal to zero at the boundary. If we decide to satisfy the boundary condition to second order accuracy, we may take the second derivative approximation to second order accuracy and first order derivative to third order accuracy (so the number of points used in the approximation would match) and require that the following system of two linear algebraic equations be satisfied

$$2\mathbf{r}_1 - 5\mathbf{r}_2 + 4\mathbf{r}_3 - \mathbf{r}_4 + O(h^2) = \frac{\partial^2 \mathbf{r}_1}{\partial s} = \mathbf{0}, \tag{C.9}$$

$$-11\mathbf{r}_1 + 18\mathbf{r}_2 - 9\mathbf{r}_3 + 2\mathbf{r}_4 + O(h^3) = 6h\frac{\partial \mathbf{r}_1}{\partial s}. \tag{C.10}$$

If we multiply (C.9) by 2 and add the two equations together, we obtain

$$-7\mathbf{r}_1 + 8\mathbf{r}_2 - \mathbf{r}_3 + O(h^2) = 6h\frac{\partial \mathbf{r}_1}{\partial s}, \tag{C.11}$$

so the modified set of boundary coefficients is $D_m^{(1)} = (-7, 8, -1)/(6h)$. Since the constraint that $\delta D^{(2)} = 0$ is the same in all of our cases, the same approach we have utilized to derive $D_m^{(1)}$ leads immediately to the appropriate coefficients for the other differentiation operators as well. For instance, the modified fourth order differentiation operator for the bending term yields $\delta D_b^{(4)} = (1, -2, 1)/h^3$.